NASA Contractor Report 187143

Development of Graphite/Copper Composites Utilizing Engineered Interfaces

Sandra M. DeVincent
Case Western Reserve University
Cleveland, Ohio

June 1991

Prepared for
Lewis Research Center
Under Cooperative Agreement NCC3-94

National Aeronautics and
Space Administration

DEVELOPMENT OF GRAPHITE/COPPER COMPOSITES UTILIZING ENGINEERED INTERFACES

Abstract

by

SANDRA MARIE DeVINCENT

In situ measurements of graphite/copper alloy contact angles have been made using the sessile drop method. The interfacial energy values obtained from these measurements have then been applied to a model for the fiber/matrix inte facial debonding phenomenon found in graphite/copper composites.

The information obtained from the sessile drop tests has led to the development of a copper alloy that suitably wets graphite. Characterization of graphite/copper alloy interfaces subjected to elevated temperatures has been conducted using Scanning Electron Microscopy, Energy Dispersive Spectroscopy, Auger Electron Spectroscopy and X-Ray Diffraction analyses. These analyses have indicated that during sessile drop tests conducted at 1130°C for 1 hour, copper alloys containing greater than 0.98 at% chromium form continuous reaction layers of approximately 10 μm in thickness. The reaction layers are adherent to the graphite surface. The copper wets the reaction layer to form a contact angle of 60° or less. X-ray diffraction results indicate that the reaction layer is Cr_3C_2.

Acknowledgements

First and foremost, I would like to thank my advisor, Dr. Gary M. Michal. His sincere interest and enthusiasm have been always been appreciated. His patience and fairness have never gone unnoticed. I would like to thank the members of my thesis committee, Dr. John J. Lewandowski and Dr. Wendell S. Williams. My NASA technical advisor, Dr. Hugh Gray, deserves recognition for his interest and support.

To my NASA co-workers, Dr. David Ellis and Mr. David McDanels, I owe many thanks for their technical assistance and advice. I also would like to thank Dave Ellis for his contribution to the alloy selection, procurement and tests conducted in my absence. In addition, I would like to thank them both for many memorable conversations and travel experiences.

Also at the NASA Lewis Research Center, I would like to recognize Mr. Ricky Riveras and Mr. Henry Gerringer for the arc and induction melting of the alloy bars, and Ms. Frances Archer for conducting the chemical analyses. Mr. Gerald Loveland deserves many thanks for his assistance with the test set-up and for the design of the induction heating coils. His interest in this research, and many months of involvement with the testing, will not be forgotten.

I would like to express my appreciation to Dr. Wayne Jennings, in the Center for Surface Analysis of Materials, at CWRU, for his instruction and assistance with the Auger Electron Spectroscopy analyses.

Finally, this research has been supported by the Defense Advanced Research Projects Agency (DARPA) and the NASA Lewis Research Center in Cleveland, Ohio, through a NASA Graduate Student Researchers Program Fellowship under Grant no. 50-632.

Table of Contents

List of Figures

List of Tables

1 INTRODUCTION

1.1 Graphite/Copper Composites

1.1.1 Early Development

The increasing size and complexity of space-based hardware will lead to higher power consumption demands for future spacecraft and satellites. Although several types of advanced power systems are under consideration, they all have a heat source and a power conversion system. The power conversion systems require high temperature operation and an efficient, minimum-mass heat rejection radiator system.

Several designs for space power radiators exist. Figure 1.1 illustrates a generic continuous fin radiator concept and a generic separate fin concept. Excess heat from the power conversion system is sent to the radiator along a titanium heat pipe which is brazed directly to a radiator panel or fin. The panel both radiates heat directly and conducts the heat to a cooler area of the panel surface for radiation into space. Current designs call for beryllium, niobium or titanium alloys as radiator panel materials. However, each of these materials has drawbacks. Beryllium is lightweight and has a high modulus, but has safety, cost and handling problems. Niobium and titanium alloys have good high temperature properties, but are poor thermal conductors.

Ultra-high modulus pitch-based graphite fibers, with an elastic modulus of 690 GPa (100 Msi) or greater, have recently been developed. These fibers have thermal conductivities, along the axis of the fiber, equal to or better than that of copper. They also possess the density of beryllium and elastic moduli two to three times that of beryllium. Using these ultra-high modulus fibers to reinforce a copper matrix offers potential to produce lightweight, high modulus, high thermal conductivity composite materials for space radiator applications. A preliminary design analysis study [Rodini,

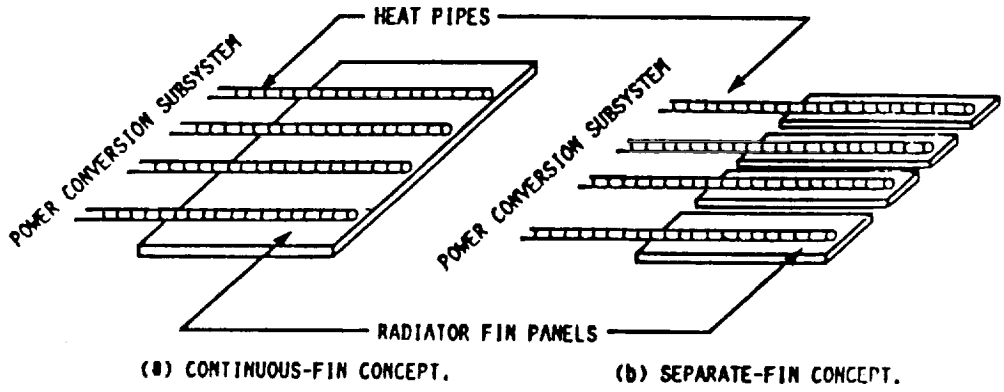

Figure 1.1. Generic space power system radiator concepts.
[McDanels and Diaz, 1989]

Thaw and Zweben, 1984] has estimated that a graphite/copper (Gr/Cu) composite radiator could offer the same performance as a beryllium panel with a mass savings of up to 9 percent for an SP-100 radiator.

1.1.2 Properties of Graphite/Copper Composites

An exploratory study was conducted to determine the feasibility of Gr/Cu composites for space power radiator applications [McDanels and Diaz, 1989]. This study evaluated a limited amount of vendor-supplied and NASA Lewis fabricated Gr/Cu composites. The focus of the investigation included the key factors involved in the design of space power radiator panels. Specific thermal conductivity and specific modulus of elasticity were investigated over a wide range of temperatures.

The Gr/Cu composites tested in this study were fabricated using unidirectionally oriented pitch-based P100 graphite fibers produced by Amoco Performance Products. The P100 fiber is supplied in tows, each containing approximately 2000 individual fibers of about 10 μm in diameter. The P100 tow had a nominal modulus of elasticity of 690 GPa, an ultimate tensile strength of 2070 MPa and a density of 2.15 kg/m^3. Gr/Cu experimental panels were purchased from DWA Composite Specialties. Panels were also fabricated at NASA Lewis Research Center by hot pressing copper coated P100 graphite fibers supplied by American Cyanimid Corporation.

The longitudinal thermal conductivities of the materials tested at temperatures up to 1100K (827°C) are shown in Figure 1.2. The unreinforced OFHC (oxygen free, high conductivity) copper and the NASA fabricated Gr/Cu composite were tested by the laser-flash method. The unreinforced copper lost about 10% of its room temperature thermal conductivity at 1100K. This reduction appears to be linear with temperature. Also indicated on this plot are handbook values for beryllium, which has approximately

one-third of the thermal conductivity of unreinforced OFHC copper over this temperature range.

The NASA fabricated 67 volume percent (v/o) composite panel exhibits similar thermal conductivity to unreinforced copper over the entire temperature range investigated. The composite lost about 20% of its room temperature thermal conductivity by 1100K. Most of this loss occurred at temperatures below 600K (327°C). Above 600K, the reduction paralleled that of the unreinforced copper.

Longitudinal thermal conductivity of the DWA 38 v/o Gr/Cu-Ti composite, measured by the steady-state comparative-rod technique, is less than half that of the NASA fabricated composite. Although the composites contain different volume fractions of fibers, the thermal conductivity properties can still be compared. Because the thermal conductivity of P100 graphite, along the fiber axis, is about the same as that of copper, the longitudinal thermal conductivity of the P100 Gr/Cu composites should be independent of fiber content. Deviations can therefore be attributed to matrix effects. The low thermal conductivity of the DWA supplied composite is most likely due to the titanium addition. Although this addition increased the strength of the matrix and improved the fiber/matrix interfacial bond, it substantially reduces the thermal conductivity of the copper matrix. The DWA composite showed a similar rate of reduction with temperature as both the NASA fabricated composite and the unreinforced copper.

While Gr/Cu composites exhibit excellent thermal conductivity in the longitudinal direction (parallel to the fibers), the thermal conductivity in the short-transverse direction (through-the-thickness) is considerably lower. In this orientation, the NASA fabricated composite has a thermal conductivity of only 60 W/mK at room temperature. This is about one-seventh that in the longitudinal direction.

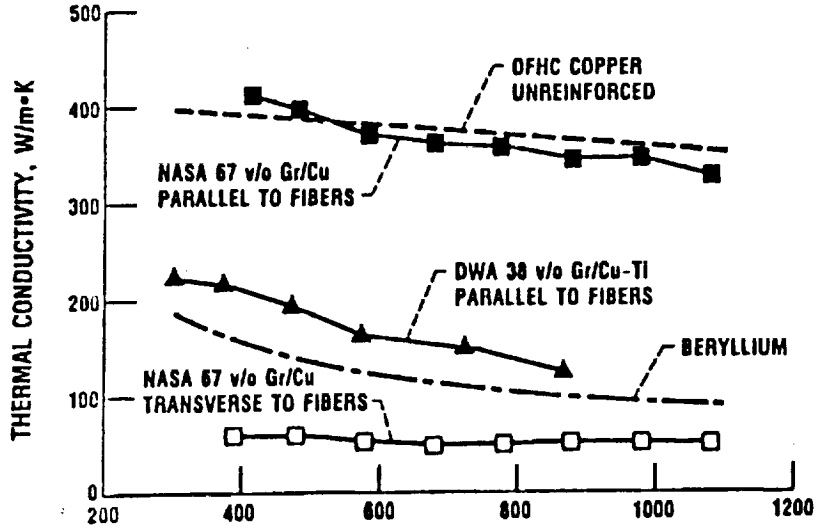

Figure 1.2. Comparison of thermal conductivity of Gr/Cu composites with competitive materials. [Titran, McDanels and Grobstein, 1989]

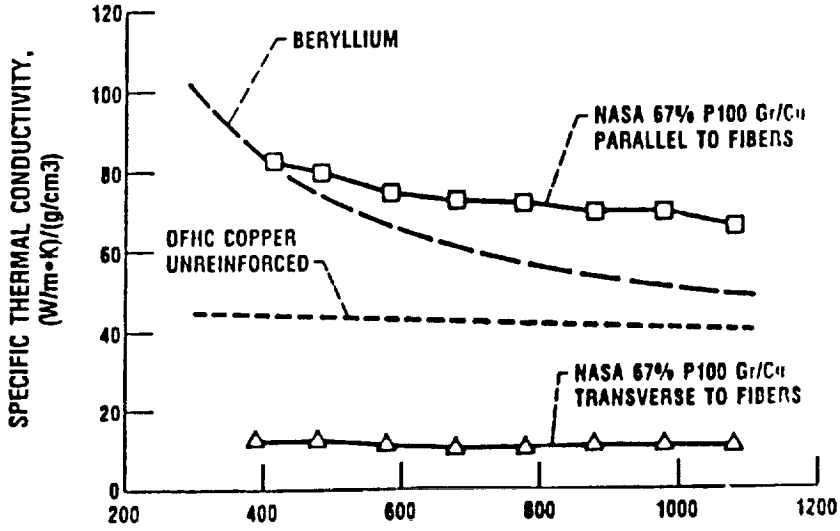

Figure 1.3. Comparison of specific thermal conductivity of Gr/Cu composites with competitive materials. [Titran, McDanels and Grobstein, 1989]

The density dependent, specific thermal conductivity is one of the most important design considerations for space power radiator systems. The longitudinal specific thermal conductivity of the Gr/Cu composites is plotted as a function of temperature in Figure 1.3. The values for copper and beryllium are included for comparison. The results for the composite, in the longitudinal direction, are significantly better than those for copper over the temperature range considered, and are better than those for beryllium at higher temperatures. These data indicate that Gr/Cu composites offer good potential for high specific thermal conductivity applications at elevated temperatures, as long as the heat can be conducted in the direction of the reinforcing fibers.

As indicated in Figures 1.2 and 1.3, the short transverse thermal conductivity of the Gr/Cu composites is much lower than the longitudinal. While this may appear discouraging, it must be noted that space power radiator systems operate at temperatures above the maximum service temperatures of copper and beryllium. The primary competition at elevated temperatures is titanium and niobium alloys. Figure 1.4 compares the short transverse specific thermal conductivity of the composite to Ti-6Al-4V and Nb-1Zr alloys. The plot shows that the NASA fabricated composite has better short-transverse specific thermal conductivity properties than the niobium alloys over the entire temperature range, and the titanium alloys at temperatures up to 700K (427°C). This temperature approaches the upper service temperature limit for titanium alloys. Because the titanium alloys do not have sufficient strength at these temperatures, Gr/Cu composites have better properties than both of these alloys at all usable temperatures.

Another important design criterion for space power radiator systems is modulus of elasticity. The specific modulus is even more critical because the vibrational frequency of a space power radiator is proportional to the square root of the

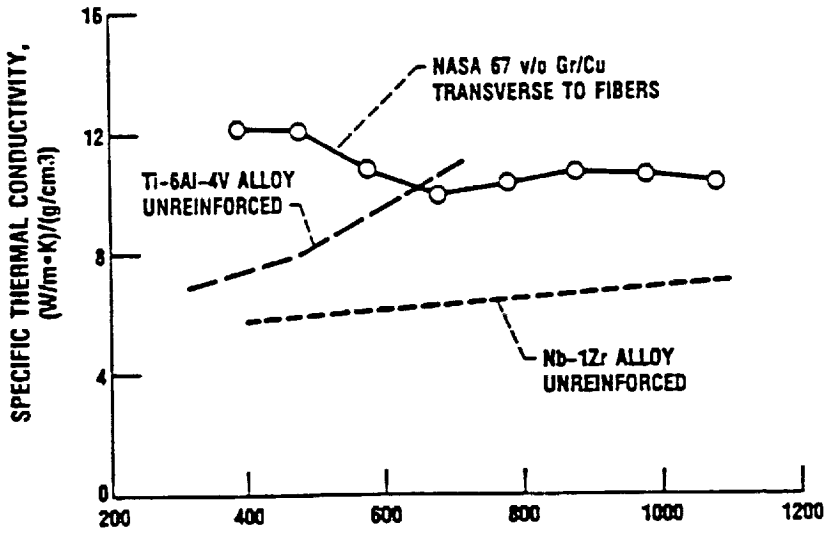

Figure 1.4. Comparison of transverse specific thermal conductivity of Gr/Cu composites with competitive materials. [Titran, McDanels and Grobstein, 1989]

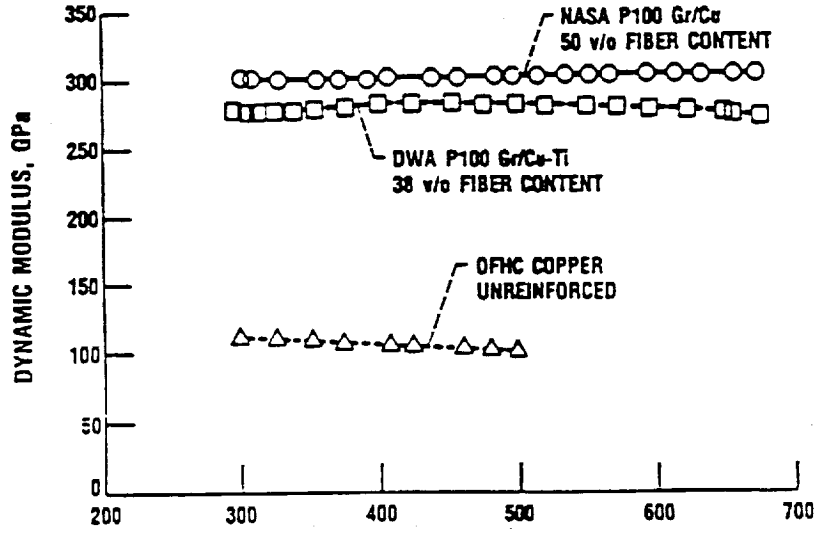

Figure 1.5. Comparison of the dynamic modulus of elasticity of Gr/Cu composites to unreinforced OFHC copper. [Titran, McDanels and Grobstein, 1989]

modulus/density ratio. Dynamic modulus of elasticity, in the longitudinal direction, of P100 Gr/Cu composites was measured over a range of temperatures. Sonic flexural resonance techniques were employed. The results for the NASA fabricated and DWA supplied composites are given in Figure 1.5, along with data for unreinforced copper. The two composites showed essentially no loss of modulus at temperatures up to 650K (377°C). The modulus of unreinforced copper, on the other hand, lost almost 10% of its room temperature modulus by 500K (227°C).

From a design viewpoint, the retention of modulus at elevated temperatures is desired because the structural stiffness of the composite can be maintained during operation. The high modulus/density ratio allows the design of a structure such that the fundamental frequency can be safely above the natural frequency of the space platform, thus eliminating problems associated with unexpected resonances.

1.2 Interfacial Energy

1.2.1 Theory

The fabrication and performance of composite materials designed for elevated temperature applications is strongly influenced by the fiber/matrix interface. A key aspect of metal/ceramic interfaces is the metal/ceramic interfacial energy. However, often the ideal matrix/fiber combinations, based upon their mechanical and physical properties, have high interfacial energies [Weitzer, Remschnig, Schuster and Rogl, 1990]. The high interfacial energies relative to the surface energies of the fibers result in a lack of wetting between the metal and fibers. This intrinsic lack of wetting causes difficulties in production of the composites, as shown in Figure 1.6. More importantly, the lack of wetting can lead to matrix fiber debonding and pore formation during the service life of the composites at elevated temperatures [McDanels and Diaz,

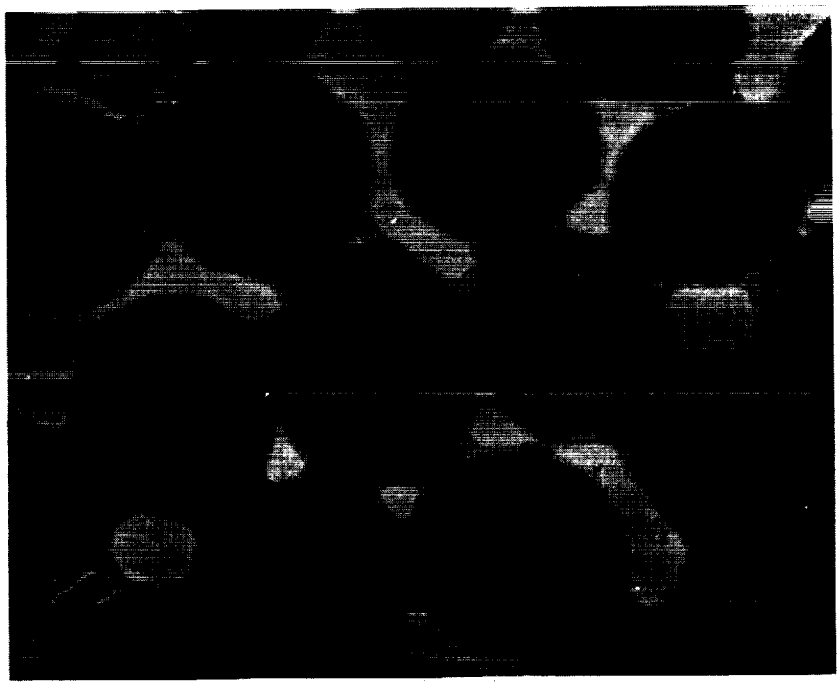

Figure 1.6. Copper 50 v/o P100 graphite fiber composite.

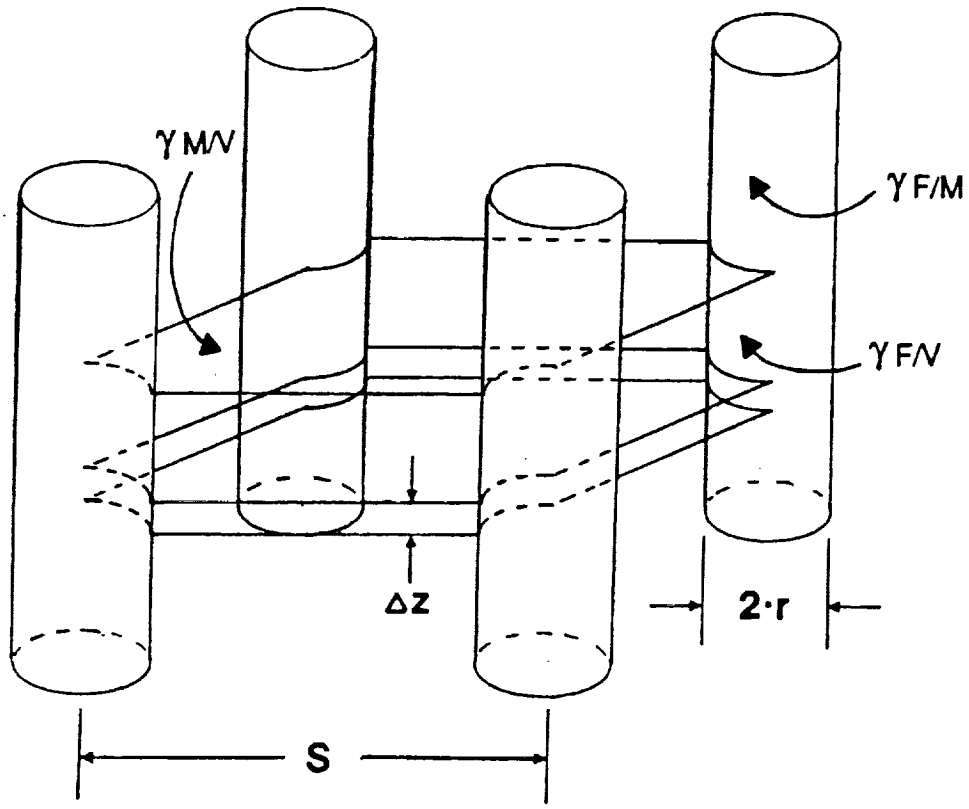

Figure 1.7. Model illustration. Cubic array of fibers of radius, r, and spacing, S.

1989; Ash and Fowser]. This lack of bonding is related to the Cu-C phase diagram and will be discussed later in Section 1.4.

1.2.2 Fiber/Matrix Debonding Model

The relationship between the creation and maintenance of a nonporous metal matrix composite and the fiber/metal interfacial energy is illustrated in Figure 1.7. The figure shows a matrix pore among a cubic array of fibers of radius, r, and spacing, S. The energy change, ΔE, associated with either expanding or shrinking the pore by ΔZ can be expressed as follows:

$$\Delta E = 4\,(S - 2r)\,\gamma_{M/V}\,\Delta z + (S^2 - \pi r^2)\,[\sigma_f\,|\Delta z| - \sigma_a\,\Delta z] + 2\pi r\,(\gamma_{F/V} - \gamma_{F/M})\Delta z \quad (1\text{-}1)$$

where σ_a is the applied stress, σ_f is the flow stress of the metal matrix, $\gamma_{M/V}$ is the metal/vapor interfacial energy, $\gamma_{F/V}$ is the fiber/vapor interfacial energy and $\gamma_{F/M}$ is the fiber/metal interfacial energy.

The first term in Equation (1-1) represents the energy associated with the creation or removal of free surface of the metal matrix. This term becomes vanishingly small as S approaches 2r, which would be the case for high volume fraction fiber composites. The second term represents the resistance to mass movement in the metal matrix. The third term in Equation (1-1) represents the wetting, or dewetting, potential for the fiber/metal interface. The sign of the energy change for this term varies depending upon whether the fiber/metal interfacial energy is less than, or greater than, the fiber surface energy. Determining the relative magnitudes of these two energies is thus the key to defining whether the pore will grow or shrink. During fabrication of a composite, an applied stress can be used to reduce the size of pores, overcoming the surface and interfacial energy effects. At elevated temperatures, however, the applied stress is no longer present and the surface and interfacial effects are dominant.

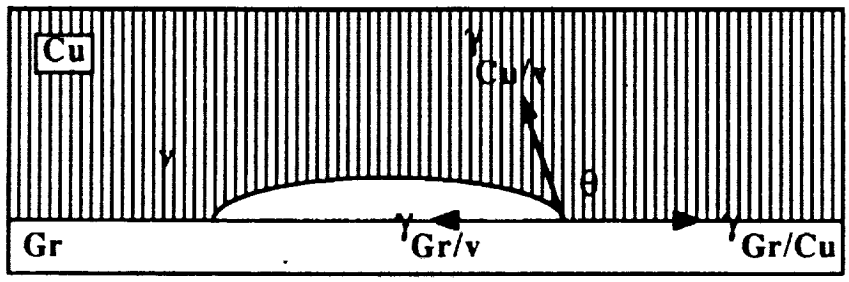

(a.) Void at fiber/matrix interface.

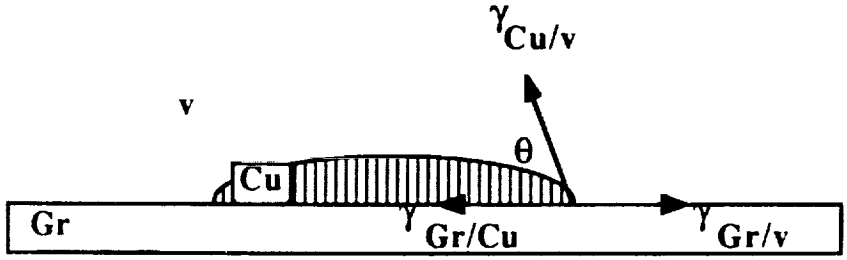

(b). Sessile drop configuration.

Figure 1.8. Comparison of a void present at a fiber/matrix interface and the sessile drop configuration.

A more simplified view of a void at a fiber/metal matrix interface is shown in Figure 1.8a. The balance of the surface and interfacial forces in that figure is seen to be quite analogous to the sessile drop geometry shown in Figure 1.8b. The balance of forces for both the void and sessile drop geometries leads to the Young-Dupre Equation [Bangham and Razouk, 1937]:

$$\gamma_{M/V} \cos\theta = \gamma_{F/V} - \gamma_{F/M} \tag{1-2}$$

The difference term on the right hand side of Equation (1-2) is exactly the measure of the driving force for void growth, or shrinkage, in a composite that is contained in Equation (1-1). The sign defines whether θ will be less than or greater than 90 degrees, independently of the magnitude of the metal surface energy. Restating this in terms of the liquid, the driving force for liquid flow between the fibers is proportional to $\gamma_{M/V}\cos\theta$, so that it is desirable to have a large solid surface energy, $\gamma_{F/V}$, and a small solid-liquid surface energy, $\gamma_{F/M}$ [Kingery, 1959].

Thus, a determination of θ being acute (wetting) or obtuse (nonwetting) defines whether void growth or shrinkage is possible. Modifying the surface and interfacial energies found on the right hand side of Equation (1-2) so that their difference is always positive, i.e. θ less than 90 degrees is a key to the successful long term performance of a fiber/metal composite system.

1.2.3 Factors Affecting Interfacial Energy

The interfacial energy between two materials can be affected by two different mechanisms. First, segregation, at the level of atomic monolayers, to the interface can lower the interfacial energy of a given system. Second, the interfacial energy can be altered by the creation of new phases at the interface that, in turn, produce new combinations of interfacial energies. An example is shown in Figure 1.9 of the

interface between materials A and B, and the interfaces between materials A and B with the addition of material C. With the creation of phase C, the interfacial energies are different from those of the original system.

1.3 Sessile Drop Test

1.3.1 Theory and Development

It is observed that in most instances a liquid placed on a solid will not wet it but remains as a drop having a definite angle of contact between the liquid and solid phases. The situation is illustrated in Figure 1.10. The following simple derivation leads to the Young-Dupre relationship [Adamson, 1990].

The change in surface free energy, ΔG^S, accompanying a small displacement of the liquid such that there is a change in area of solid covered, ΔA, is

$$\Delta G^S = \Delta A\,(\gamma_{SL} - \gamma_{SV}) + \Delta A\,\gamma_{LV}\cos(\theta - \Delta\theta) \qquad (1\text{-}3)$$

At equilibrium

$$\lim_{\Delta A \to 0} \frac{\Delta G^S}{\Delta A} = 0$$

and

$$\gamma_{SL} - \gamma_{SV} + \gamma_{LV}\cos\theta = 0 \qquad (1\text{-}4)$$

or

$$\gamma_{LV}\cos\theta = \gamma_{SV} - \gamma_{SL} \qquad (1\text{-}5)$$

The equation was stated in qualitative form in 1855 by Young [Young, 1805]. An equivalent equation was stated in algebraic form, in combination with the work of adhesion, by Dupre in 1869 [Dupre, 1869]. Together, the equations, which are really the same, are referred to as the Young-Dupre equation.

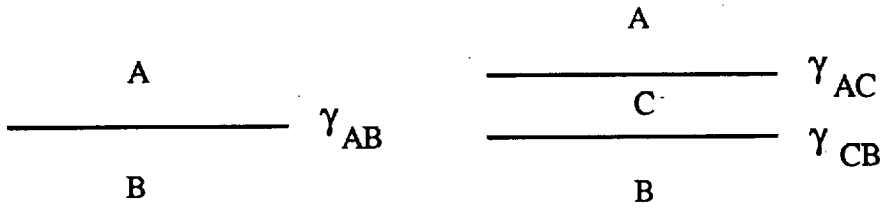

Figure 1.9. Interfaces of system A-B and system A-C-B.

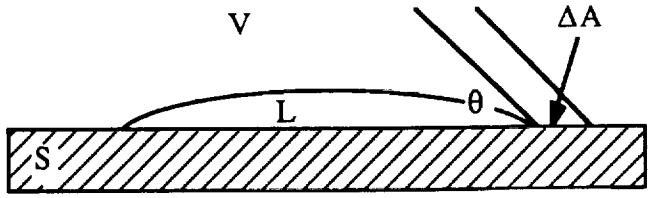

Figure 1.10. Solid-liquid-vapor interfaces with contact angle, θ and change in area of solid covered, ΔA. [Adamson, 1990]

1.3.2 General Procedure

To obtain a sessile drop of a metal or alloy, it is first necessary to heat a small mass of the material in a vacuum or an inert atmosphere at a temperature equal to or greater than its melting point. The sample is usually placed upon a polished ceramic or refractory oxide support. A furnace should be used that will allow temperature measurement via an optical pyrometer. It is also important that the material be in the view of a camera for recording of the shape of the sessile drop. Commonly, a tube furnace is used. The sessile drop image is recorded by self-illumination from one end of the furnace. In many experiments, the sessile drop is illuminated from one end, and its shadow is photographed. The contact angle may be obtained from a photograph of the drop profile either by measuring the angle or by calculating it from the entire drop profile. The camera profile method is accurate to approximately 2° in the measurement of the contact angle.

In order for the contact angle measurements to be considered valid, the measurement must be made when the drop is in the liquid state. Because of nonuniform cooling of the liquid, measurements cannot be made from solidified sessile drops [Kingery, 1959]. It should also be noted that the measurements are accurate only when the drop is symmetrical [Murr, 1974].

Since the substrate material can have an important influence on the shape of a sessile drop and on the calculated value of the interfacial energy, care must be taken in the preparation of the substrate surface and in the selection of the testing atmosphere. A surface smoothness of 1 μm is desired for the surface roughness to be negligible. Greater than 1 μm roughness will affect the measurement of the contact angle. If the contact angle is greater than 90°, surface roughness will increase the angle. In contrast, if the contact angle is less than 90°, surface roughness will decrease the angle.

1.3.3 Associated Calculations

Once accurate measurements of the contact angle have been obtained, calculations of interfacial energy can be made using the Young-Dupre equation. It is necessary, however, to know the values of the liquid/vapor and solid/vapor interfacial energies in order to utilize this equation. These values are available for many pure materials, but have not been reported for most alloy systems. In these cases, direct measurements of the liquid/vapor and solid/vapor interfacial energies must be made via other testing methods. It is common, though, to assume the interfacial energy of an alloy is equal to that of the pure material in order to readily estimate the solid/liquid interfacial energy.

1.3.4 Previous Work on Graphite/Copper Interfaces

To date, very little work has been conducted in the area of Gr/Cu interfaces. Perhaps the most widely referenced study was that of Mortimer and Nicholas [1970, 1971]. This investigation determined the effects of alloying additions on two types of carbon, HX30 and vitreous carbon. Through sessile drop testing in vacuum below 1 x 10^{-5} torr, at 1150°C, they have reported the contact angle of pure Cu on vitreous carbon to be 120°. Alloying additions of Al, Mo, Nb, Ta, Ti, W, U and Zr did little to enhance the wetting of Cu on either of the carbon substrates. Alloys of Cu with B, Ca, Co, Hf, Fe, Mn, Ni, Pt, Re and Sc tested on vitreous carbon substrates produced similar results. The contact angles of these alloys did not differ by more than 25° from that of pure Cu. Mortimer and Nicholas found that the only additions which produced a significant decrease in the contact angle were 1 at% Cr on both substrates and 1 at% V on the vitreous carbon only.

Metallographic examination revealed the presence of reaction products at the interfaces of samples to which carbide forming alloying additions had been made. Four

types of reaction products were identified: continuous layers of uniform thickness, discontinuous layers of near uniform thickness, flakey layers partly detached from the carbon substrate and interfacial area containing many small particals. Most of the samples did not adhere to the substrate, resulting in the presence of discontinuous reaction layers. The reaction product of the Cu-Cr alloy was continuous, and quantitatively determined to be Cr_3C_2. The remaining layers were too thin to analyze.

For their calculations of the interfacial energies, Mortimer and Nicholas have assumed that the substrate/metal interfacial energy is identical for carbon/alloy systems and is appropriate for carbide/alloy systems. Having made this assumption, the Young-Dupre equation for an alloy on a carbon substrate can be written as

$$\gamma_{SV_{carbon}} = \gamma_{LV_{alloy}} \cos\theta_{alloy/C} + \gamma_{SL} \tag{1-6}$$

Replacing the carbon substrate with a reaction product carbide yields

$$\gamma_{SV_{carbide}} = \gamma_{LV_{alloy}} \cos\theta_{alloy/carbide} + \gamma_{SL} \tag{1-7}$$

Two additional assumptions were made for the dilute alloys investigated:

$$\theta_{alloy/carbide} = \theta_{Cu/carbide}$$

$$\gamma_{LV_{alloy}} = \gamma_{LV_{Cu}}$$

Using values of 1239 erg/cm^2 for the surface energy of pure Cu, and 798 erg/cm^2 for the surface energy of carbon, Mortimer and Nicholas have estimated the surface energies of the carbides present in their investigation. They have reported γ_{SV} of Cr_3C_2 to be 975 erg/cm^2 for a $\theta_{Cu/carbide}$ equal to 46.5°. The interfacial energy for Cu/Cr_3C_2 is then calculated to be 130 erg/cm^2, a very small value.

1.4 Alloyed Matrices

1.4.1 Reasoning

Due to the lack of wetting of Cu on Gr, the potential to enhance wetting by alloying the Cu has been investigated. The alloying elements chosen are those which have limited solubility in solid Cu and are potential carbide formers. They include: Cr, Fe, Hf, La, Mn, Nb, Si, Ta, Ti, V, Y and Zr. Most tend to strongly segregate to interfaces. Because these composites are being considered for thermal conductivity critical applications, the addition of alloying element was minimized with the intention of minimizing the thermal conductivity drop. For this reason, an effective alloying addition is defined as one that produces the greatest decrease in contact angle, from that of pure Cu, for the lowest atomic percent addition. The influence of alloying addition on the electrical resistivity, which is inversely proportional to the thermal conductivity, is shown in Figure 1.11.

1.4.2 Phase Diagrams

The Cu-C phase diagram is shown in Figure 1.12. From the diagram, it is evident that there are no reactions between Cu and C, and hence, no intermediate phases that may form. This explains the debonding which occurs in Gr/Cu composites at elevated temperatures. The phase diagrams for the Cu-Cr and Cu-V alloy systems are given in Figures 1.13 and 1.14. As suggested, the alloying elements have limited solubility in solid Cu. The associated carbide phase diagrams are depicted in Figures 1.15 and 1.16. The phase diagrams for the remaining Cu alloys investigated are given in Appendix I. All of the alloying elements chosen can form stable carbide phases.

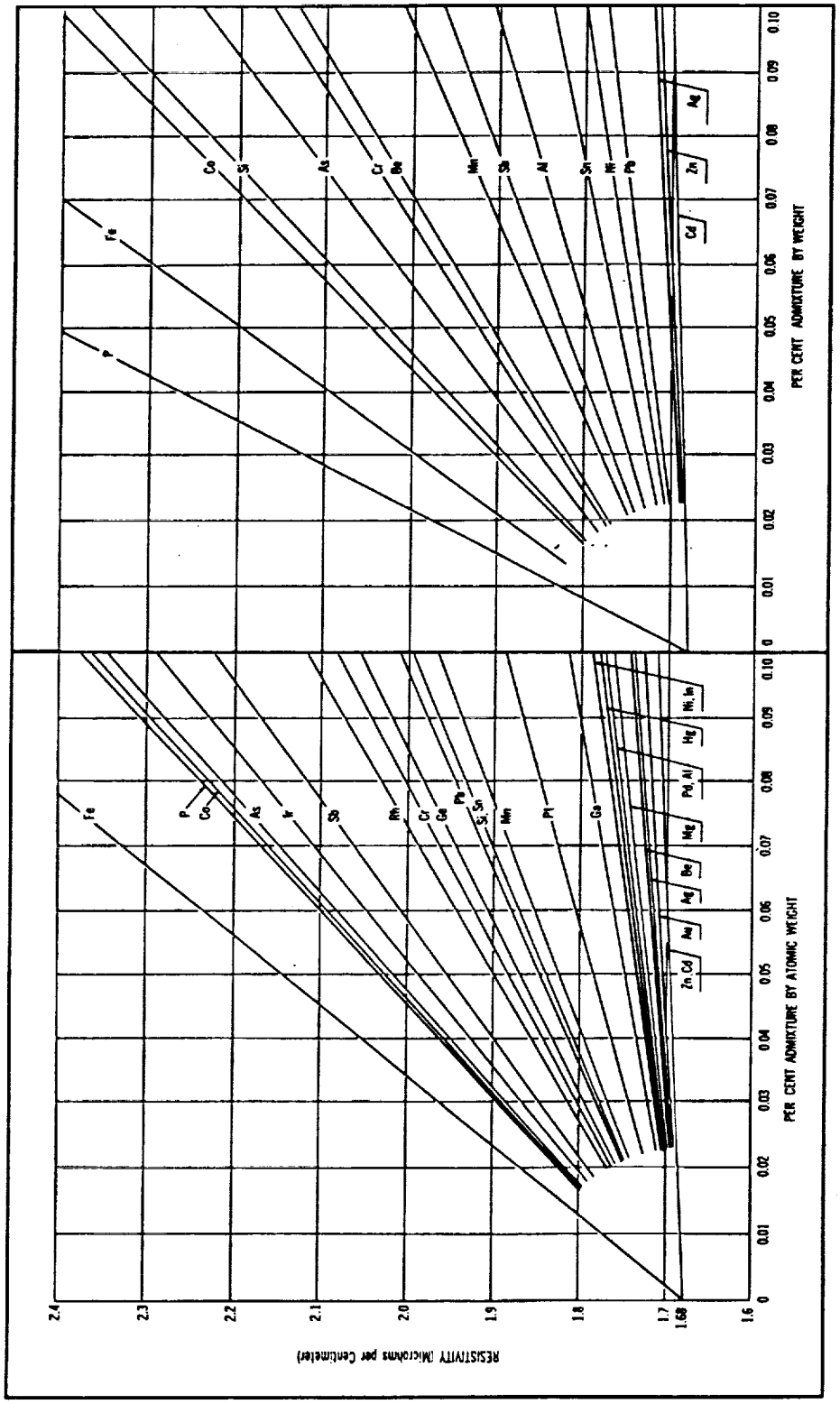

Figure 1.11. Increase of electrical resistivity of copper with admixtures of various elements. [Pawlek and Reichel, 1956]

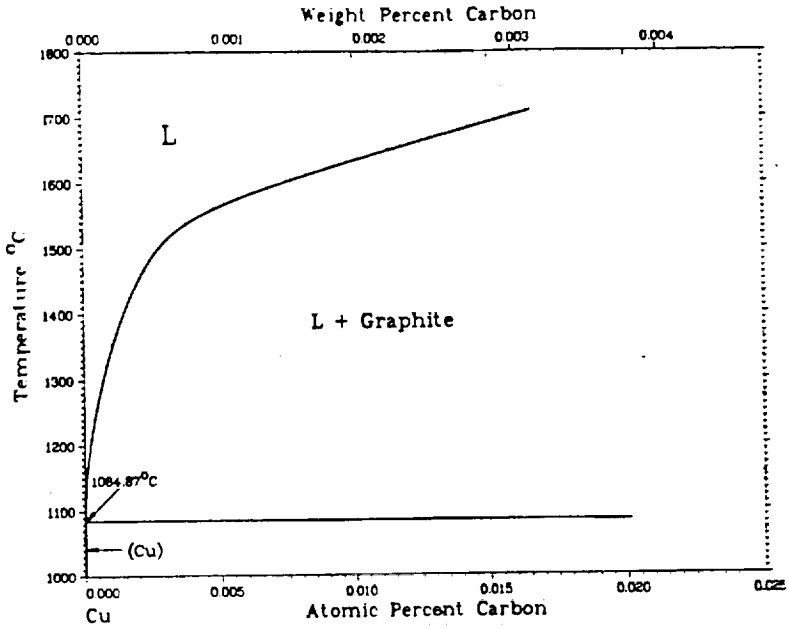

Figure 1.12. Cu-C phase diagram. [Binary Alloy Phase Diagrams, 1986, redrawn from Metals]

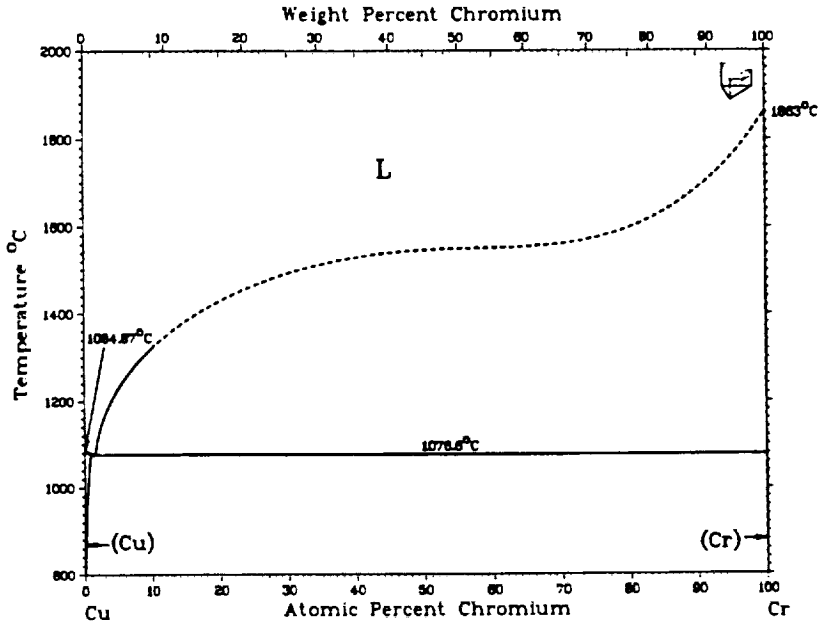

Figure 1.13. Cr-Cu phase diagram. [Chakrabarti and Laughlin, 1984]

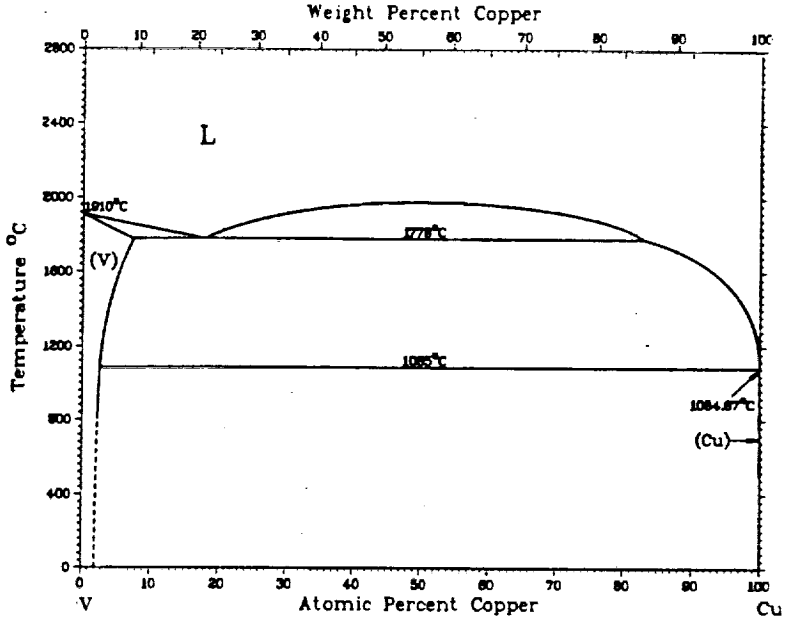

Figure 1.14. V-Cu phase diagram. [Smith and Carlson, 1981]

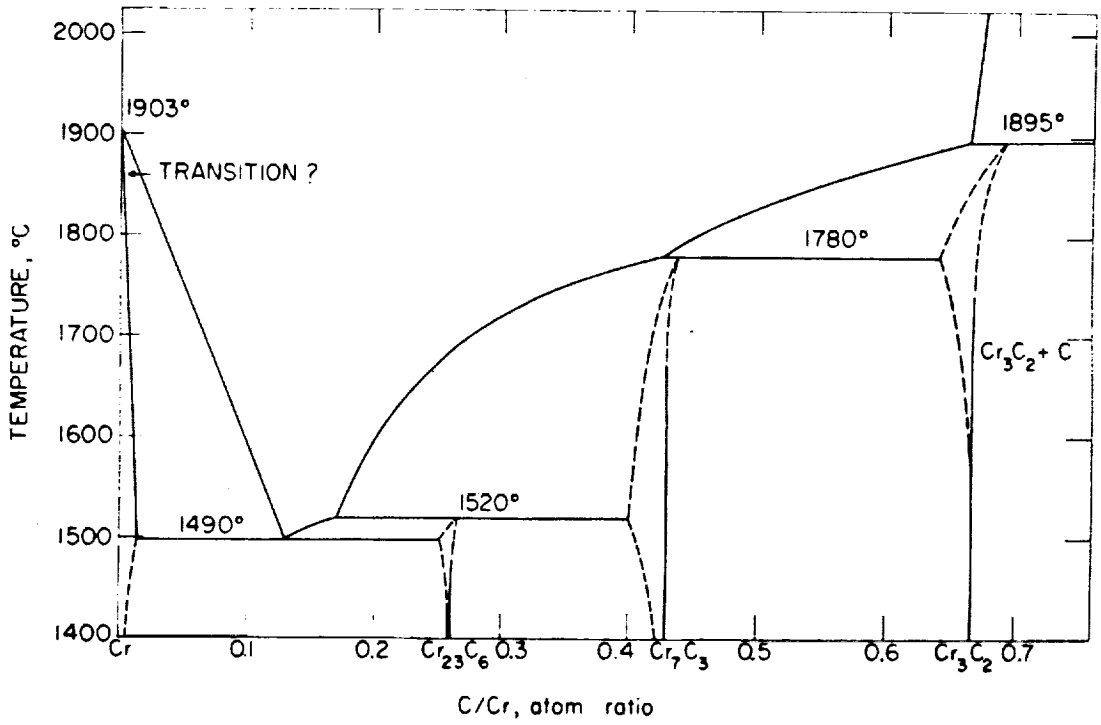

Figure 1.15. Cr-Cr_3C_2 Phase Diagram. [Storms, 1967]

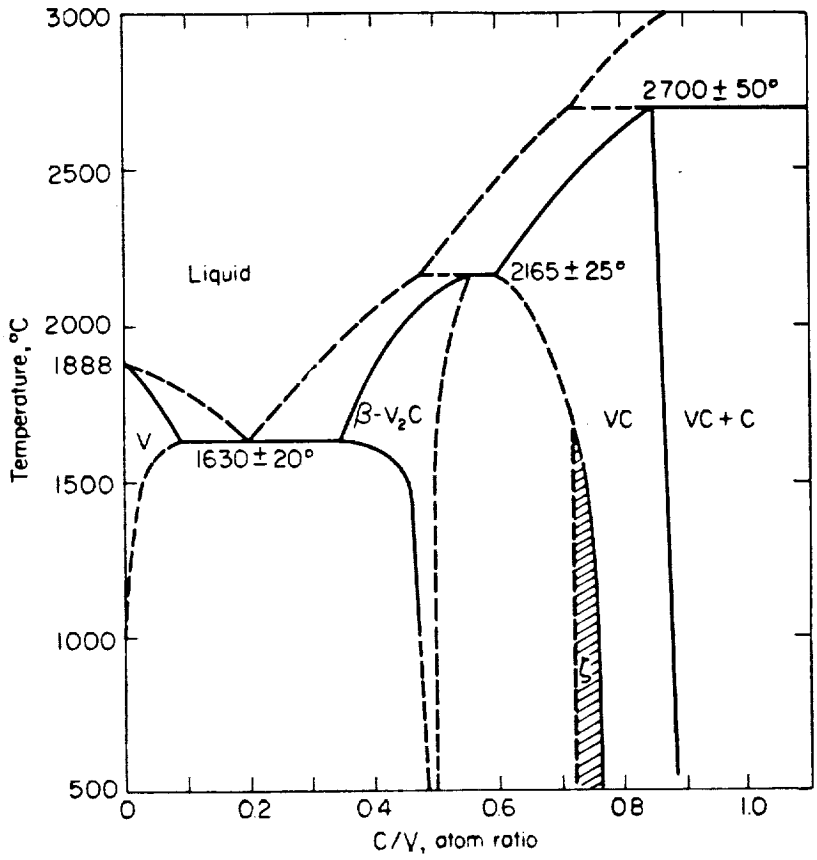

Figure 1.16. V-VC Phase Diagram. [Storms, 1967]

1.5 Diffusion Mechanisms

In order for chemical reactions to take place in condensed phases, it is essential that atoms be able to move about in the crystalline or noncrystalline solid [Kingery, 1981]. Mechanisms by which this can take place include vacancy diffusion and interstitial diffusion. If a new compound is formed between A and B, continuation of the reaction requires that materials diffuse through the intermediate layer. The rate of this diffusion process limits the rate of the reaction.

1.5.1 Bulk Diffusion

The growth in the z direction of a reaction layer phase at the interface of two materials, A and B, is controlled by the bulk diffusion rates of A and B through that phase. The slower of the two is rate limiting.

The location of the reaction layer phase, with respect to the A/B interface is dependent upon the relative bulk diffusion rates of the two materials in the reaction layer. If the diffusion rates are similar in magnitude, the reaction layer will form at the interface and extend equally into material A and material B. On the other hand, if the diffusion rate of B through the reaction layer is faster than that of A, the reaction layer will form primarily in the upward direction into material A. The reverse also holds.

1.5.2 Surface Diffusion

Once formed, it is also possible for a reaction layer to grow outward along the surface of a material. This type of growth is similar to the ledge growth mechanism. Smooth solid/liquid interfaces tend to advance by the lateral growth of ledges [Porter and Easterling, 1981]. Because the ledges are a non-equilibrium feature of an interface, growth is dependent on how the ledges are supplied. One such source of ledges is surface nucleation. If a sufficiently large number of atoms diffuse to the interface of materials A and B to form a disc-shaped layer as shown in Figure 1.17, it is possible

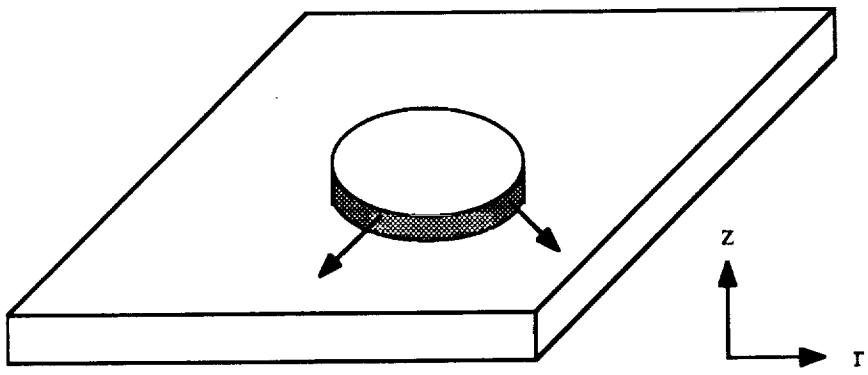

Figure 1.17. Ledge creation by surface nucleation.
[redrawn from Porter and Easterling, 1981]

for the arrangement to become self-stabilized and continue to grow. Once the layer has grown to the size of the A/B interface or contact area, continued growth occurs via surface diffusion. For example, growth due to the diffusing species of material A diffusing along the surface of material B.

At the surface of a phase, an atom moving from one site to another is not constrained to squeezing between surrounding atoms an all sides. Because of this, atomic mobility is greater on the surface and takes place with a lower activation energy . For surface diffusion, the activation energy is about half that for bulk diffusion [Kingery, 1981]. Generally, surface diffusion is considerably faster than bulk diffusion. For this reason, a reaction layer will extend in length or radius much quicker than in height or thickness. An example of the difference in the relative magnitudes of bulk and surface diffusion is shown below. The example is for thorium in tungsten at 1400K [Kingery, 1960].

$$D_{surface} = 0.47 \exp[-66{,}400/RT] = 2.02 \times 10^{-11} \text{ cm}^2/\text{s}$$
$$D_{bulk} = 1.0 \exp[-120{,}000/RT] = 1.84 \times 10^{-19} \text{ cm}^2/\text{s}$$

$$D_{surface} / D_{bulk} = 1.1 \times 10^{8}$$

As shown by this ratio, the surface diffusion is many orders of magnitude faster than the bulk diffusion of this system.

1.6 Overview

The investigation of Gr/Cu-alloy interfaces begins with the determination of an alloy system that wets the Gr substrate. Through sessile drop testing, contact angles were measured for each alloy considered. Using these data, interfacial energy values were calculated. Although there were many alloys considered, only those systems that

exhibited wetting behavior were characterized. The focus of further investigation was the Cu-Cr alloy systems. Some verification of results and trends was done using the Cu-V alloys.

2 EXPERIMENTAL PROCEDURE

2.1 Sessile Drop Test

2.1.1 Material Selection

Additions to Cu of 0.5 at% and 1.0 at% of Cr, Fe, Hf, La, Mn, Nb, Si, Ta, Ti, V, Y and Zr were attempted to produce arc melted and induction melted alloys for sessile drop evaluation. Only partial success was achieved in obtaining the desired alloying additions, as shown later in Table 3.1. Tests were also run using pure Cu as a standard. The chemical composition of each alloy was verified through ICP Emission Spectrometry and Atomic Absorption Spectrophotometry.

2.1.2 Sample Preparation

Testing surfaces of commercial grade H-490 Gr discs of 2.54 cm (1 in) diameter were polished to a 1 μm finish. Cu alloy test specimens of 1.27 cm (0.5 in) diameter and approximately 2mm (0.08 in) height were used. A small number of the Cu alloy test specimens, 0.61, 0.98, 1.10 and 1.22 at% Cr, were cut from available bar stock with diameter of 1.9 cm (0.75 in).

2.1.3 Testing

Sessile drop tests were conducted in 1 atm argon. For each alloy, two to five individual tests were run. The Gr substrate was placed directly on the pancake induction coil of the furnace. A Cu alloy test specimen was placed on top of the Gr as shown in Figure 2.1. Temperatures were monitored using a two wavelength optical pyrometer measuring the temperature of the Gr substrate. To minimize the thermal gradient the Gr was surrounded by Al_2O_3 insulation. Separate tests with thermocouples indicated the thermal gradient between the Gr and Cu to be $\leq 5°C$. After achieving a vacuum $< 4.6 \times 10^{-3}$ Pa (3.5×10^{-5} torr), the furnace was back-filled with

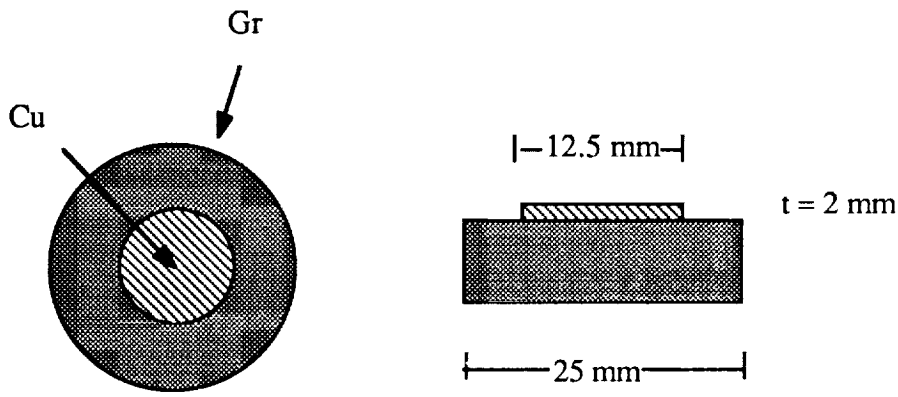

Figure 2.1. Sessile drop test specimen set-up.

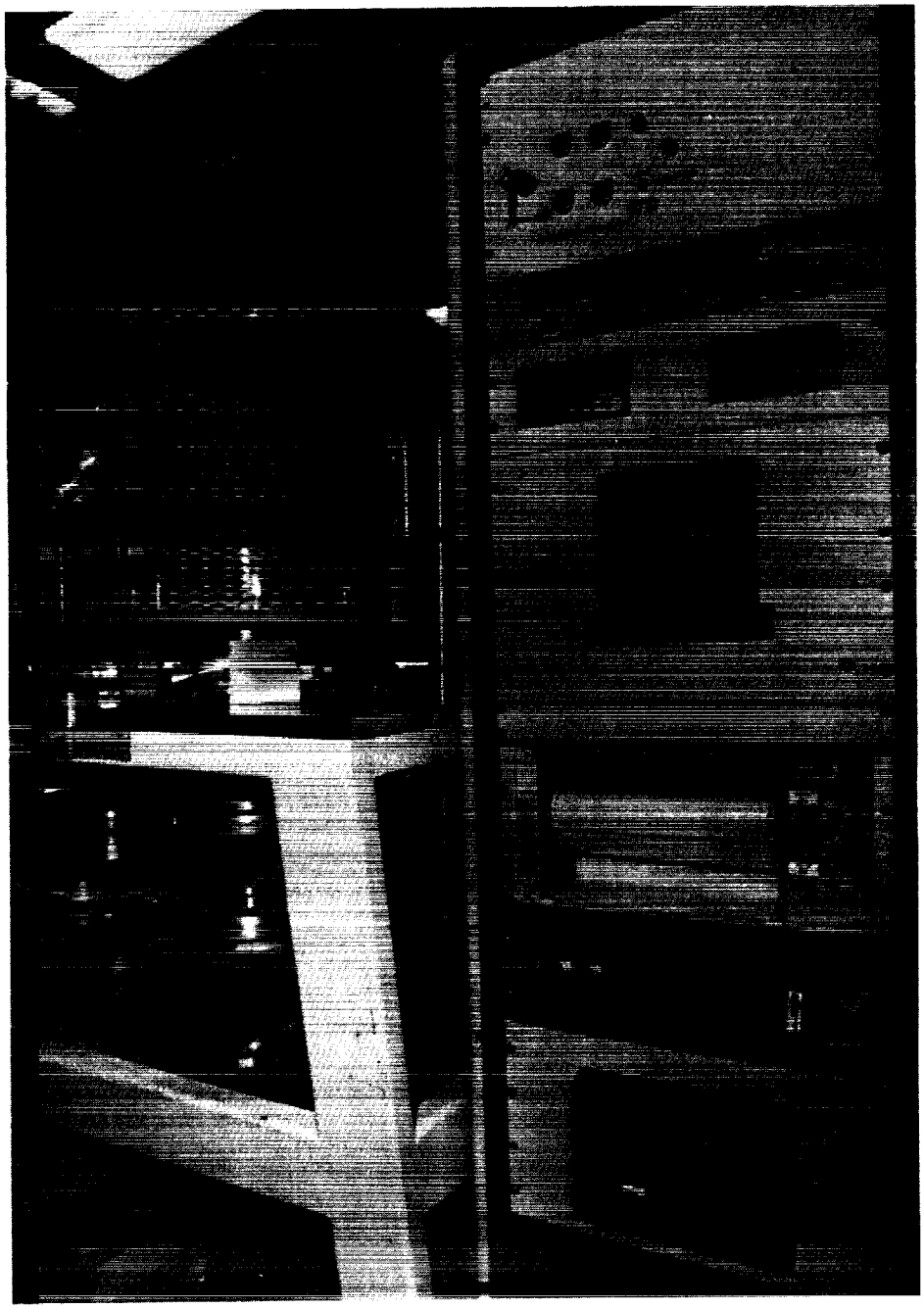

Figure 2.2. Sessile drop testing system.

argon. This procedure was repeated to allow additional flushing of the system. The Cu alloy and the Gr were simultaneously heated to the melting point of the alloy. The test temperature was then raised to a 50°C superheat and held for 3600 s (1 hr). The test was recorded on videotape while the temperature was recorded on a strip chart recorder. The contact angles were measured at 300 s (5 min) intervals during the test using a video monitor. A photograph of the entire system is shown in Figure 2.2.

2.1.4 Measurements

The contact angle was measured manually off the video monitor using a 7x graduated eyepiece. The angle measurements obtained were used in the Young-Dupre equation to calculate the Gr/Cu-alloy interfacial energies.

2.2 Scanning Electron Microscopy

Sessile drop test specimens of the Cu-Cr and Cu-V alloys were cross-sectioned, mounted in epoxy and polished to a 0.25 μm diamond finish. The specimens were examined in the transverse direction using a JOEL 840-A Scanning Electron Microscope (SEM). The continuity and thickness of the reaction layer of each sample was determined. Using a Kevex system, Energy Dispersive Spectroscopy (EDS) analyses were conducted on the Cu-Cr and Cu-V specimens. X-Ray spectra of the bulk alloy, alloy near the interface, the reaction layer, Gr near the interface and bulk Gr were obtained.

2.3 Auger Electron Spectroscopy

Cross-sections of the Cu-Cr alloy sessile drop test specimens were prepared for characterization using a PHI 660 SAM Auger Electron Spectroscopy (AES) system. Line scans of Cu, Cr and C were taken across the interfacial region. This was done to

indicate any segregation of the alloying addition to the interface and to determine the composition of the reaction layer. Survey scans of the reaction layer regions were also taken.

2.4 X-Ray Diffraction

X-ray diffraction methods were used to analyze the reaction layer normal to the surface. Using a Philips APD 3500 diffractometer, an x-ray spectrum was obtained for a reaction layer of the Gr/Cu-0.61at%Cr sessile drop specimen. An untested surface of a Gr substrate was also analyzed for comparison purposes.

3 RESULTS

3.1 Chemical Analysis

The compositions of the alloys tested are listed in Table 3.1. The chemical analyses of these alloys indicate considerable variation from the intended targets of 0.5 at% and 1.0 at% due to difficulties encountered in melting. Also included in the table are the oxygen contents and the amount of addition not tied up as an oxide. The latter quantity was calculated by first assuming an oxide phase and then assuming that all of the oxygen is used in forming that phase. The available additions, in at%, are the amounts which can contribute to the formation of the reaction layer, the lowering of the surface energy of the alloy and the lowering of the contact angle. As indicated, some of the materials have effectively no alloying addition available.

3.2 Sessile Drop Test

3.2.1 Contact Angle Measurements

Photographs of the test specimens were taken from each of the videotapes. An example is shown for pure Cu in Figure 3.1. Contact angle data as a function of alloying element are given in Table 3.2. The values reported are for the equilibrium angle. Most alloys reached equilibrium within 100 s after melting. Based on all the measurements, a pooled standard deviation for the contact angle measurements was calculated to be 16°. The scatter due to the optical measurement system is much less than this value. The major source for error is believed to be the presence of surface oxide on the Cu alloy test specimen. The kinetics of oxide film formation on the Cu-alloy free surface varies for each alloying element, and therefore the stability of the surface oxide also varies.

Table 3.1. Chemical composition of copper alloys.

alloy addition	wt%	at%	O, ppm	oxide	available addition, at%
Cr	0.4	0.49	10	Cr_2O_3	0.487
	0.5	0.61	66		0.593
	0.8	0.98	13		0.977
	0.9	1.10	16		1.096
	1.0	1.22	11		1.217
Fe	0.1	0.11	16	FeO	0.104
	0.4	0.45	10		0.446
Hf	1.0	0.36	46	HfO_2	0.351
	2.0	0.72	254		0.669
La	0.038	0.017	20	La_7O_3	-0.002
Mn	0.4	0.46	26	MnO	0.45
	0.9	1.04	10		1.036
Nb	0.2	0.14	34	NbO	0.127
Si	0.3	0.68	49	SiO_2	0.671
	0.4	0.90	12		0.898
Ta	0.3	0.11	20	Ta_2O_5	0.107
	0.4	0.14	76		0.128
	0.8	0.28	18		0.277
Ti	0.041	0.054	27	TiO_2	0.049
	0.041	0.054	658		-0.076
V	0.3	0.37	34	VO	0.357
	0.8	1.00	57		0.977
Y	0.2	0.14	37	Y_2O_3	0.13
	0.2	0.14	404		0.033
Zr	0.1	0.07	10	ZrO_2	0.068
	0.4	0.28	295		0.222

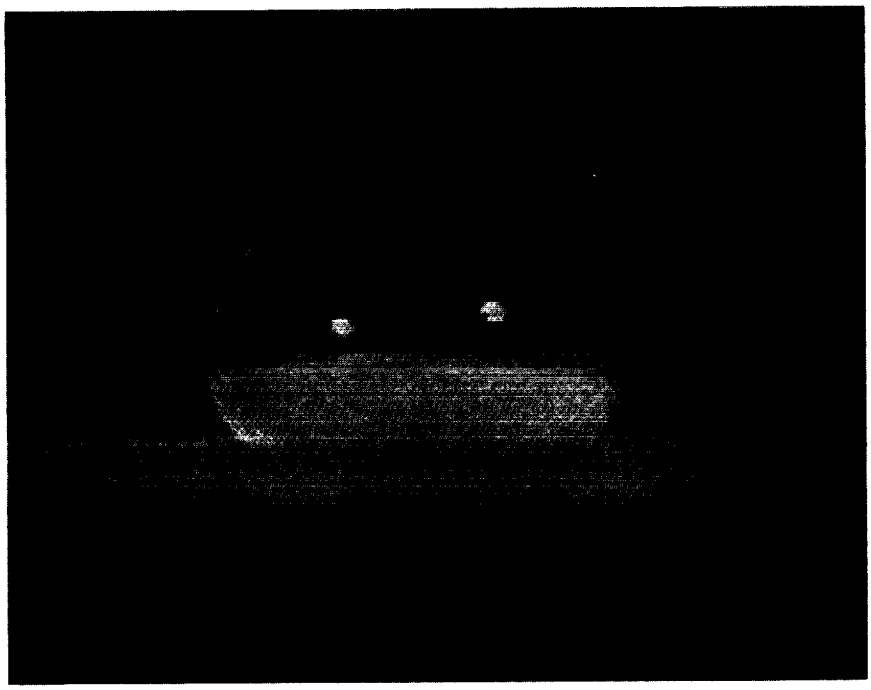

Figure 3.1. Sessile drop test specimen. Pure copper: contact angle 157°.

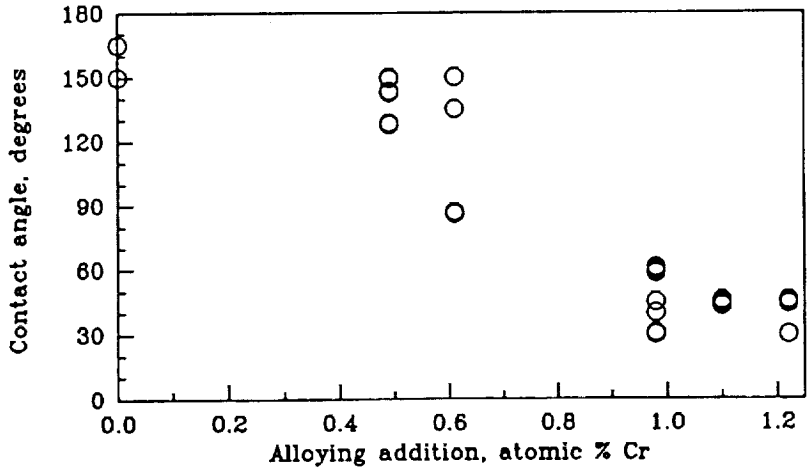

Figure 3.2. Contact angle as a function of Cr addition.

Table 3.2. Graphite/Cu-alloy sessile drop test results.

Cu-alloy addition	at%	contact angle, °	$\gamma_{Gr/Cu}$ mJ/m^2	adherence to Gr
Cu		157	1975	no
Cr	0.49	140	1778	yes
	0.61	114	1318	no
	0.98	60	159	yes
	1.10	45	-106	yes
	1.22	41	-167	yes
Fe	0.11	146	1858	no
	0.45	135	1702	no
Hf	0.36	90	798	no
	0.72	80	576	no
La	0.017	138	1748	no
Mn	0.46	142	1858	no
	1.04	135	1702	no
Nb	0.14	140	1778	no
Si	0.68	157	1975	no
	0.90	150	1906	no
Ta	0.11	130	1620	no
	0.14	132	1654	no
	0.28	142	1806	no
Ti	0.054	128	1585	no
	0.054	119	1418	no
V	0.37	128	1585	no
	1.00	45	-106	yes
Y	0.14	111	1256	no
	0.14	144	1833	no
Zr	0.07	113	1298	no
	0.28	111	1256	no

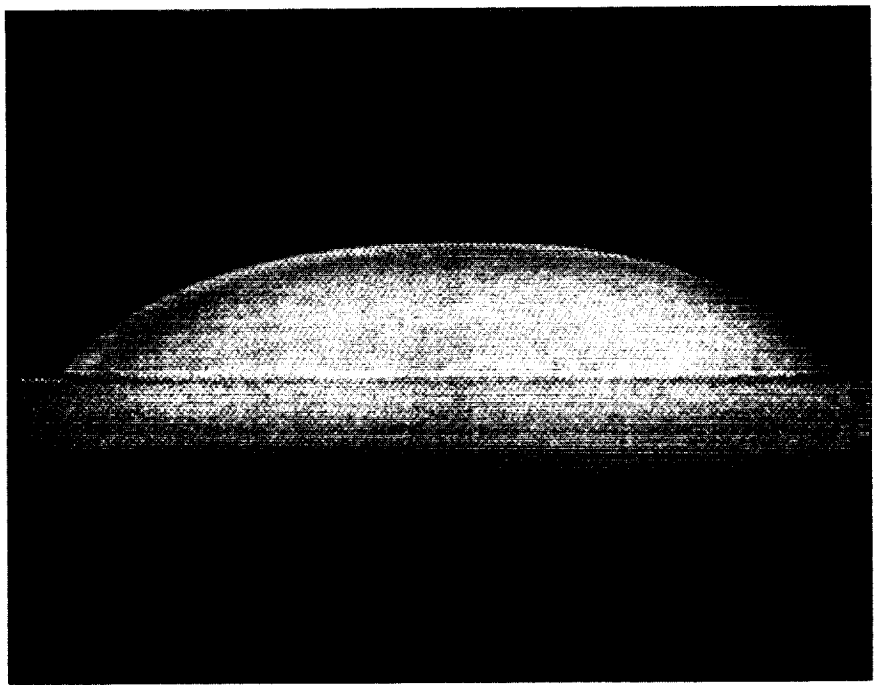

Figure 3.3. Sessile drop test specimen. Cu-1.10at%Cr: contact angle 45°.

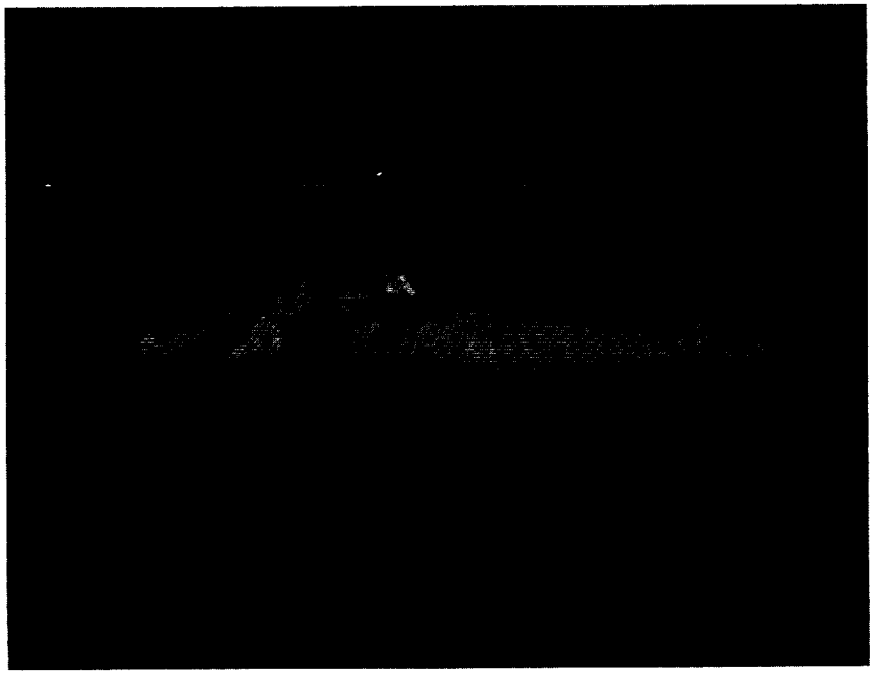

Figure 3.4. Sessile drop test specimen. Cu-1.00at%V: contact angle 45°.

Additions of Cr, Hf, V, Y and Zr significantly decreased the contact angle from that of pure Cu. Angles of 111° were measured for both Y and Zr, 80° for Hf and as low as 41° and 45° for Cr and V respectively. The change in contact angle, from that of pure Cu, is easily observed in the photographs of the Cu-1.10at%Cr and Cu-1.00at%V sessile drops which are shown in Figures 3.3 and 3.4. As indicated in Table 3.2, additions of less than 0.1 at% La or Ti result in a slightly decreased contact angle, whereas much greater additions of many of the other alloying elements are needed to produce the same effect. The raw data for the contact angle measurements as a function of Cr addition are plotted in Figure 3.2. By increasing the amount of Cr addition, the contact angle of the Cu alloy on Gr can be reduced. The results for the Cu-Cr alloys correspond to those found by others [Mortimer and Nicholas, 1970; Nogi, Osugi and Ogino, 1990; Nicholas and Mortimer, 1971].

3.2.2 Adherence

The adherence of the Cu alloy test specimen to the Gr substrate is reported in Table 3.2. The only alloys found to adhere to the Gr surface were those which resulted in significant contact, i.e. Cr and V at amounts of approximately 1 at% or greater. Although the Cu-0.49at%Cr alloy adhered to the Gr, this can be attributed to the smaller size of test specimen as compared to the other Cu-Cr alloys. This smaller size provided a much smaller contact area and therefore a smaller area over which cooling stresses can affect the continuity of the reaction layer formed, and in turn, the adherence to the Gr substrate.

3.2.3 Gr/Cu Interfacial Energy Calculations

Using the Young-Dupre equation and assuming values for the free surface energy of Cu and the free surface energy of Gr, estimates of the Gr/Cu interfacial energy can be made. Values of 1279 mJ/m^2 for the Cu [Murr, 1974; Kingery, 1959] and 798

mJ/m^2 for the Gr [Mortimer and Nicholas, 1970] were used in the calculations. The value for Cu was assumed to be constant with alloying addition and alloying level. Interfacial energy values are listed in Table 3.2 for the Gr/Cu systems investigated.

Some degradation of Gr surfaces, indicated by discoloration found in the areas not covered by the Cu alloy test specimens, was observed. This indicates a reaction occurred at the Gr surface which may change the value of $\gamma_{Gr/v}$.

3.3 Microscopy

3.3.1 Scanning Electron Microscopy

Micrographs of each Cu-Cr alloy were obtained using the Scanning Electron Microscope. This was done to establish the presence of a reaction layer at the interface, and to determine its thickness and continuity. Figures 3.5 through 3.9 contain micrographs of Cu-0.49, 0.61, 0.98, 1.10 and 1.22 at%Cr. As indicated in the figures, the reaction layers formed at the Gr/Cu-alloy interfaces of the samples containing lower amounts of Cr, 0.49 and 0.61 at%, are discontinuous and 0.2 and 1.3 μm thick, respectively. The higher alloyed interfaces exhibit continuous reaction layers of approximately 1 μm thickness.

The Cu-V alloys were also examined. Micrographs of Cu-0.37 and 1.00 at%V are shown in Figures 3.10 and 3.11. The Cu-V alloys follow the trend indicated by the Cu-Cr alloys. The Cu-0.37at%V alloy reveals a 5 μm thick discontinuous reaction layer at the interface, while the Cu-1.00at%V alloy forms a 15 μm thick continuous reaction layer. The reaction layer formed at the interface of both sessile drop test specimens is columnar in nature.

Figures 3.12 through 3.14 examine the edges of the sessile drops and the extent of the reaction layer associated with the Cu-1.10at%Cr and Cu-1.00at%V alloys. As

ORIGINAL PAGE
BLACK AND WHITE PHOTOGRAPH

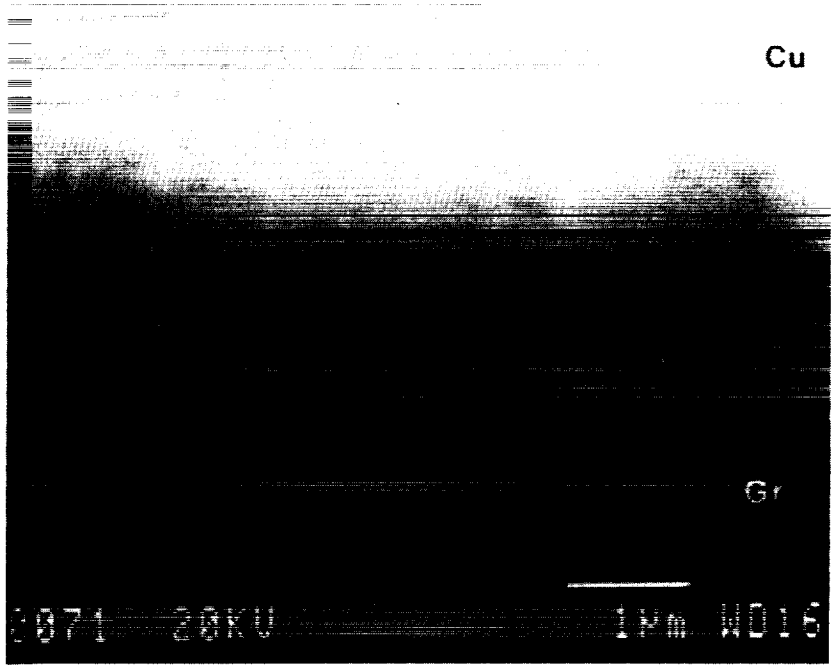

Figure 3.5. SEM micrograph of Cu-0.49at%Cr sessile drop specimen. Discontinuous reaction layer, 0.2 μm thick.

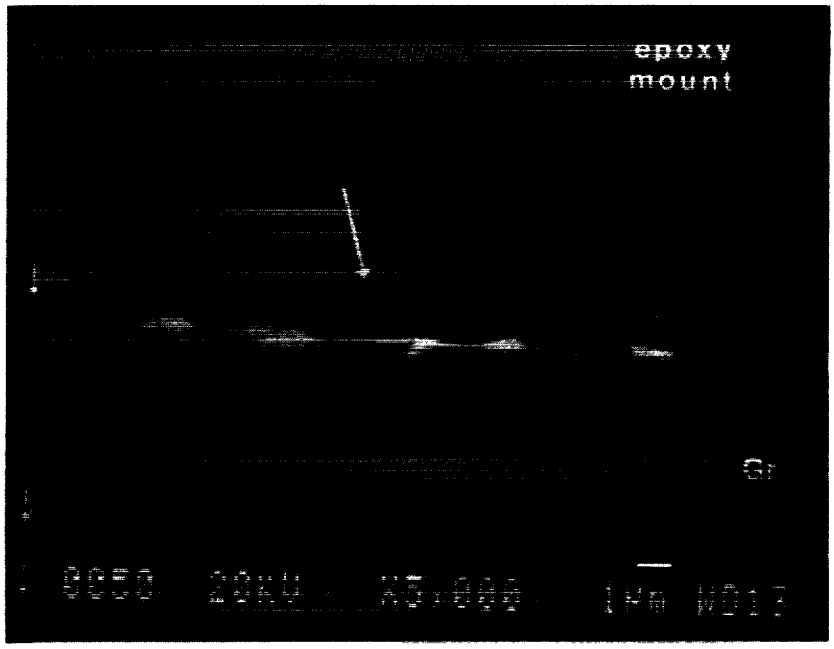

Figure 3.6. SEM micrograph of Cu-0.61at%Cr sessile drop specimen. Discontinuous reaction layer on graphite substrate, 1.3 μm thick.

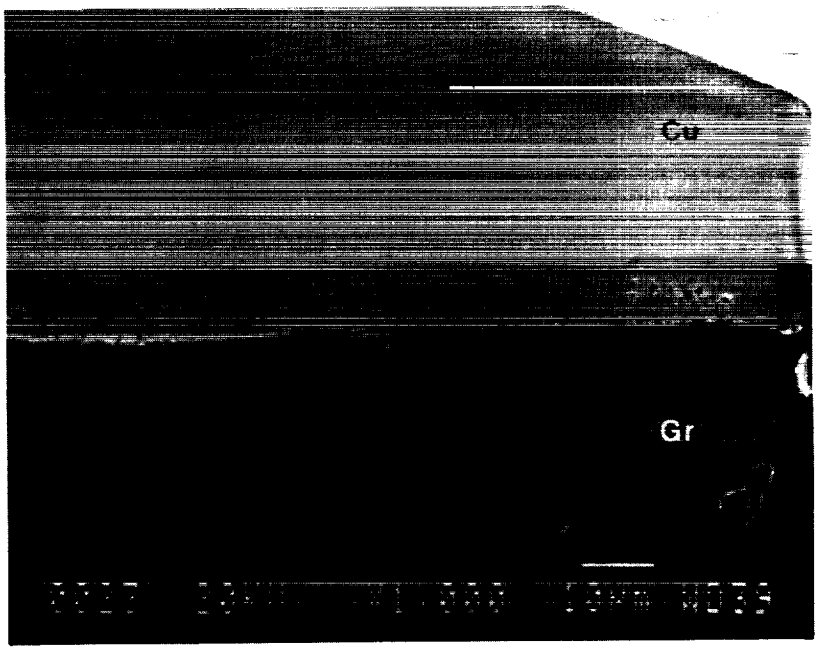

Figure 3.7. SEM micrograph of Cu-0.98at%Cr sessile drop specimen. Continuous reaction layer, 9 μm thick.

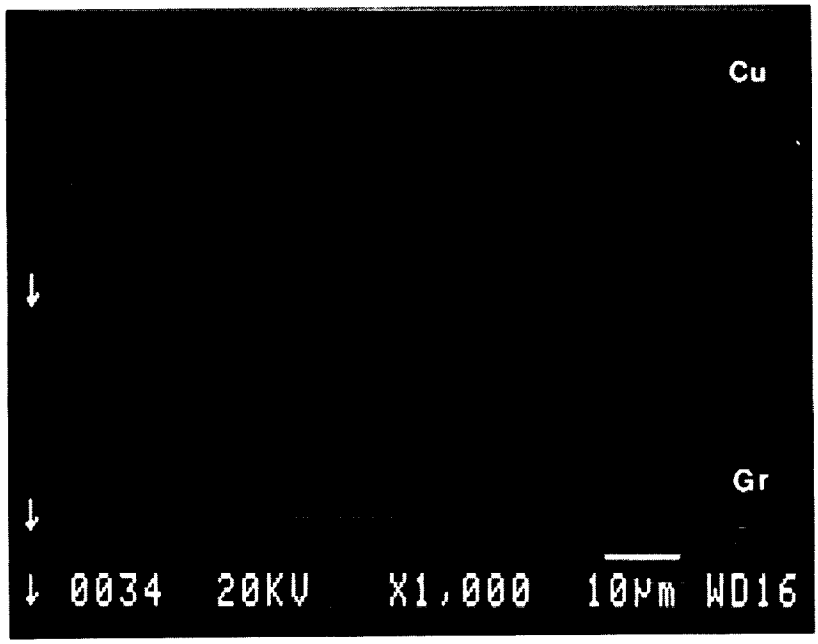

Figure 3.8. SEM micrograph of Cu-1.10at%Cr sessile drop specimen. Continuous reaction layer, 8 μm thick.

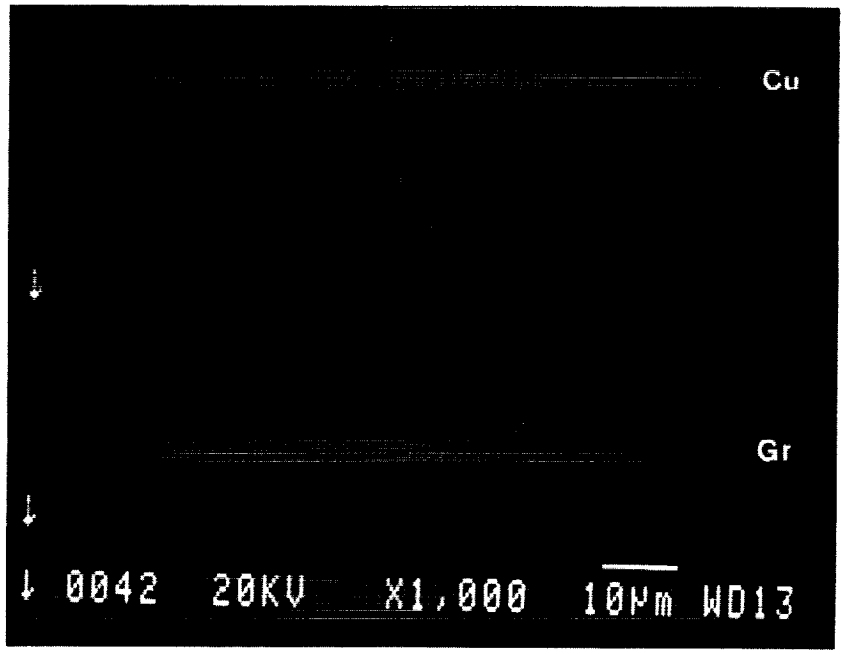

Figure 3.9. SEM micrograph of Cu-1.22at%Cr sessile drop specimen. Continuous reaction layer, 10 µm thick.

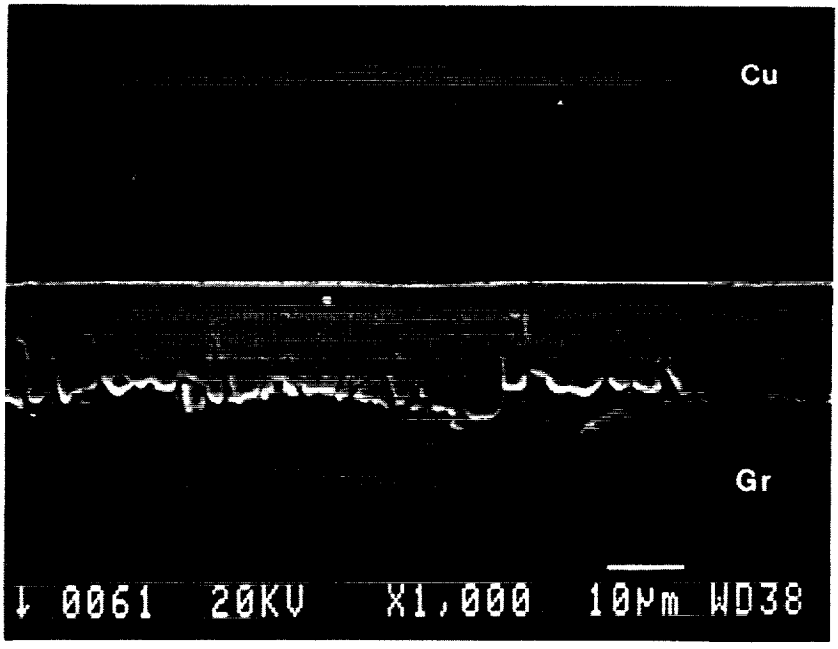

Figure 3.10. SEM micrograph of Cu-1.00at%V sessile drop specimen. Continuous reaction layer, 15 µm thick.

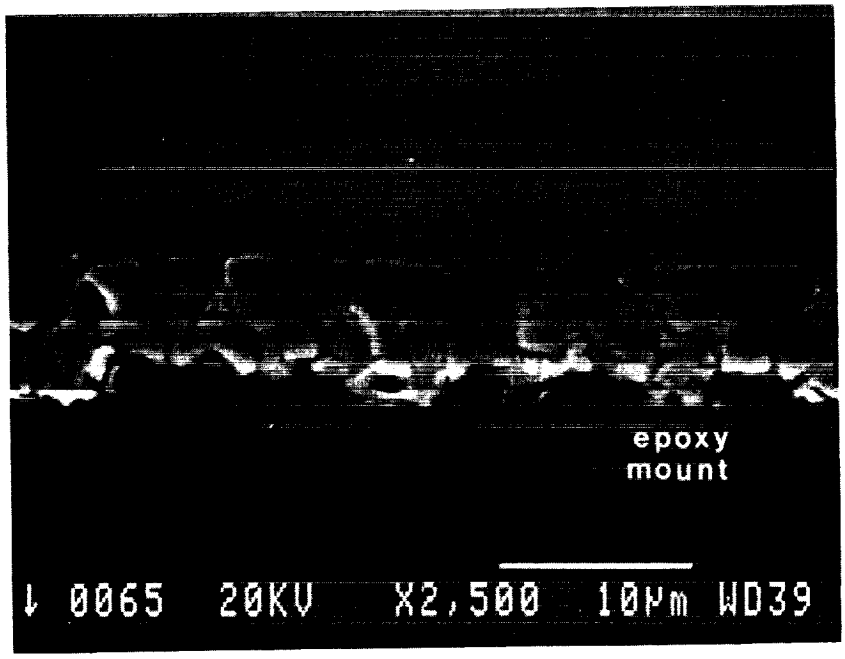

(a.) Area of Cu alloy adherent to reaction layer.

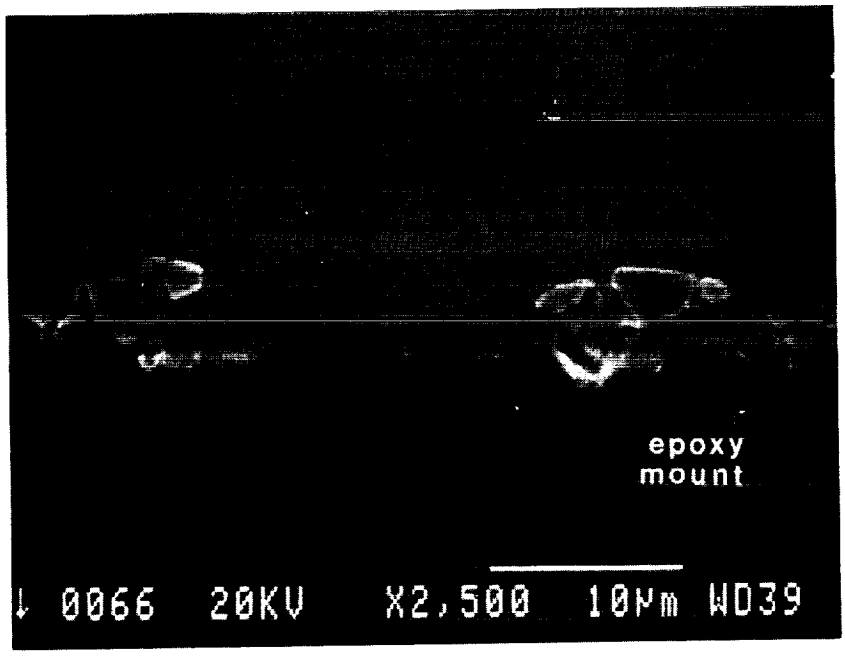

(b). Area of Cu alloy not adherent to reaction layer.

Figure 3.11. SEM micrograph of Cu-0.37at%V sessile drop specimen. Discontinuous reaction layer on Cu alloy, 5 µm thick.

ORIGINAL PAGE
BLACK AND WHITE PHOTOGRAPH

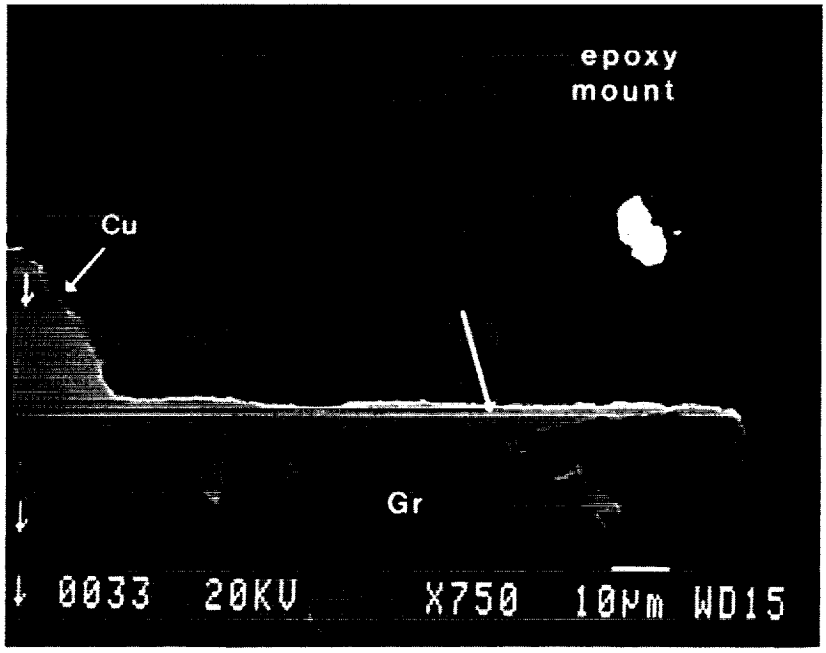

Figure 3.12. SEM micrograph of Cu-1.10at%Cr sessile drop specimen. Reaction layer extends along Gr surface.

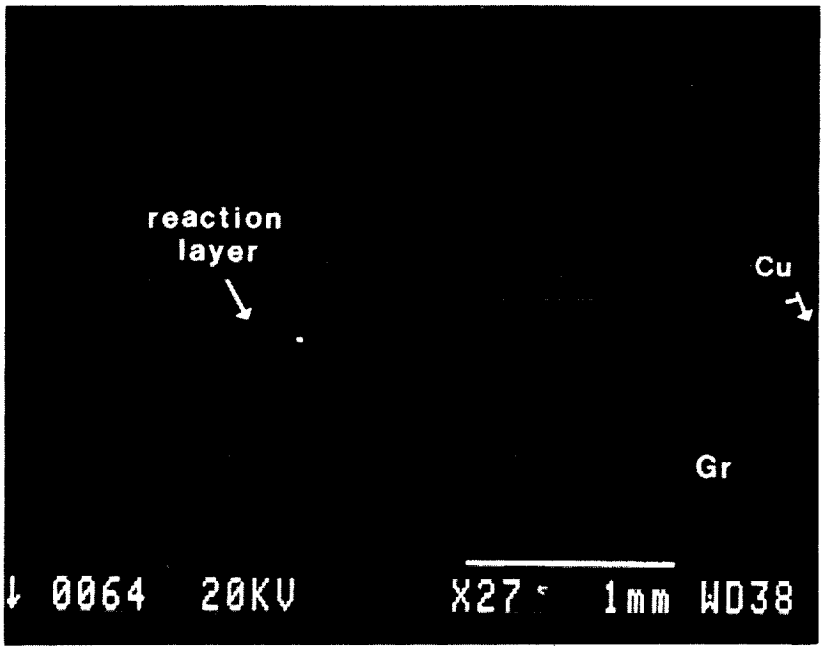

Figure 3.13. SEM micrograph of Cu-1.00at%V sessile drop specimen. Reaction layer extends > 3.5 mm along Gr surface.

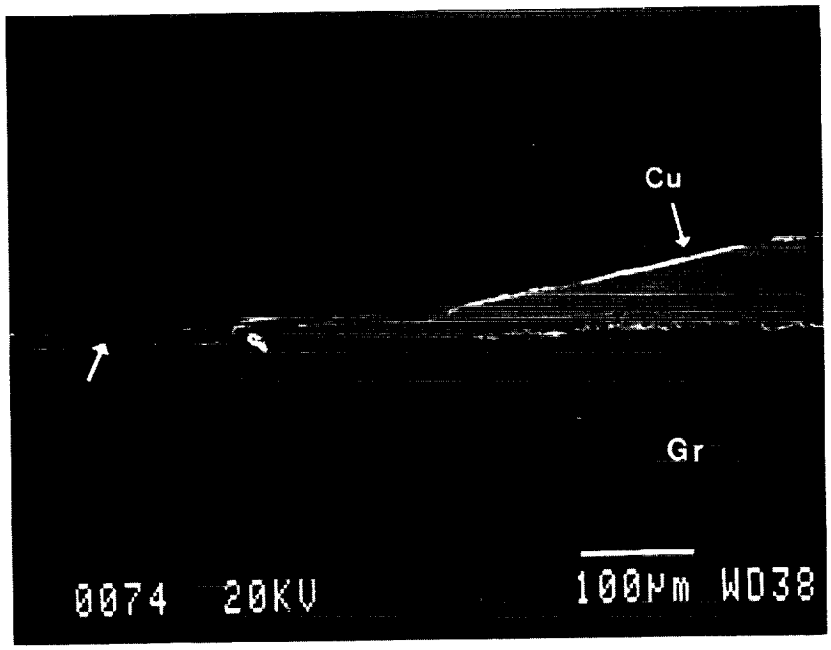

(a.) Extension of reaction layer at edge of Cu-V sessile drop.

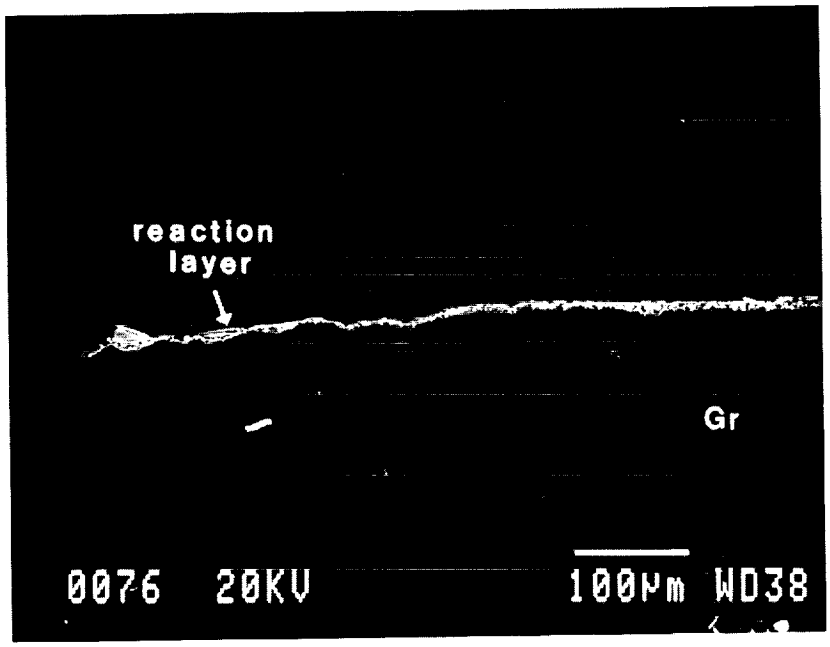

(b). Outer edge of reaction layer extension.

Figure 3.14. SEM micrograph of Cu-1.00at%V sessile drop specimen. Reaction layer extends along Gr surface.

indicated, by both the Cu-Cr and Cu-V alloys, the reaction layer extends along the surface of the Gr substrate approximately 0.1 mm (100 μm) beyond the edges of the sessile drops. The reaction layer formed at the Gr/Cu-1.00at%V interface extends more than 3.5 mm in the radial direction, as shown in Figure 3.13. A higher magnification view of that reaction layer is given in Figure 3.14. The Cu-V alloy saw a much higher temperature than the Cu-Cr alloy. This may account for the much farther surface diffusion distance.

Stress induced cracking occurred between the sessile drop and the Gr substrate during metallographic preparation of many of the test specimens which revealed that the reaction layer formed at the Gr/Cu-Cr interface in strongly adherent to the Gr. The separation of the Cu from the Gr at the interface of the Cu-1.22at%Cr sessile drop test specimen is shown in Figure 3.15. Figure 3.16 and 3.17 clearly indicate the adherence of the reaction layer to the Gr substrate. A closer look at the Cu-0.37at%V test specimen in Figure 3.11a suggests that the reaction layer which formed at its interface is more adherent to the Cu-V alloy.

The contact angle reported can be observed in the micrographs which include the outer edge of the sessile drop specimen. This is especially obvious in Figure 3.18 of the Cu-1.00at%V specimen. A shrinkage cavity is present in the alloy, along the bottom surface. The reaction layer is continuous across the Gr substrate where this gap has formed. By examining the edges of the cavity, along the Gr, the 45° wetting angle is evident. Also shown in Figures 3.12 through 3.14 is the spreading of the Cu alloy along the reaction layer. From the micrographs, it is apparent that the contact angles reported are those of the Cu alloy on the reaction layer, not on the Gr. The outer edges of the reaction layer exhibit a near zero contact angle with the Gr substrate, as shown in Figures 3.12, 3.14b and 3.17. It can also be seen, with the Cu-Cr alloys, that the

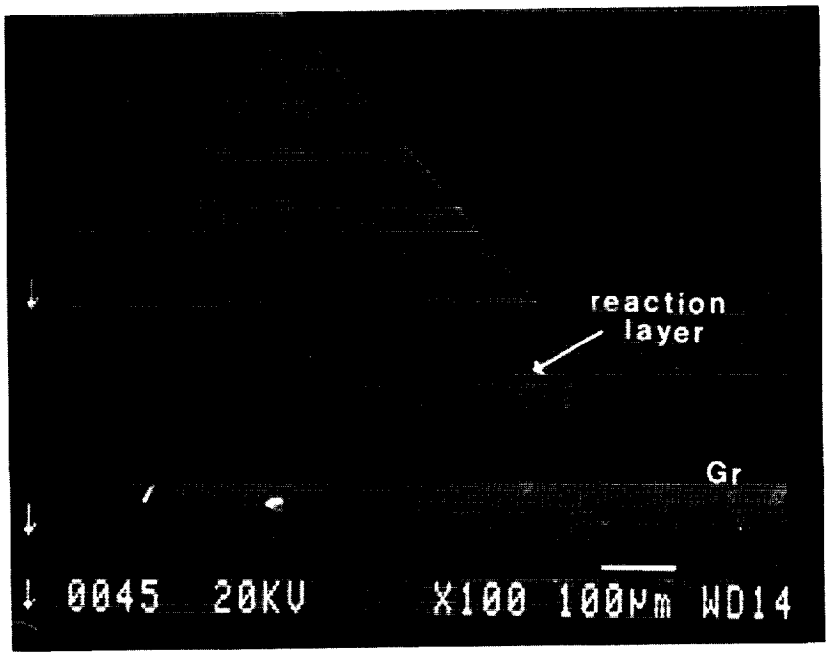

(a.) Low magnification.

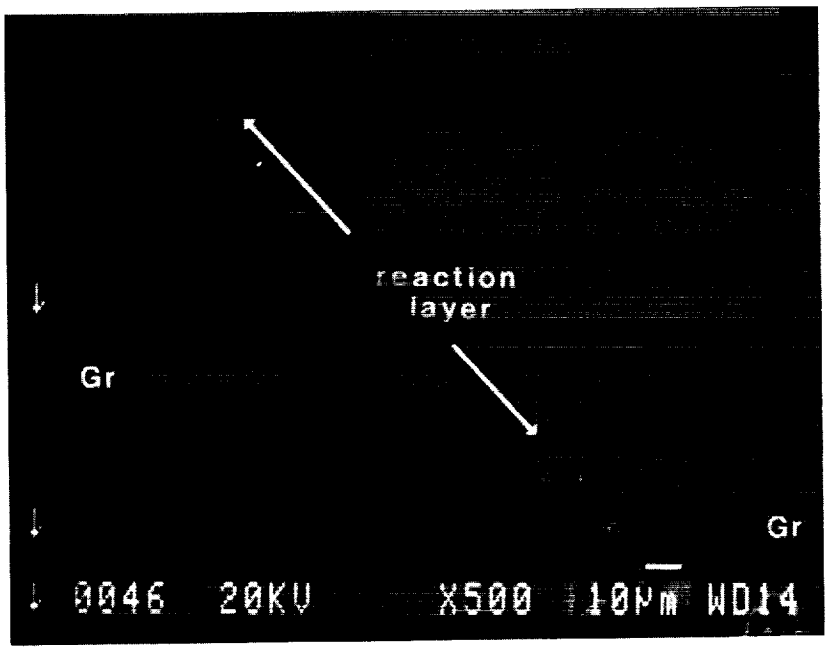

(b). Higher magnification.

Figure 3.15. SEM micrograph of Cu-1.22at%Cr sessile drop specimen. Cu is separated from Gr at reaction layer.

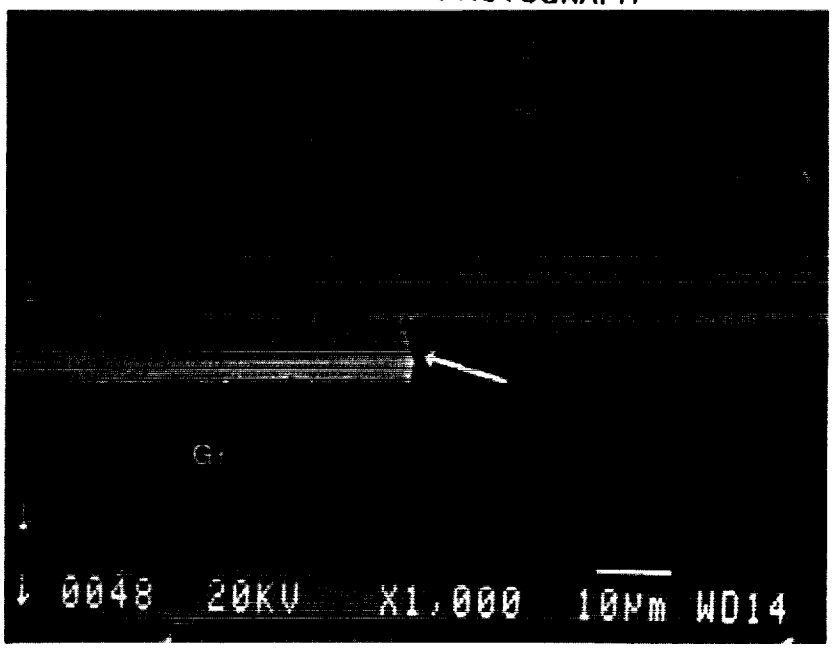

Figure 3.16. SEM micrograph of Cu-1.22at%Cr sessile drop specimen. Reaction layer is separated from Cu at Cu/reaction layer interface.

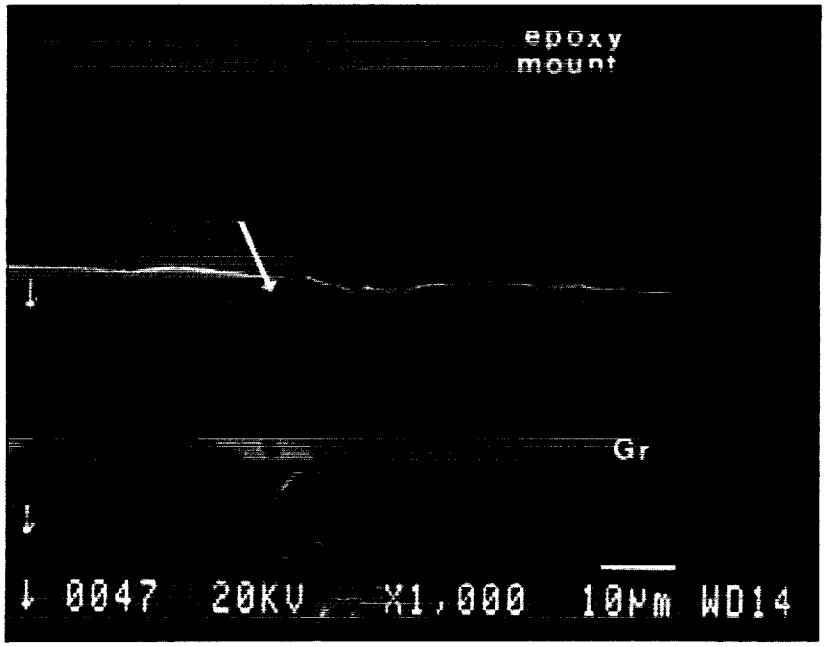

Figure 3.17. SEM micrograph of Cu-1.22at%Cr sessile drop specimen. Reaction layer is adherent to Gr surface.

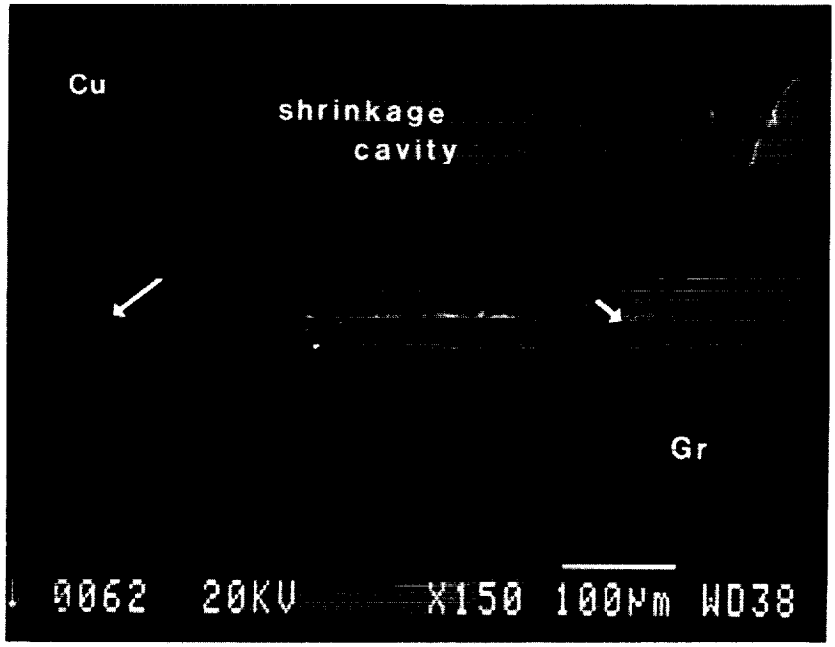

Figure 3.18. SEM micrograph of Cu-1.00at%V sessile drop specimen. Reaction layer is continuous. Wetting angle of 45° between Cu and reaction layer.

Table 3.3. Summary of scanning electron microscopy analyses of Cu-Cr and Cu-V alloys.

at. % addition	description of layer	layer thickness, mm	contact angle	Cu to Gr adherence
0.49 Cr	discontinuous	0.2	140	yes
0.61	discontinuous	1.3	114	no
0.98	continuous	9	60	yes
1.10	continuous	8	45	yes
1.22	continuous	10	41	yes
0.37 V	discontinuous	5	128	no
1.00	continuous	15	45	yes

reaction layer extends in thickness equally up into the alloy and down into the Gr. It is believed that the reaction layers present at the Gr/Cu-V alloy interfaces are formed primarily above the plane of the Gr surface.

A summary of the information obtained during the SEM analyses is given in Table 3.3. The table describes the continuity of the reaction layer and its thickness, the contact angle measured via sessile drop testing and the adherence of the Cu alloy to the Gr substrate. Data for the Cu-Cr and Cu-V alloys are included.

3.3.2 Energy Dispersive Spectroscopy

The Cu-Cr and Cu-V alloy sessile drop test specimens were characterized using Energy Dispersive Spectroscopy. This was done in order to qualitatively identify the chemical composition of the reaction layer phase. Information regarding segregation of the alloying addition to the interface was also obtained. The spectra for the Cu-1.22at%Cr sessile drop test specimen are included in Figures 3.19 through 3.23. The bulk alloy is shown to be comprised of Cu and a trace amount of Cr. The region, in the alloy, located just above the reaction layer shows a slight increase in Cr concentration. This is due to an overlap of the signal from the Cr in the reaction layer. An increase in the bulk alloy would otherwise indicate uphill diffusion. The reaction layer is shown to be primarily Cr with some C signal being indicated. Just below the reaction layer, into the Gr substrate, small amounts of Cr are picked up which can also be attributed to a signal overlap problem. The Gr bulk, as expected, shows only a very strong C peak. These results are representative of those found for the remaining Cu-Cr alloys.

The same series of spectra were obtained for the Cu-1.00at%V sessile drop test specimen and are given in Figures 3.24 through 3.29. The trends are the same as those shown for the Cu-Cr alloys. The only difference occurred during the analysis of the

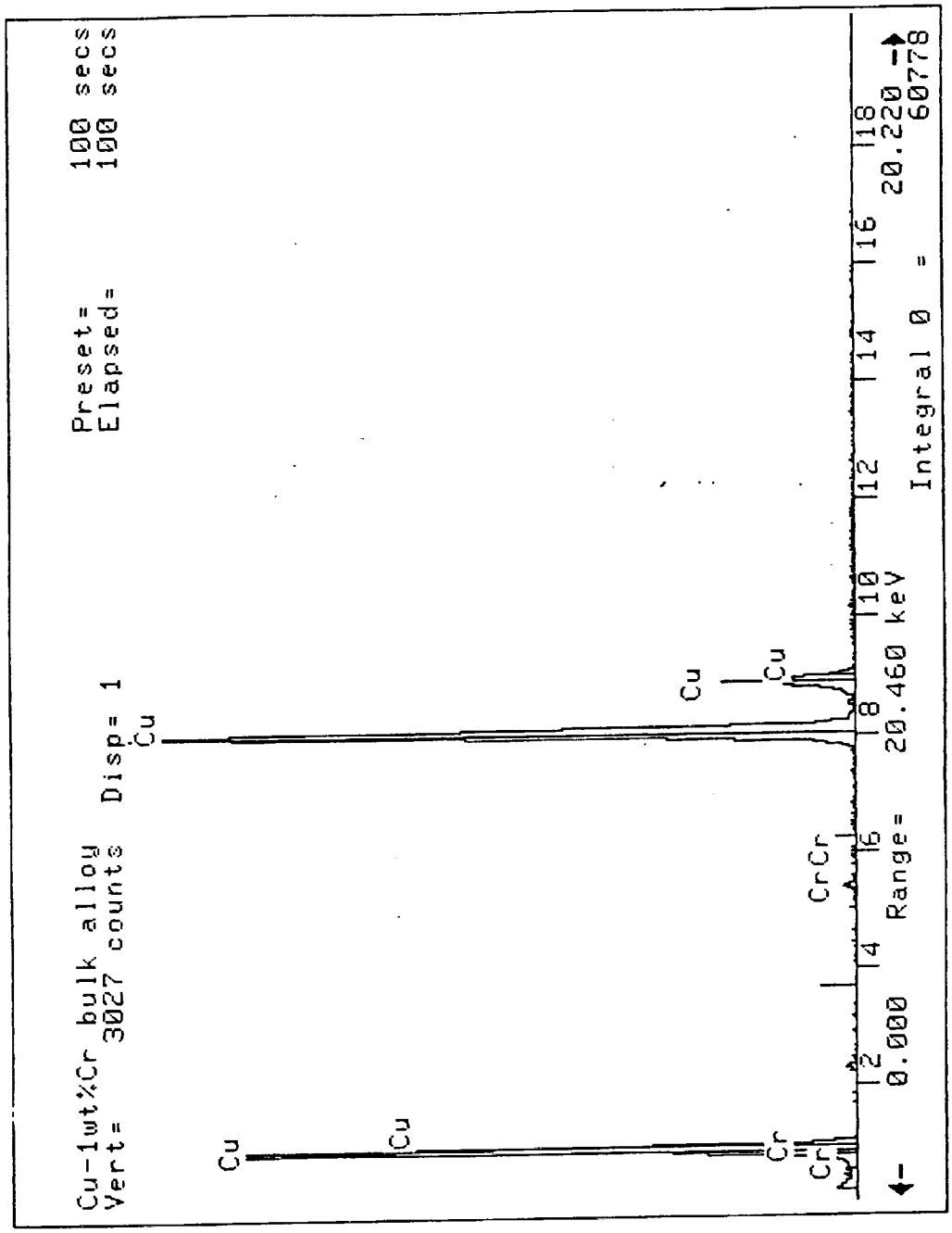

Figure 3.19. EDS spectrum of Cu-1.22at%Cr sessile drop specimen; bulk alloy.

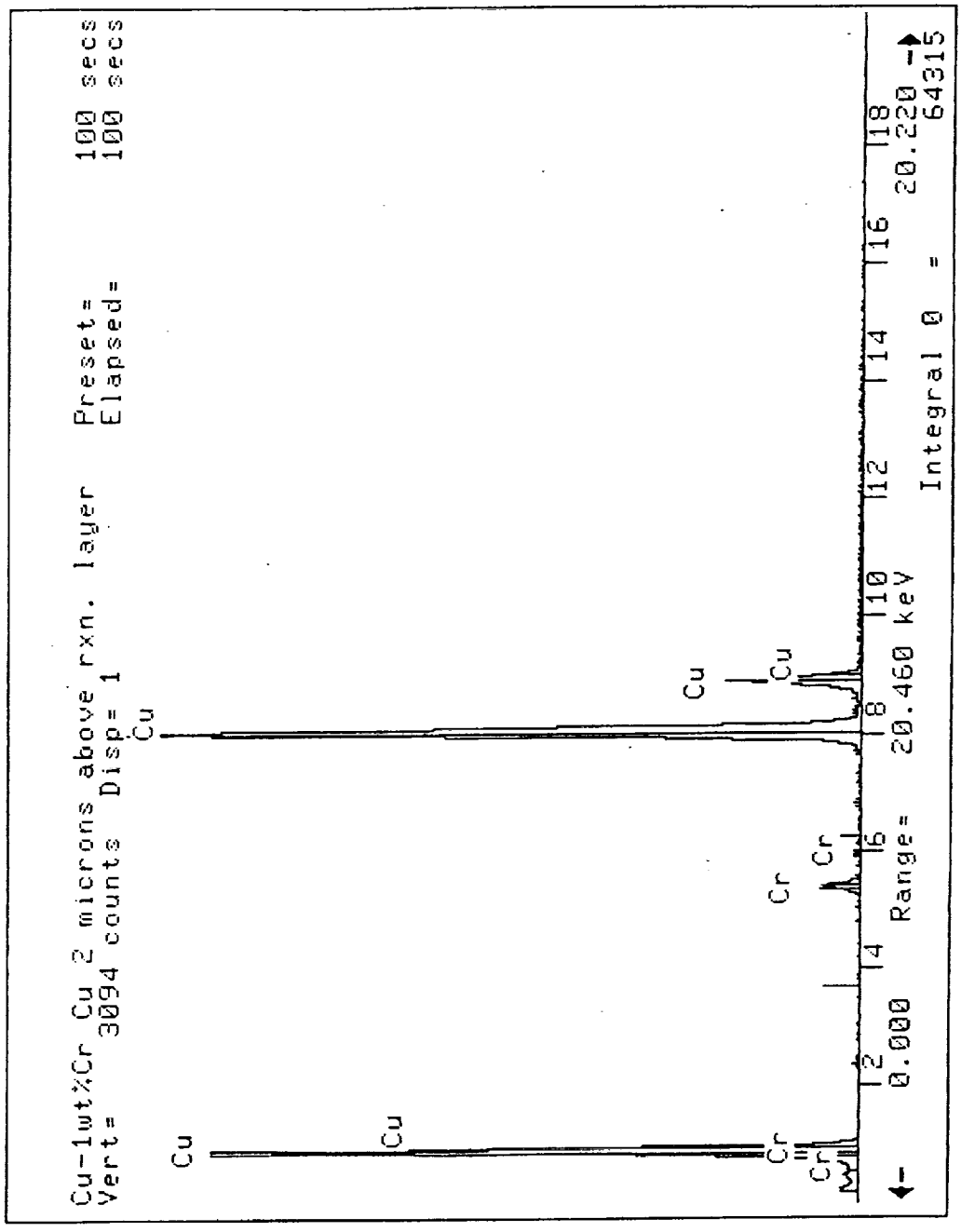

Figure 3.20. EDS spectrum of Cu-1.22at%Cr sessile drop specimen: alloy, 2 μm above the reaction layer.

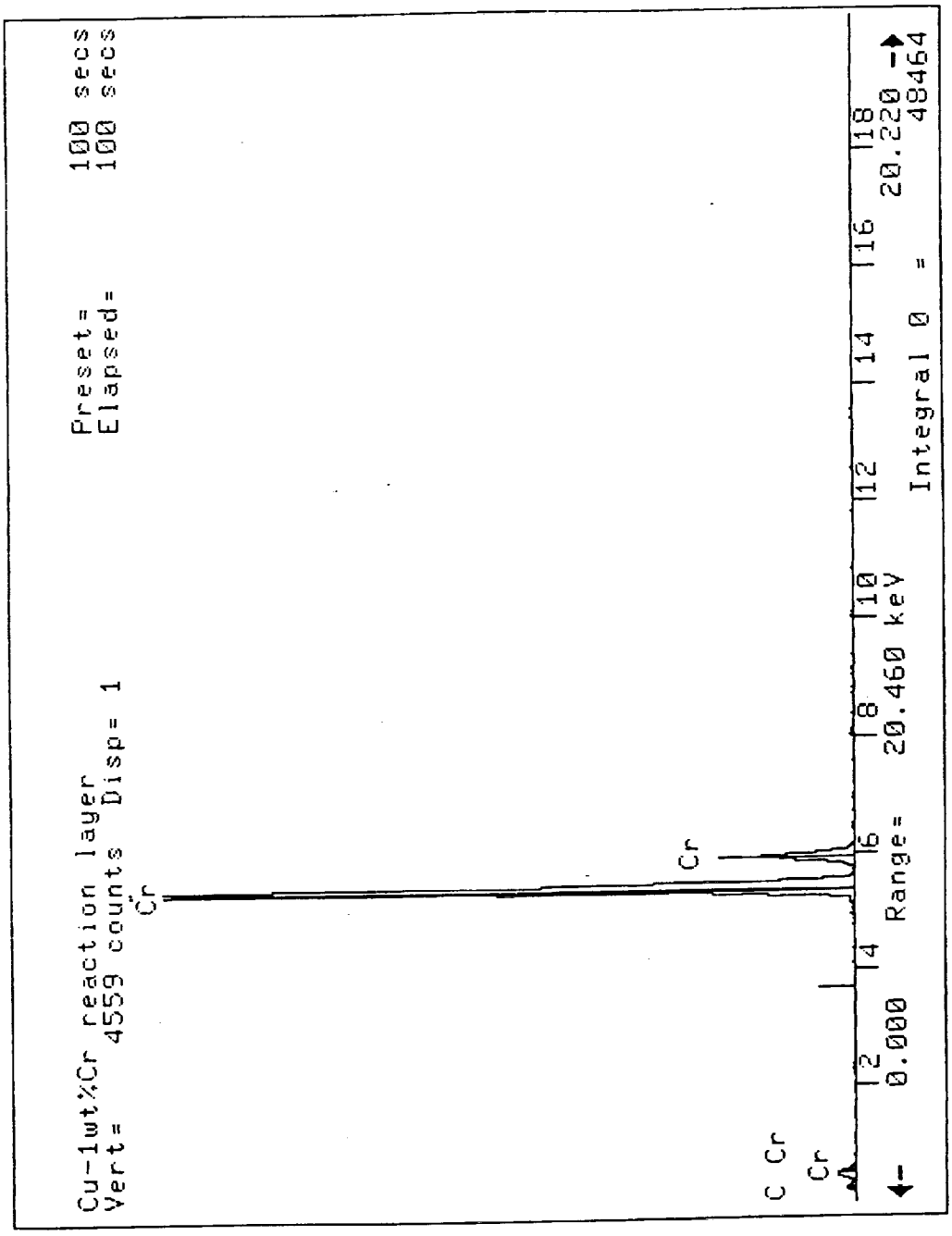

Figure 3.21. EDS spectrum of Cu-1.22at%Cr sessile drop specimen: reaction layer.

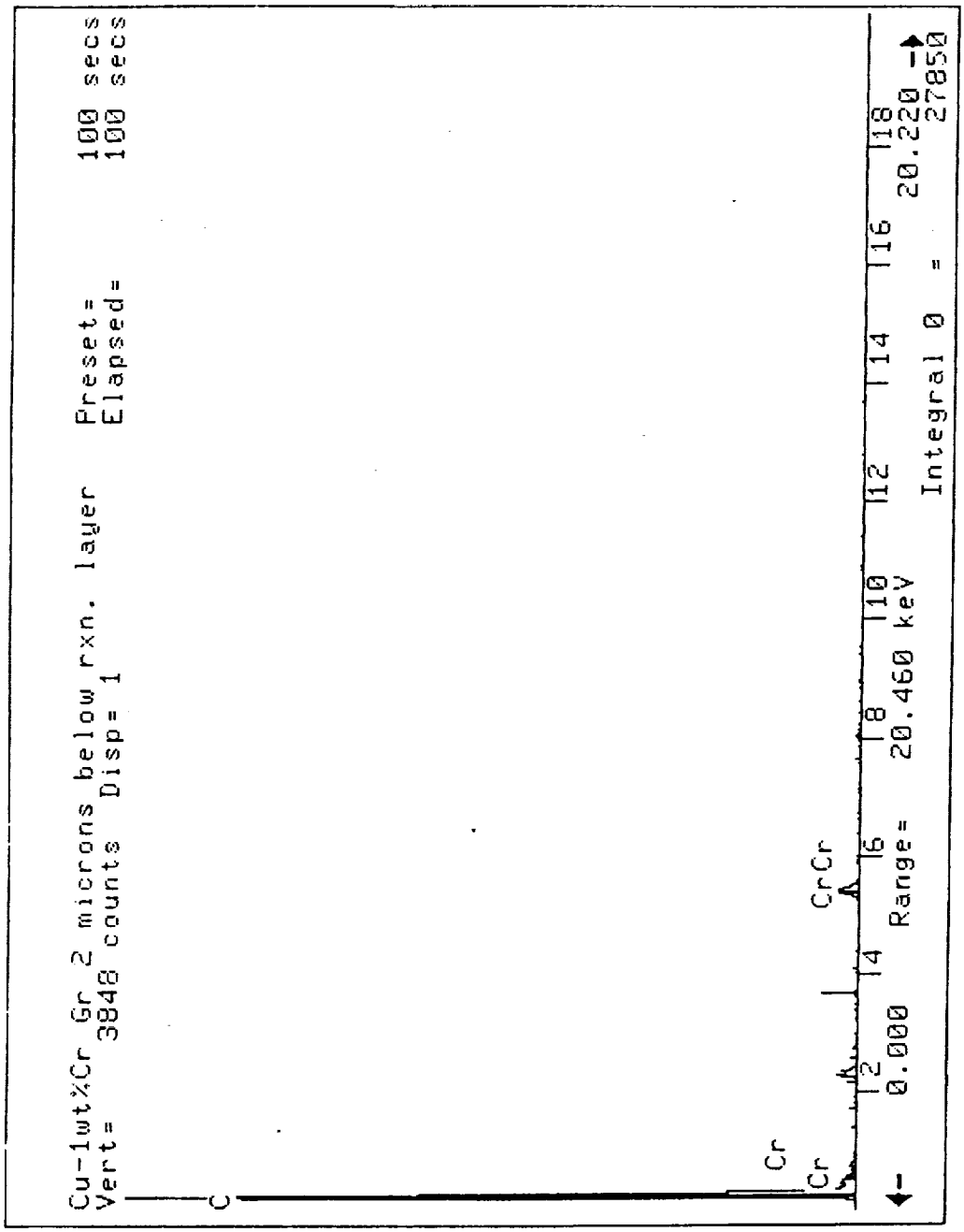

Figure 3.22. EDS spectrum of Cu-1.22at%Cr sessile drop specimen: Gr, 2 μm below reaction layer.

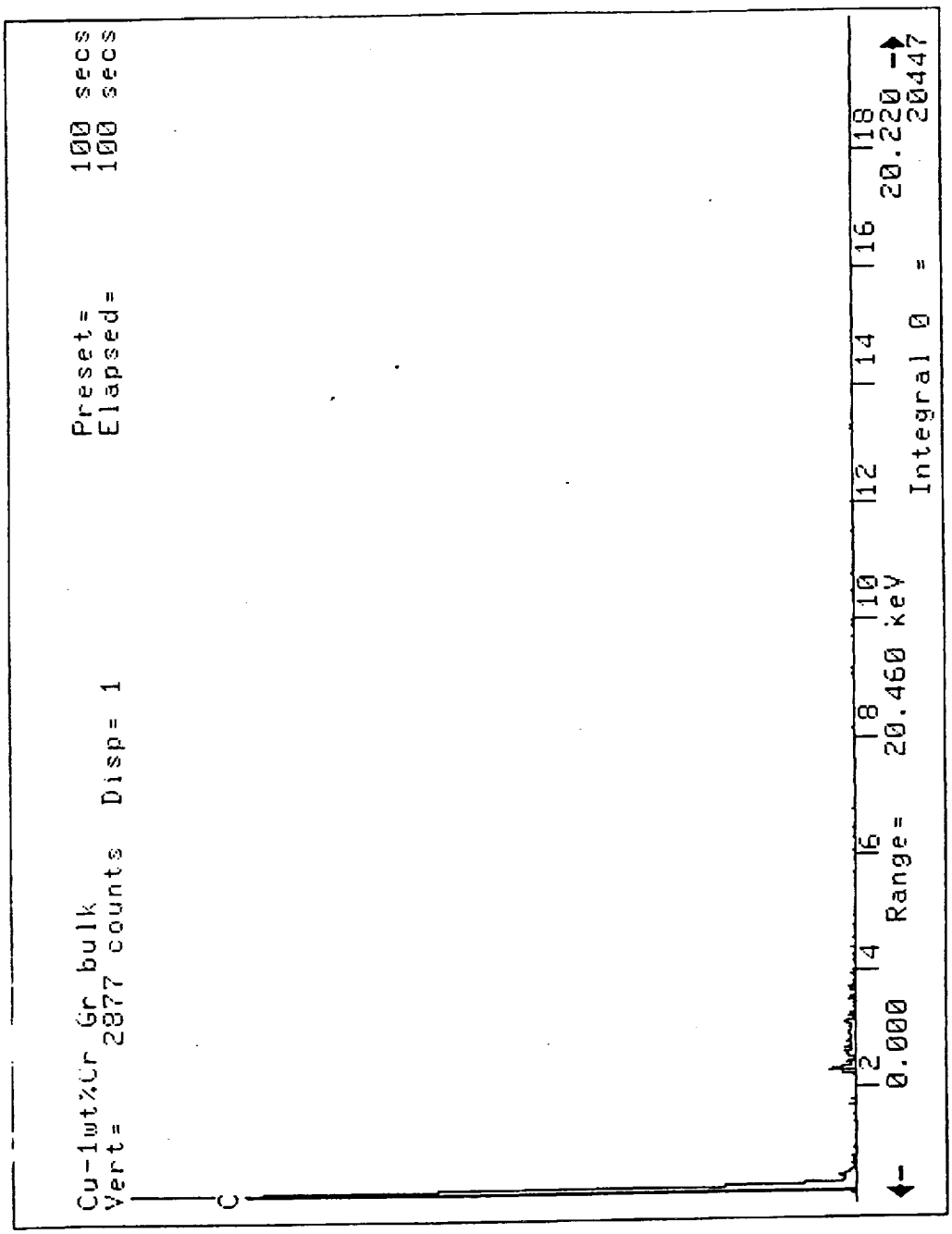

Figure 3.23. EDS spectrum of Cu-1.22at%Cr sessile drop specimen: Gr bulk.

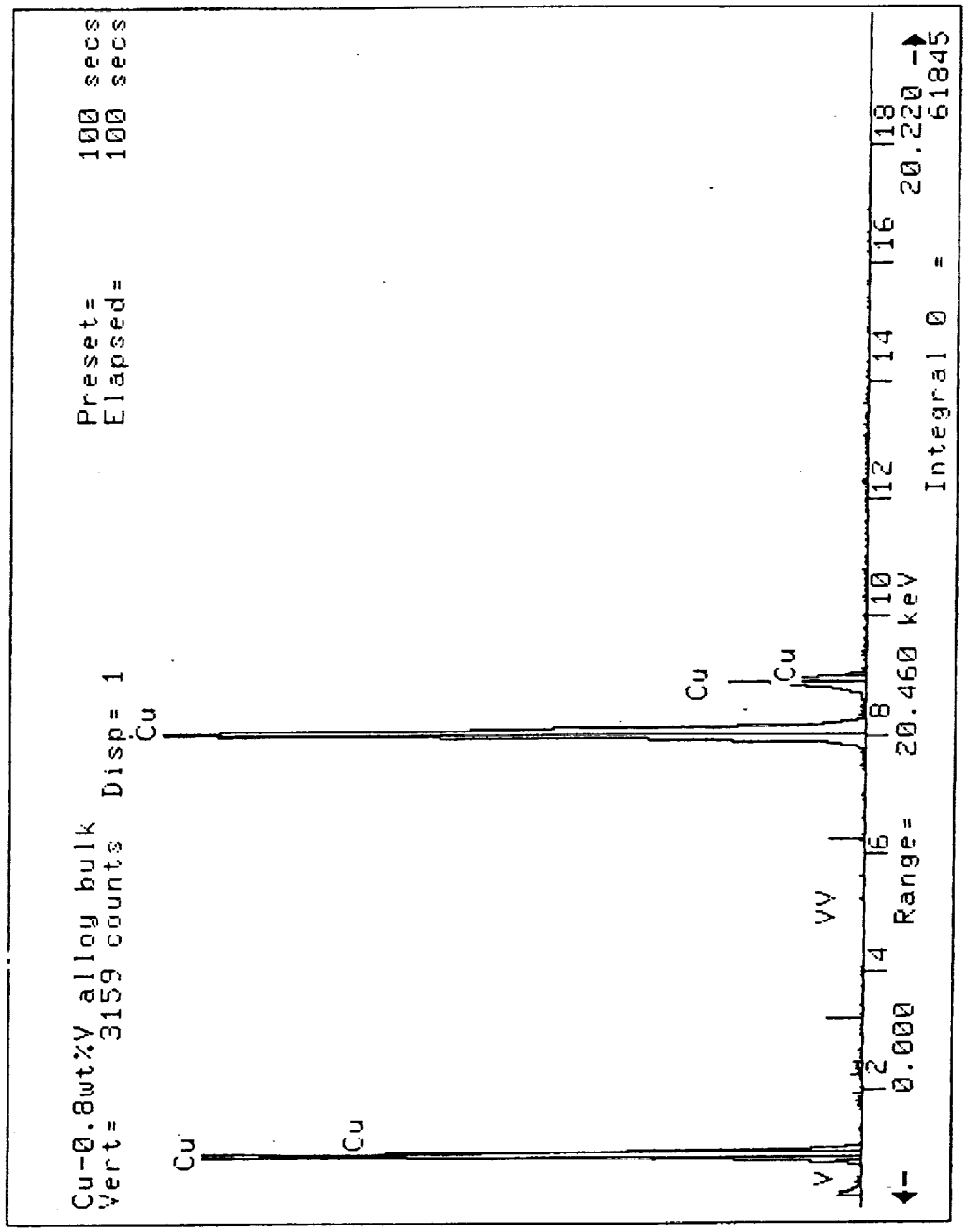

Figure 3.24. EDS spectrum of Cu-1.00at% V sessile drop specimen: bulk alloy.

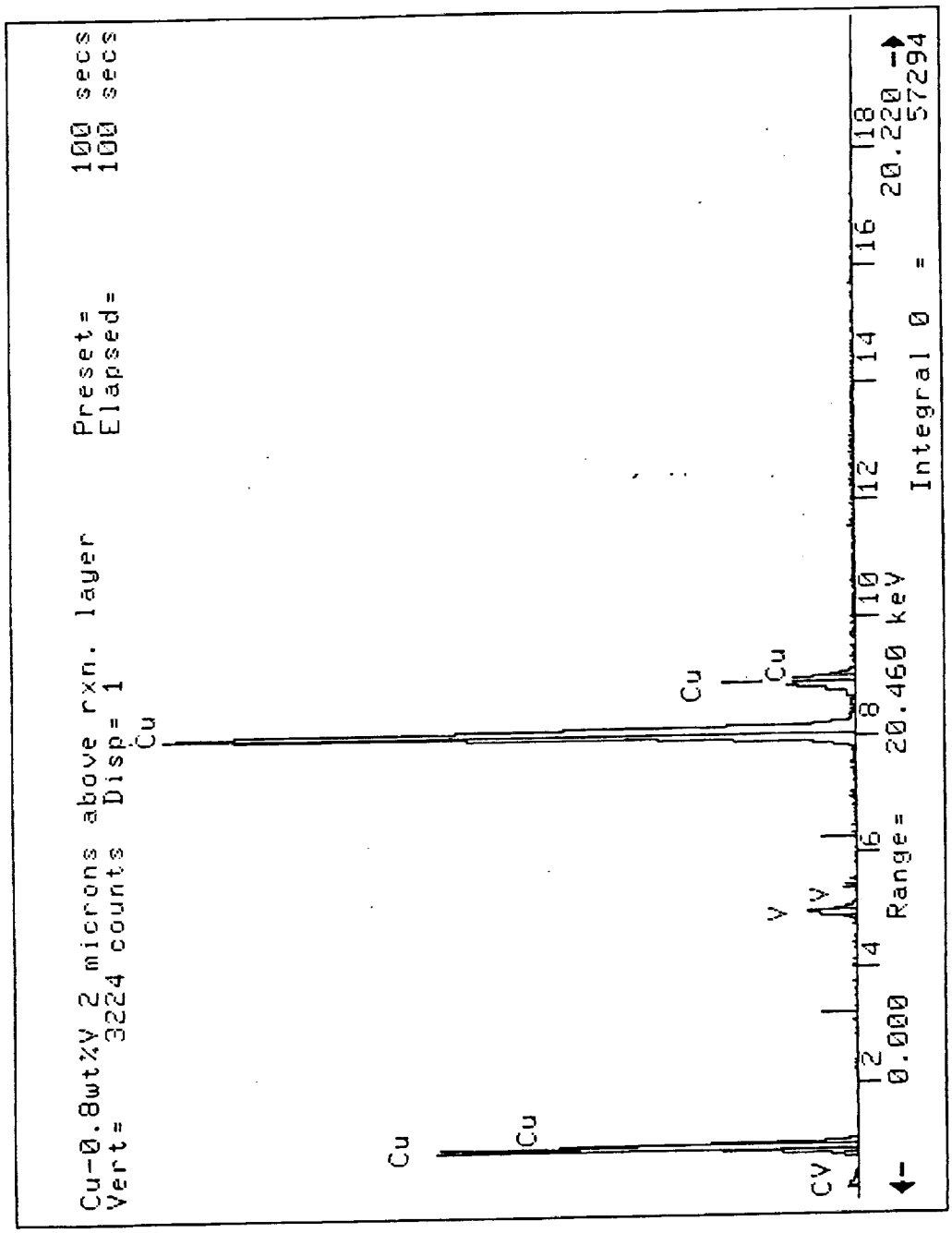

Figure 3.25. EDS spectrum of Cu-1.00at% V sessile drop specimen: alloy, 2 μm above reaction layer.

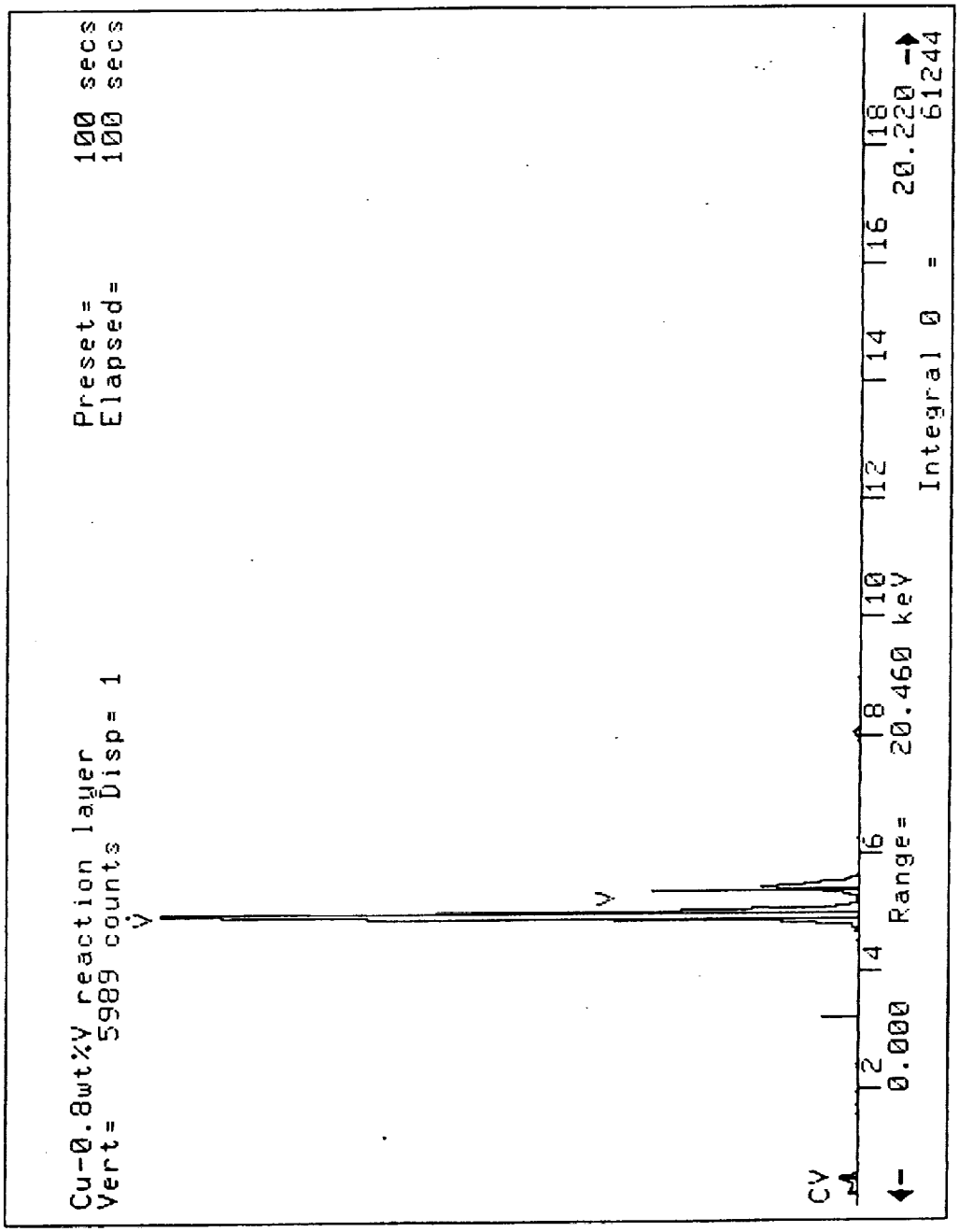

Figure 3.26. EDS spectrum of Cu-1.00at%V sessile drop specimen: reaction layer.

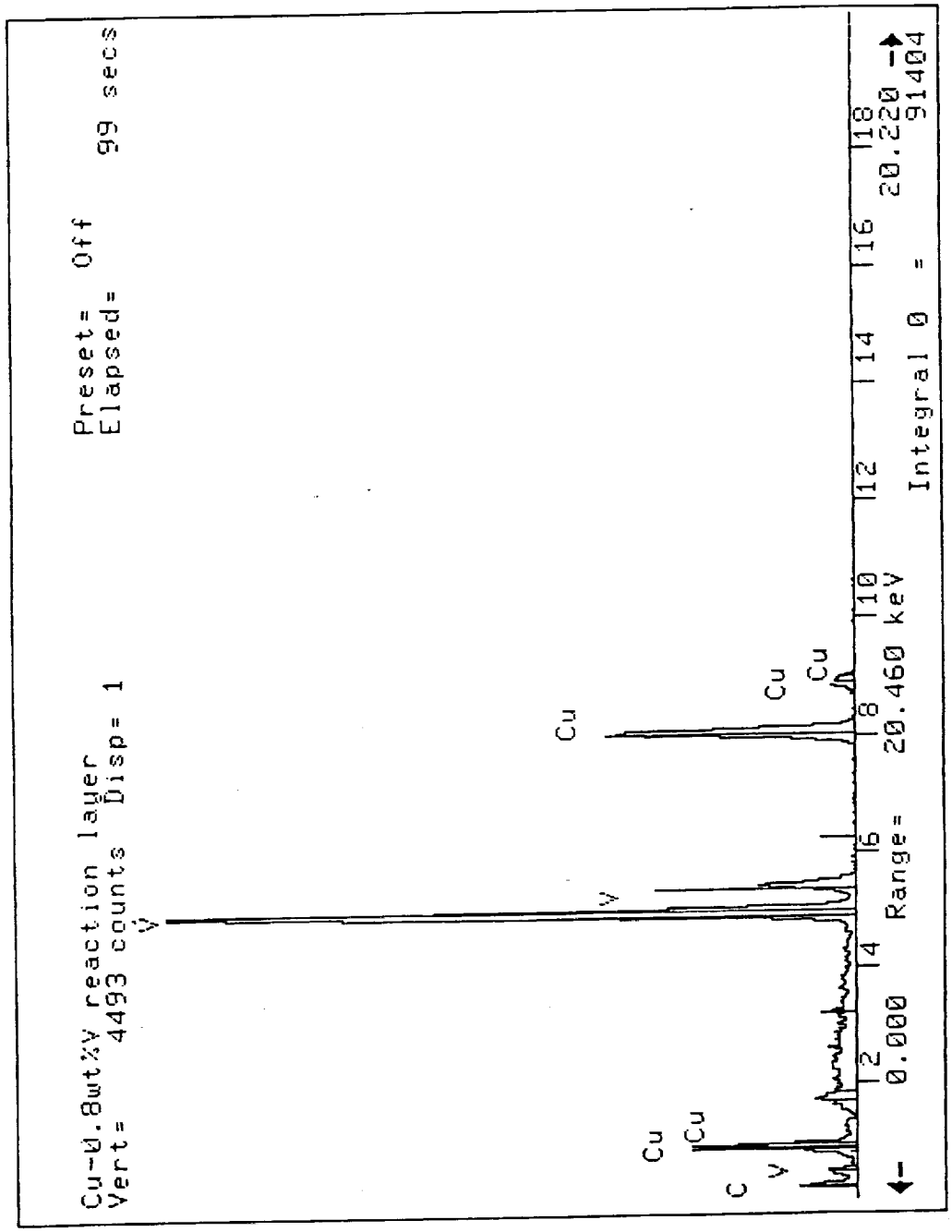

Figure 3.27. EDS spectrum of Cu-1.00at%V sessile drop specimen: interdendritic region of reaction layer.

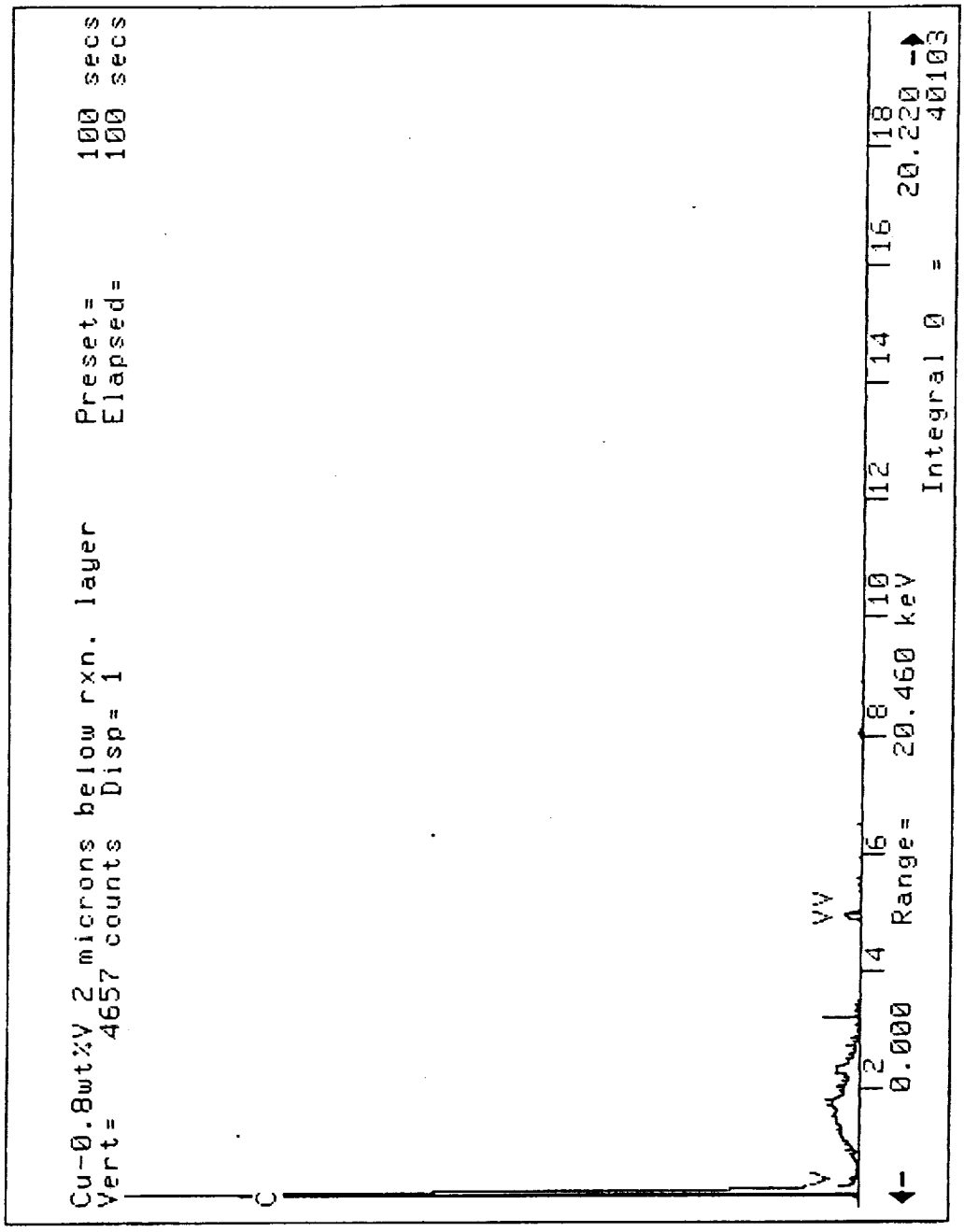

Figure 3.28. EDS spectrum of Cu-1.00at%V sessile drop specimen: Gr, 2 μm below reaction layer.

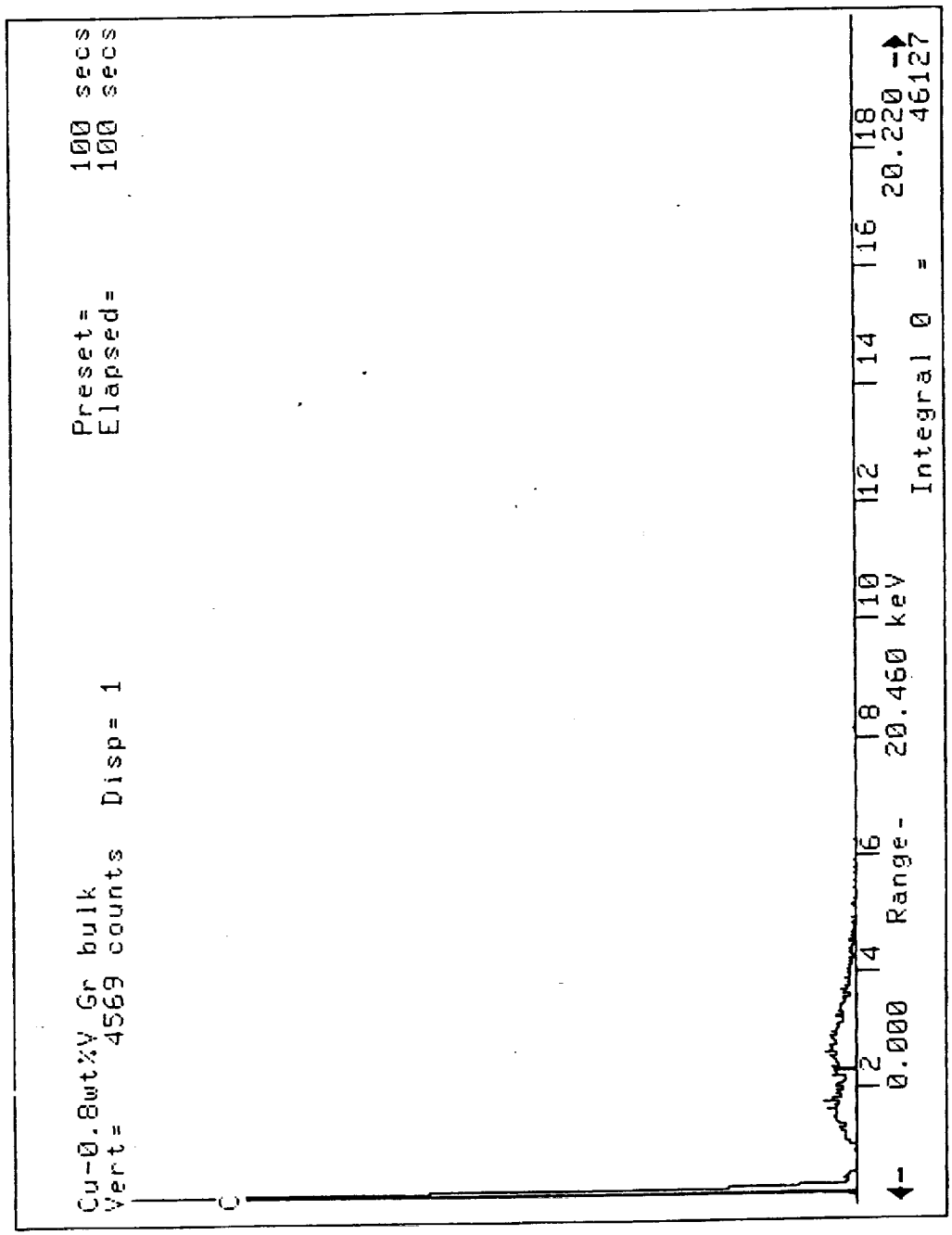

Figure 3.29. EDS spectrum of Cu-1.00at% V sessile drop specimen: Gr bulk.

reaction layer. Because the reaction layer formed at the Gr/Cu-V interface is columnar in nature, as depicted in Figure 3.10, the spectra taken in that area indicate the presence of Cu, V and C in some areas, and the presence of only V and C in others. These results indicate that the liquid Cu alloy was able to wet the intercolumnar regions in the V-rich reaction layer.

3.3.3 Auger Electron Spectroscopy

The information obtained using the SEM and EDS analyses were verified using Auger Electron Spectroscopy. After a 6 s sputter, line scans for Cu, Cr and C were obtained from the Cu-1.22at%Cr sessile drop test specimen. As indicated in the micrograph in Figure 3.30, the line scan was run over a length of approximately 60 μm. The scan begins in the Cu-Cr alloy and crosses the reaction layer into the Gr. The result of the line scan for Cu, shown in Figure 3.31, indicates a high concentration across the bulk alloy and a drop in concentration to an insignificant amount at the reaction layer and across the Gr. The same scan was obtained for Cr and is shown in Figure 3.32. As indicated earlier, in the EDS analysis, there is a great increase in the Cr concentration over the reaction layer. Ignoring the presence of adventitious C, Figure 3.33 shows an increase in C concentration across the reaction layer. Figure 3.34 is a survey scan taken on the reaction layer after a 60 s (1 min) sputter. The high concentration of Cr and the presence of C is in agreement with the results already given. The character of the C peak is similar to that expected of graphitic C.

3.4 X-Ray Diffraction

Because the chemical composition of the reaction layer could not be quantitatively determined via EDS or AES analyses, x-ray diffraction methods were employed. A preliminary x-ray spectrum of the reaction layer present on the Gr surface of the Cu-0.61at%Cr sessile drop test specimen (shown in Figure 3.6) was taken. This spectrum

is shown in Figure 3.35. The spectrum for the untested Gr surface is shown in Figure 3.36. Examination of the diffraction peak positions for C, Cr_3C_2, Cr_7C_3 and $Cr_{23}C_6$ indicate that the reaction layer phase is Cr_3C_2. These diffraction peak positions are included in Appendix II. A list of the Cr_3C_2 peak positions and the observed peak positions is given in Table 3.4. Only five Cr_3C_2 peaks are evident due to the discontinuous nature of the carbide layer investigated.

ORIGINAL PAGE
BLACK AND WHITE PHOTOGRAPH

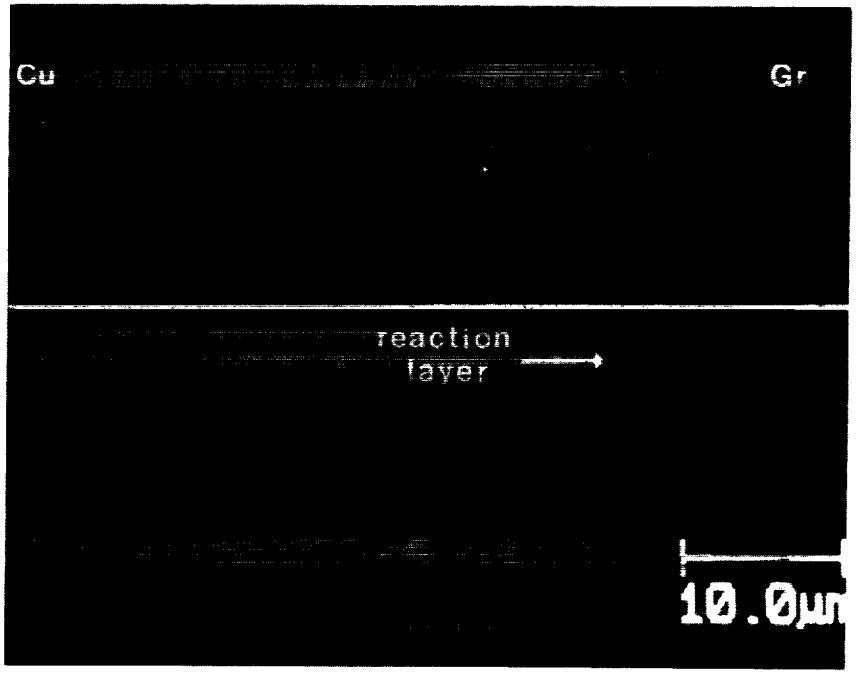

Figure 3.30. AES micrograph of Cu-1.22at%Cr sessile drop specimen indicating position of line scan analysis.

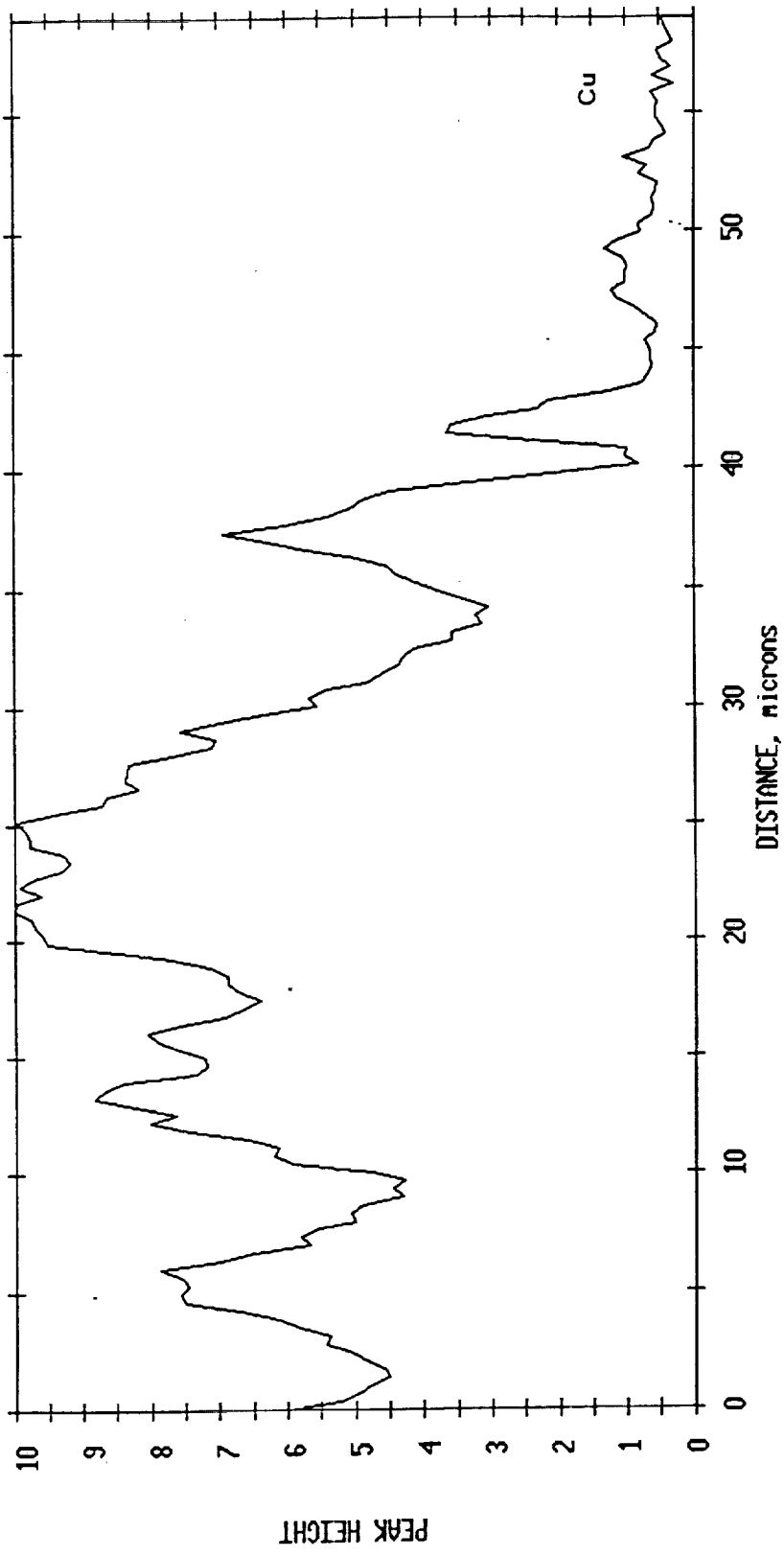

Figure 3.31. AES line scan for Cu over the interfacial region of a Cu-1.22at%Cr sessile drop specimen after 6 s sputter.

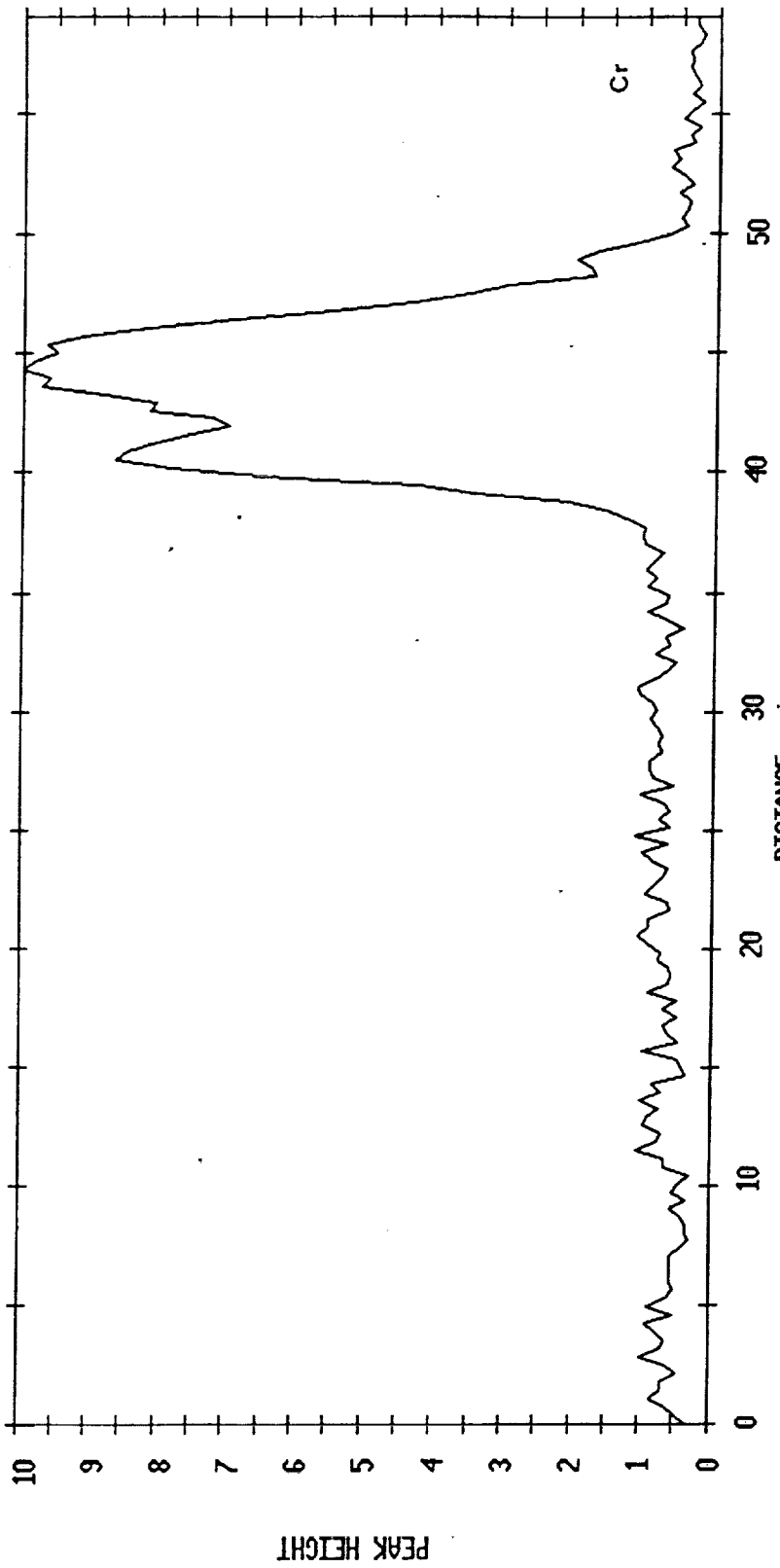

Figure 3.32. AES line scan for Cr over the interfacial region of a Cu-1.22at%Cr sessile drop specimen after 6 s sputter.

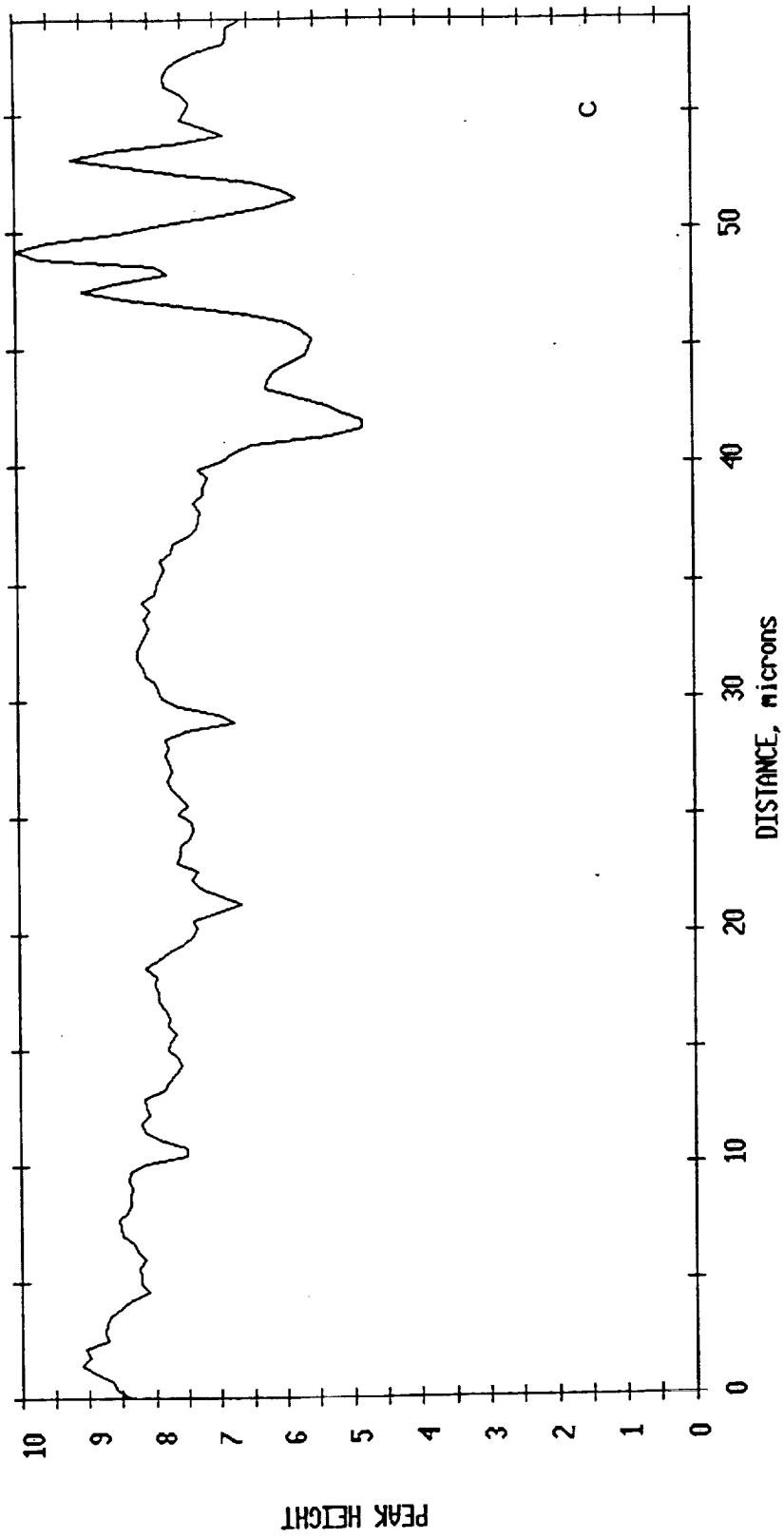

Figure 3.33. AES line scan of C over the interfacial region of a Cu-1.22at%Cr sessile drop specimen after 6 s sputter.

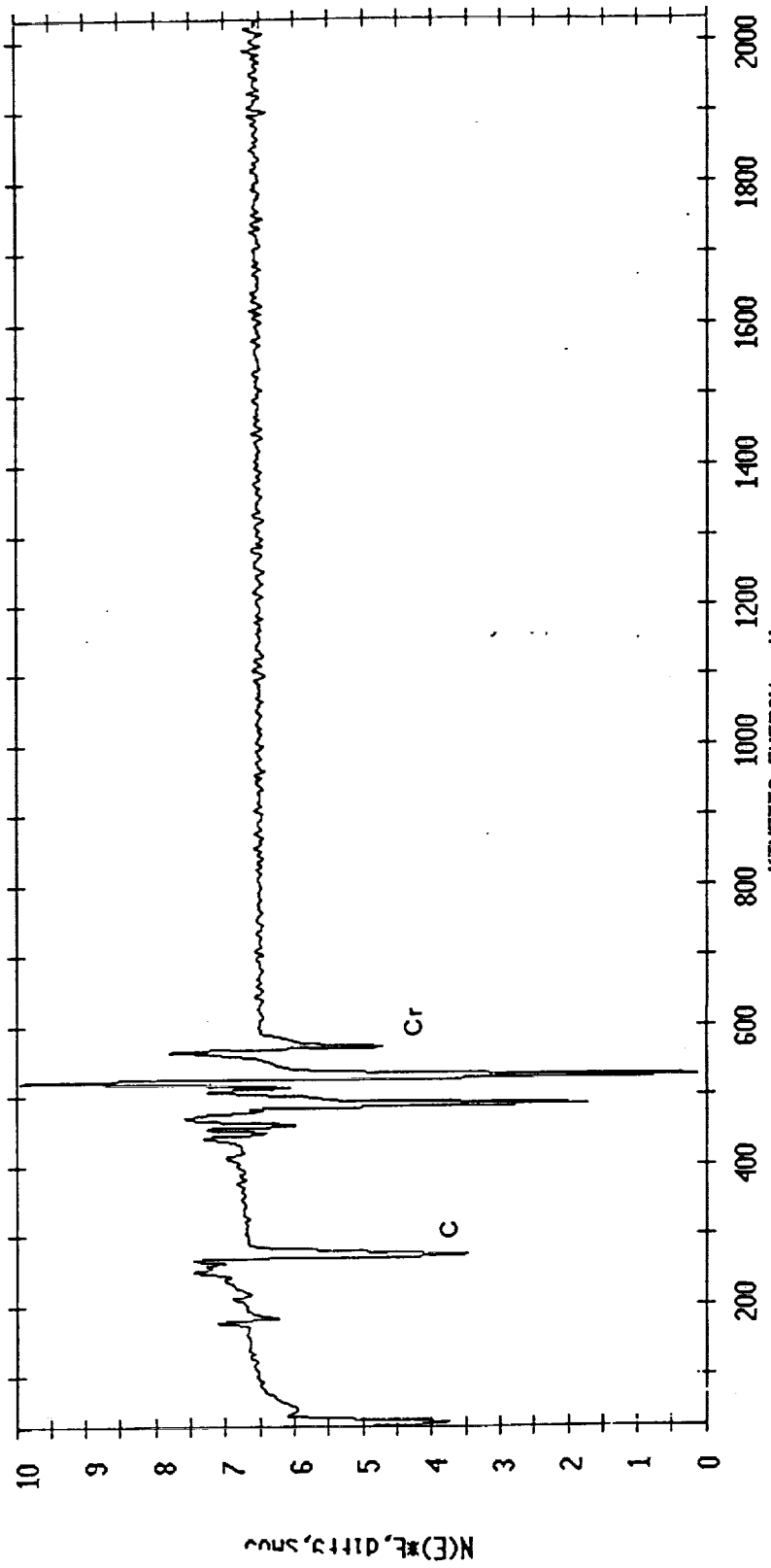

Figure 3.34. AES survey scan of reaction layer after 60 s (1 min) sputter.

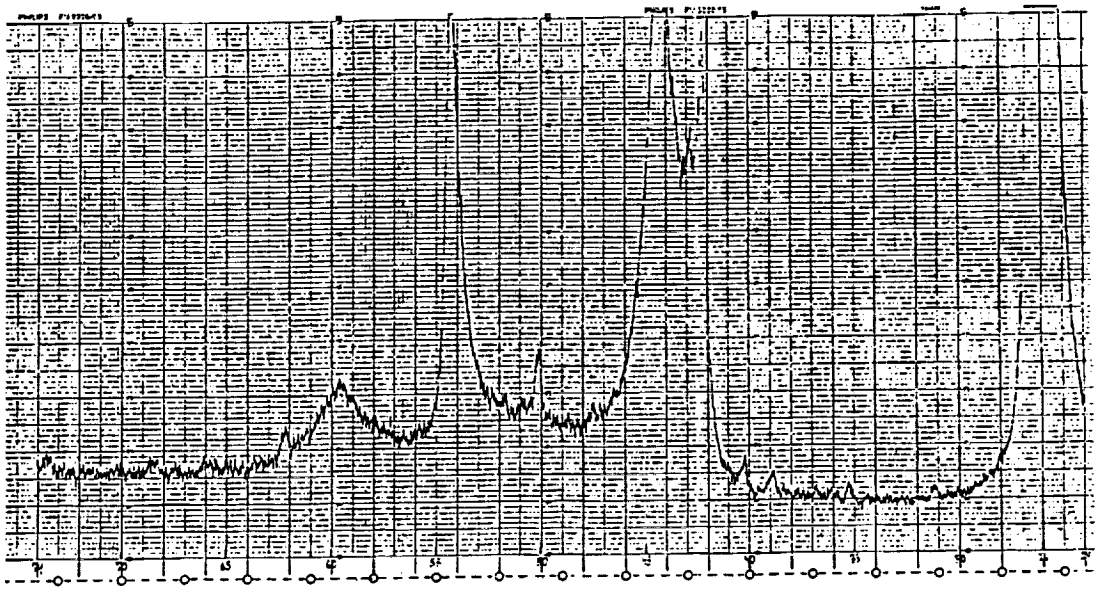

Figure 3.35. X-ray spectrum of reaction layer formed at Gr/Cu-0.61at%Cr interface.

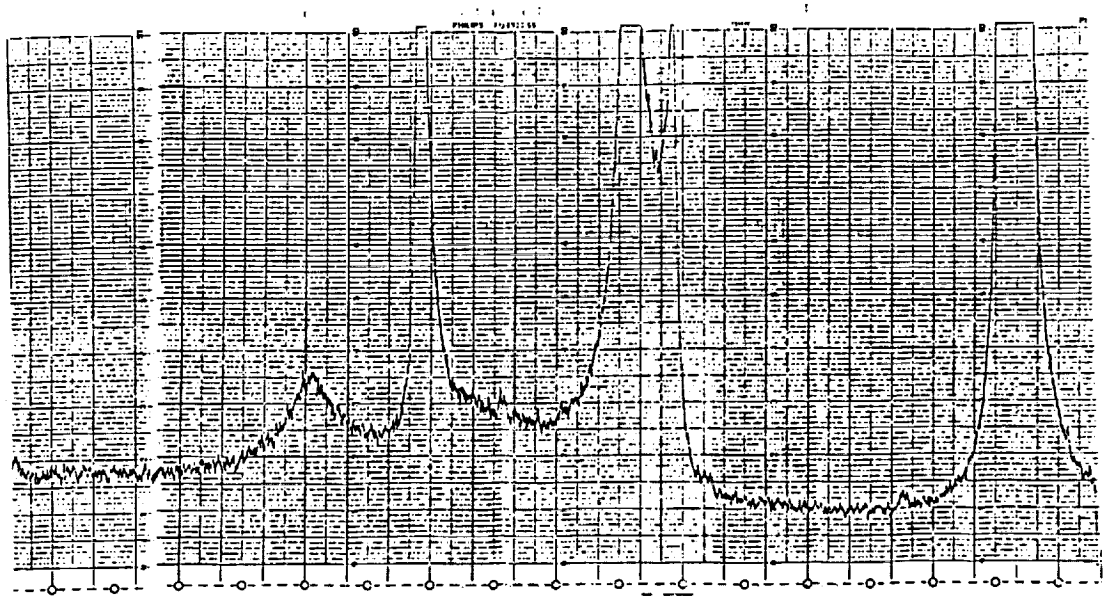

Figure 3.36. X-ray spectrum of untested Gr surface.

Table 3.4. Comparison of Cr_3C_2 and observed x-ray diffraction peaks.

peak position Cr_3C_2	peak position observed	peak position Cr_3C_2	peak position observed
4.978	n.o.	2.1215	
3.983	n.o.	2.1036	2.1141
3.146	n.o.	1.9912	n.o.
2.7460	n.o.	1.9482	n.o.
2.5478	2.5519	1.9151	n.o.
2.4897	n.o.	1.8934	n.o.
2.4596	n.o.	1.8691	n.o.
2.3063	2.3217	1.8190	1.8221
2.2751	n.o.	1.7833	n.o.
2.2409	2.2460	1.7670	n.o.

4 DISCUSSION

4.1 Contact Angle Measurements

The contact angle measurements given in Table 3.2 indicate that La is most effective in reducing the contact angle per at% added, followed by Ti and Zr. Other elements that reduced the contact angle significantly include Cr, Hf, V and Y. Cr and V, at the alloying levels of greater than 1 at%, were the only additions that resulted in wetting. All of the alloys melted within 50°C of the melting temperature of pure Cu. However, the V alloys required a temperature of 1530°C to achieve a completely liquid state. Although the Cu-V phase diagram does not indicate its presence, a miscibility gap was observed, upon melting at 1530°C, for all of the Cu-V alloys during the sessile drop tests. The two immiscible liquids were shown earlier in Figure 3.4.

The pooled standard deviation mentioned earlier is an average of the standard deviations of the data collected for each of the 26 alloys and represents the reproducibility of the tests. The value of 16° contains the error of angle measurement technique, as well as experimental factors. A high standard deviation was calculated for some of the Cu alloys. This is primarily due to the presence of a thin oxide coating which formed on some of the sessile drops. The formation of this film is dependent on its stability at the testing temperature and oxygen partial pressure in the system. Making the assumption that the alloying addition is dissolved in the Cu to approximately the solubility limit, the assumption that the activity of the alloying addition atoms equals unity can be made. The Ellingham diagram in Figure 4.1 indicates that formation of the oxides of the all of the alloying additions is possible under the testing conditions employed. However, oxide films were not observed on most of the samples while at the testing temperature.. The Cu-Cr alloy test specimens,

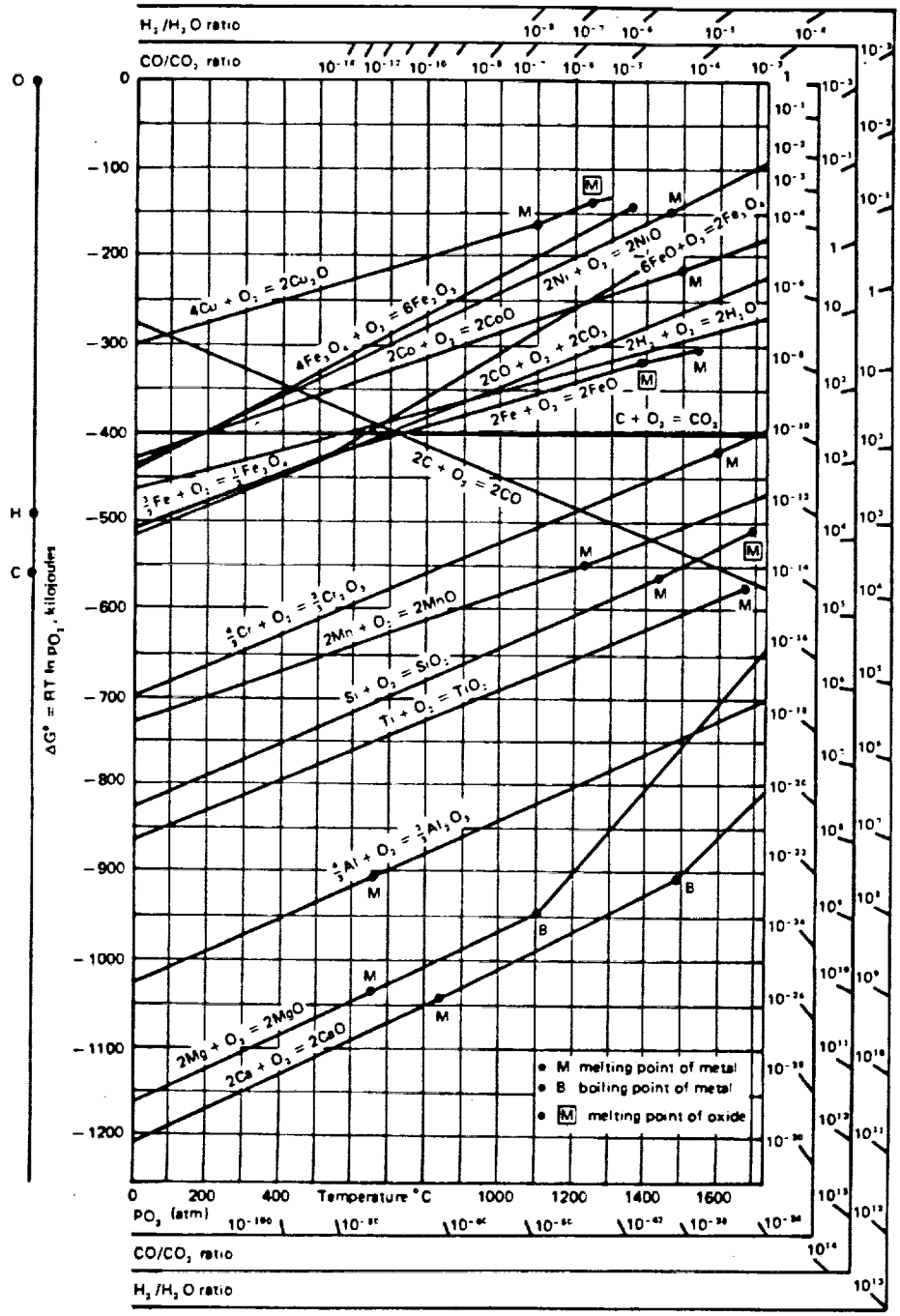

Figure 4.1. The Ellingham diagram for metallurgically important oxides. [Gaskell, 1981]

for example, did not indicate substantial, if any, oxide film formation. In many instances, upon cooling and exposure of the test specimen to air, oxide films developed.

In many cases, the angle measurements reported for the alloy compositions investigated are higher than those reported previously by others [Mortimer and Nicholas 1970, 1971; Nogi, Osugi and Kazumi, 1990]. The difference in angle measurements can be attributed to the difference in experimental methods. Although the testing temperatures were similar, Mortimer and Nicholas conducted their experiments in vacuum. The substrates used were HX30 Gr and vitreous carbon. Nogi, Osugi and Kazumi tested in an Ar-5H_2 atmosphere at 1500°C, using commercial grade Gr substrates. Because the carbon substrates used in each study are different, the measured contact angles for one type of substrate are different from those of another. The other experimental factor that affects wetting behavior, and therefore contact angle measurements, is the testing atmosphere. Tests conducted in vacuum and in atmospheres containing hydrogen, an oxygen getter, provide less chance of oxygen contamination or oxide film formation.

4.2 Interfacial Energy Calculations

The Gr/Cu interfacial energy was observed to be affected by alloying addition. The alloying elements most effective in lowering the Gr/Cu interfacial energy are La, Ti and Zr. The value calculated for pure Cu of 1975 mJ/m^2 is decreased to 1418 mJ/m^2 for an addition of only 0.054 at% Ti and to 1298 mJ/m^2 for 0.07 at% Zr. The Gr/Cu interfacial energy is also affected by the amount of alloying element present. As seen in Table 3.2, increasing at% of all the additions studied, with the exception of Ta, results in a greater decrease in interfacial energy.

The results of the calculations for the Gr/Cu interfacial energies shown in Table 3.2 indicate that, in some cases, such as with Cr and V, negative values can be obtained. These values are obviously incorrect. Three possible explanations exist for this discrepancy.

The first two possibilities concern the assumptions about the surface energies of the Cu and Gr. The surface energy of the Cu was assumed to be constant with respect to both alloying element and the amount of alloying element added. This assumption is probably not valid given the high mobility of the alloying elements in the liquid Cu and the tendency of many of the elements to segregate to interfaces. The presence of these alloying addition atoms at the Cu/vapor interface could decrease the surface energy to values considerably below the assumed value of 1279 mJ/m^2. The assumption that the surface energy of Gr is 798 mJ/m^2 may also not be correct. The surface energy of Gr has a wide range of values depending on grade, contamination level, degree of orientation, and the plane of the Gr exposed at the surface [Mortimer and Nicholas, 1970].

The third assumption is regarding which interfacial energy is actually being measured. No allowance was made for the presence of a reaction layer at the interface. To account for the reaction layer the surface energy of the reaction layer should be used instead of the surface energy of Gr [Nicholas and Mortimer, 1971; Loehman, 1989]. This in turn requires knowledge of the interfacial reaction products and their surface energies. While the reaction products can be determined experimentally, in most cases their surface energies are not known.

Mortimer and Nicholas [1970], however, have reported surface energy values for the carbides of six of the twelve alloys studied in this investigation. These values are given for temperatures of 1100-1150°C, a temperature range applicable to this

Table 4.1. Carbide/Cu-alloy interfacial energies.

Cu-alloy addition	at%	contact angle, °	carbide formed	$\gamma_{SV\,carbide}$ mJ/m^2	$\gamma_{carbide/Cu}$ mJ/m^2
Cr	0.49	140	Cr_3C_2	975	1954
	0.61	114			1495
	0.98	60			336
	1.10	45			71
	1.22	41			10
Hf	0.36	90	HfC	690	690
	0.72	80			468
Nb	0.14	140	NbC	2440	3420
Ti	0.054	128	TiC	1190	1977
	0.054	119			1810
V	0.37	128	VC	1675	2462
	1.00	45			771
Zr	0.07	113	ZrC	800	1300
	0.28	111			1258

study. Still assuming that the surface energies of the Cu alloys are equal to the surface energy of pure Cu, and using their values for the surface energies of the carbides, where possible, the interfacial energies have been recalculated. Table 4.1 contains the calculations for the carbide/Cu interfacial energies. The interfacial energy calculations are dependent on the surface energy of the alloy, the surface energy of the substrate and the contact angle. In the case of carbide formation, the alloying addition affects each of these three quantities. Table 4.1 contains calculations that have taken two of these into account and therefore contains more accurate values. The previously reported calculations, in Table 3.2, only consider one of the alloy-dependent quantities.

4.3 Reaction Layer Analysis

4.3.1 Continuity

The degree of wetting is shown to be affected by whether the carbide layer is continuous or discontinuous as discussed by Nogi, Osugi and Ogino [1990]. Analyses of the Cu-Cr alloy and Cu-V alloy interfaces, summarized in Table 3.2, confirm that the best wetting is obtained when a continuous reaction layer forms. It has also been noted that only when a continuous reaction layer is formed does the Cu alloy test specimen adhere to the Gr substrate.

4.3.2 Thickness

The thickness of the reaction layer is a function of the alloying level. A higher concentration of alloying addition results in a greater thickness of carbide layer, assuming the carbide layer forms at all. Obviously, more Cr is needed to form a 10 μm thick carbide layer, than a 0.2 or 1.3 μm thick layer. The same is true for the Cu-V alloys.

Mass balance calculations verify the feasibilty of forming a reaction layer of 10 μm thickness. The two following calculations determine the volume of the Cu-1.22at%Cr sessile drop test specimen and volume of a reaction layer of 10 μm thickness that extends 1 mm beyond the sessile drop edge radially.

volume of Cu-Cr sample: $r = 9.525$ mm
$t = 2.0$ mm
$V = 570\ mm^3$

volume of reaction layer: assume spreading of 1 mm in radial direction
$r = 10.5$ mm
$t = 0.01$ mm
$V = 3.46\ mm^3$

The available volume of Cr in the sample can be shown to be twice that which is needed to form the reaction layer by the following:

available volume of Cr: $\rho\ (Cu) = 8.93\ g/cm^3$
$\rho\ (Cr) = 7.2\ g/cm^3$

$$\frac{8.93\ g\ Cu}{1000\ mm^3} = \frac{x}{570\ mm^3} \quad \text{-------> } x = 5.09\ g\ Cu$$

$$\text{-------> } 0.0509\ g\ Cr$$

$$\frac{7.2\ g\ Cr}{1000\ mm^3} = \frac{0.0509\ g\ Cr}{V} \quad \text{-------> } V = 7.07\ mm^3\ Cr$$

This indicates that if the composition of the reaction layer was simply elemental Cr, there is a sufficient concentration available in the sample. However, it has been shown that the composition of the reaction layer is Cr_3C_2. The volume of Cr_3C_2 that can form has also been caculated.

available volume of Cr_3C_2: $\rho = 6.68\ g/cm^3$

moles Cr_3C_2 ---> 0.0509 g Cr = 0.000979 moles Cr
---> 0.000326 moles Cr_3C_2

(0.000326 moles Cr_3C_2)(180 g/mole) = 0.05868 g Cr_3C_2

$$\frac{6.68\ g\ Cr_3C_2}{1000\ mm^3} = \frac{0.0509\ g\ Cr}{V} \quad \text{-------> } V = 8.784\ mm^3\ Cr_3C_2$$

This, again, is considerably higher than the volume of the reaction layer. Based on a mass balance analysis, it is quite possible for a carbide layer of such dimensions to form.

4.3.3 Composition

As indicated by the x-ray diffraction spectrum, the reaction layer phase that forms at the Gr/Cu-Cr alloy interface is Cr_3C_2. This agrees with thermodynamic considerations of the reaction layer composition. The Cr-carbide phase diagram, shown in Figure 1.15, indicates that Cr_3C_2 is the most likely phase to form given the small amount of Cr compared to the C available from the Gr substrate. From the Cu-Cr phase diagram (Figure 1.13), at 1130°C, the Cr liquid-solid transition occurs at X_{Cr} = 0.02, a composition of 2 at%. Assuming Henrian behavior, the activity of Cr in liquid Cu can be calculated as follows:

$$a_{Cr} = \gamma_{Cr} X_{Cr}$$
$$\gamma_{Cr} = a_{Cr}/X_{Cr} = 1/0.02 = 50 \text{ (constant at T = 1403K)}$$
$$a_{Cr} = (50)(0.0122) = 0.61 \text{ in liquid Cr}$$

Assuming the activity of C is 1, and the activities of the potential carbide phases are also 1, the free energy of formation for each carbide phase can be determined.

$$3Cr + 2C = Cr_3C_2$$

$$\Delta G = \Delta G^\circ + RT\ln k$$
$$k = a_{Cr_3C_2}/a_{Cr}^3 a_C^2 = 1/a_{Cr}^3 = 1/(0.61)^3 = 4.4$$
$$\Delta G^\circ = -27100 \text{ cal/mole [Elliot and Gleiser, 1960]}$$
$$\Delta G = -27100 \text{ cal/mole} + (1.987 \text{ cal/}^\circ \text{ mole})(1403K)\ln(4.4)$$
$$\Delta G = -22970 \text{ cal/mole}$$
$$\Delta G = -4594 \text{ cal/g-atom}$$

$7Cr + 3C = Cr_7C_3$

$\Delta G = \Delta G° + RT\ln k$
$k = a_{Cr_7C_3}/a_{Cr}^7 a_C^3 = 1/a_{Cr}^7 = 1/(0.61)^7 = 31.8$
$\Delta G° = -50300$ cal/mole [Elliot and Gleiser, 1960]
$\Delta G = -50300$ cal/mole + (1.987 cal/° mole)(1403K)ln(31.8)
$\Delta G = -40654$ cal/mole
$\Delta G = -4065$ cal/g-atom

$23Cr + 6C = Cr_{23}C_6$

$\Delta G = \Delta G° + RT\ln k$
$k = a_{Cr_{23}C_6}/a_{Cr}^{23} a_C^6 = 1/a_{Cr}^{23} = 1/(0.61)^{23} = 86579.2$
$\Delta G° = -111200$ cal/mole [Elliot and Gleiser, 1960]
$\Delta G = -111200$ cal/mole + (1.987 cal/° mole)(1403K)ln(86579.2)
$\Delta G = -79506$ cal/mole
$\Delta G = -2741$ cal/g-atom

The free energies of formation for each of the Cr_3C_2, Cr_7C_3 and $Cr_{23}C_6$ carbides indicate that the Cr_3C_2 phase is the most stable of the three.

The critical amount necessary to start the reaction $3Cr + 2C = Cr_3C_2$ is checked by the following calculation:

assume: $\Delta G = 0$ --> no driving force
$\Delta G = \Delta G° + RT\ln(1/a_{Cr}^3)$
$\exp(-\Delta G°/RT) = 1/a_{Cr}^3 = 16665$
$a_{Cr} = 0.039$
$X_{Cr} = a_{Cr}/\gamma_{Cr} = (0.039)(50) = 0.00078$ ---> 0.078 at% Cr

There is enough Cr in each of the Cu-Cr alloy test specimens to start the reaction for the formation of Cr_3C_2.

4.4 Carbide Formation

The formation of the Cr_3C_2 reaction layer phase can be described in terms of diffusion mechanisms and calculations. The following calculation indicates that, under the testing conditions employed, Cr can diffuse in liquid Cu a distance of 1 mm:

$t = 3600$ s, $D = 3 \times 10^{-6}$ cm^2/s [Shurygin and Shantarin, 1968]

$$x = (Dt)^{1/2}$$
$$x = [(3600)(0.3 \times 10^{-5})]^{1/2}$$
$$x = 1 \text{ mm}$$

This distance is equal to half of the height of the Cu alloy sessile drop test specimen.

Once the Cr has diffused to the Gr/Cu-Cr interface, nucleation of the carbide phase occurs across the length of the interface. The reaction layer can grow in the z direction via bulk diffusion of the C and Cr through the carbide. It can extend or grow outward, in the r direction by surface diffusion of the Cr along the Gr surface. Carbide layer formation is limited by the bulk diffusion of C in the carbide [Fries, Cummings, Hoffman and Daily, 1967]. Surface diffusion can be many orders of magnitude faster than bulk diffusion, as was shown in Section 1.5.

Given the activation energy for C in Cr_3C_2 [Fries, Cummings, Hoffman and Daily, 1967], the bulk diffusion of C through Cr_3C_2 can be estimated as follows:

$Q = 45$ kcal/mole
$\exp[-Q/RT] = \exp[-45000/(1.987)(1403)] = 9.7 \times 10^{-8}$

from growth,

$D = x^2/t = (10\ \mu m)^2/3600\ s = 2.8 \times 10^{-10}$ cm^2/s
$D_o = D/\exp[-Q/RT] = (2.8 \times 10^{-10}\ cm^2/s)/(9.7 \times 10^{-8}) = 0.0029$ cm^2/s

The bulk diffusion of Cr through Cr_3C_2 can be approximated to the same order of magnitude based upon the observation, from SEM micrographs, that the reaction layer extends upward into the alloy specimen and downward into the Gr substrate about the same distance.

The diffusion rate for Cr along Cr_3C_2, via surface diffusion, is much faster. Assuming that the surface diffusion of C is of the same order of magnitude as the surface diffusion of Cr, the following calculations can be made:

$D_{surface} = D_{bulk}$(surface/bulk diffusion ratio given in Section 1.5)
$D_{surface} = 2.8 \times 10^{-10}$ cm^2/s (1.1×10^8)
$D_{surface} = 0.03$ cm^2/s

The distance that the carbide layer can grow radially in one hour, via surface diffusion, is:

$t = 3600$ s, $D = 0.03$ cm^2/s

$x = (Dt)^{1/2}$
$x = [(3600)(0.03)]^{1/2}$
$x = 10.4$ cm

This indicates that surface diffusion is fast enough to extend the reaction layer far beyond the length of the sample. Assuming that the estimate of the surface diffusion rate of Cr in Cr_3C_2 is fair, and substituting 100 μm for the diffusion distance, x, an approximation of the time necessary to form the carbide layer observed for the Cu-Cr alloy test specimens (10 μm thick, extending 100 μm radially) can be made:

$x = (Dt)^{1/2}$
$t = x^2/D$
$t = (0.01)^2/0.03$
$t = 0.003$ s

Clearly, these initial calculations show that surface diffusion offers fast enough kinetic activity to produce the Cr_3C_2 layers in the size scale and time scale employed in this study. Actually, the use of a surface to bulk diffusion rate ratio of 10^8 is not necessary. A ratio of 10^4 would account for the observed growth of the carbide layer.

5 CONCLUSIONS

Sessile drop tests have been conducted on twelve Cu-based alloys to determine if the wetting of Gr by liquid Cu can be improved through alloying additions. Of the alloys studied, Fe, La, Mn, Nb, Si , Ta and Ti did not wet H-490 Gr at the alloying levels examined. The additions of Hf, Y and Zr decreased the wetting angles, but did not reduce the angles to much below 111° at the alloying levels investigated. The additions of Cr and V at approximately the level of 1 at% were able to enhance the wetting behavior such that wetting angles of 45°, or less, were produced. However, because of the difficulties of dissolving V in liquid Cu, a temperature of 1530°C was needed to achieve that degree of wetting. This renders the Cu-V alloy systems impractical for fabrication processes.

The Gr/Cu interfacial energy is affected by alloying additions that change the contact angle of the system. The addition of greater than 1 at% Cr results in a Cr_3C_2/Cu interfacial energy as low as 10 mJ/m^2. Although additions of about 1 at% of either Cr and V lower the contact angle to 45°, Cr is more effective in lowering the interfacial energy of the system.

Utilizing diffusion mechanisms and calculations, the formation of the reaction layers can be described. The formation of a reaction layer begins by surface nucleation which is made possible by the diffusion of an alloying element to the Gr/Cu alloy interface. This phase then grows by bulk diffusion of C and the alloying atoms through the reaction layer in the vertical direction, and by surface diffusion of the alloying atoms along the reaction layer in the radial direction. Due to the high mobility of the alloying addition atoms along the reaction layer, it extends outward much faster than it grows via bulk diffusion.

Auger electron spectroscopy and x-ray diffraction analyses indicate that the Gr/Cu-Cr alloy reaction layer is Cr_3C_2. This determination is supported by thermodynamic calculations. Upon formation of the reaction layer carbide, the Cu wets this layer and reduces not only its contact angle with the layer, but also the interfacial energy of the system.

The adherence of the reaction layer is a function of its continuity. Only in the cases of wetting, greater than 1 at% of Cr or V, did the Cu alloy form a continuous reaction layer, and therefore adhere to the Gr substrate.

LITERATURE CITED

Adamson, A.W. 1990. Physical Chemistry of Surfaces. Wiley and Sons, Inc., New York: 385-89.

Ash, B. and S. Fowser. Personal communications.

Bangham, D.H. and R.L. Razouk. 1937. Adsorption and the Wettability of Solid Surfaces. Trans. Faraday Soc. **33**: 1459.

Chakrabarti, D.J. and D.E. Laughlin. 1981. Bull. Alloy Phase Diagrams. **2** [3].

Chakrabarti, D.J. and D.E. Laughlin. 1982. Bull. Alloy Phase Diagrams. **2** [4].

Chakrabarti, D.J. and D.E. Laughlin. 1984. Bull. Alloy Phase Diagrams. **5** [1].

Dupre, A. 1869. Theorie Mechanique de la Chaleur. Paris: 368.

Elliot, J.F. and M. Gleiser. 1960. Thermochemistry for Steelmaking. Addison-Wesley Publ. Co., Reading, MA: 135-36.

Fries, R.J., Cummings, J.E., Hoffman, C.G. and S.A. Daily. 1967. Chemical Diffusion of C in the group VI-B metal carbides. US At. Energy Comm. Report: LA-3795.

Gaskell, D.R. 1981. Introduction to Metallurgical Thermodynamics. McGraw-Hill, New York: 287.

Kingery, W.D. 1959. Property Measurements at High Temperatures. Wiley and Sons, Inc., New York: 368.

Kingery, W.D. 1981. Introduction to Ceramics. Wiley and Sons, Inc., New York: 217-64.

Kishkoparov, N., Chentsov, V., Frishberg, I. and V. Pastukhov. 1984. Wetting of Natural Graphite by Copper Alloys. Sov. P. Met. and Met. Cer. [11]: 869-70.

Loehman, R. 1989. Interfacial Reactions in Ceramic-Metal Systems. Am. Ceram. Soc. Bull. **68** [4]: 891-92.

Massalski, T.B.,ed. 1986. Binary Alloy Phase Diagrams. Vol. 1. American Society for Metals, Metals Park, Ohio: 558, 559, 598, 916, 923, 934, 961, 971, 976, 982.

McDanels, D.L. and J.O. Diaz. 1989. Exploratory Feasibility Studies of Graphite Fiber Reinforced Copper Matrix Composites for Space Power Radiator Panels. NASA TM-102328.

Mortimer, D. and M. Nicholas. 1970. The Wetting of Carbon by Copper and Copper Alloys. J. Mat. Sci. **5** [2]: 149-55.

Murr, L. 1974. Interfacial Phenomena in Metals and Alloys. Addison-Wesley Publ. Co., Reading, MA: 102.

Nicholas, M. and D. Mortimer. 1971. The Wetting of Carbon by Liquid Metals and Alloys. Proc. of Int. Conf. on Carbon Fibers, their Composites and Applications, London, February 2-4: 1-3.

Nogi, K., Osugi, Y. and K. Ogino. 1990. A New Method of Wettability Measurement Utilizing a Small Sample and Its Application to Graphite or a-SiC and Liquid Cu-Cr Alloy Systems. ISIJ. **30** [1]: 64-9.

Pawlek, F. and K. Reichel. 1956. Der Einfluss von Beimengungen auf die elektrische Leitfahigkeit von Kupfer. Z. Metallkunde. **47**: 347.

Shurygin, P.M. and V.D. Shantarin. 1968. Compensation effects in the diffusion of metals in molten copper. Zhur. Fiz. Khim. **42** [2]: 463-65.

Storms, E.K. 1967. The Refractory Carbides. Academic Press, New York, NY: 47-60, 102-121.

Titran, R.H., McDanels, D.L. and T.L. Grobstein. 1989. Metal Matrix Composites for Space Power Applications. NASA TM-102114.

Weitzer, F., Remschnig, K., Schuster, J.C. and P.Rogl. 1990. Phase Equilibria and Structural Chemistry in the Ternary Systems M-Si-N and M-B-N. J. Mat. Research. **5** [10]: 2152-59.

Young, T. 1805. Miscillaneous Works. Vol. 1. G. Peacock, ed., Murray, London: 418.

Appendix I

The binary phase diagrams for Cu-Fe, Hf, La, Mn, Nb, Si, Ta, Ti, Y and Zr are given in Figures AI-1 through AI-10.

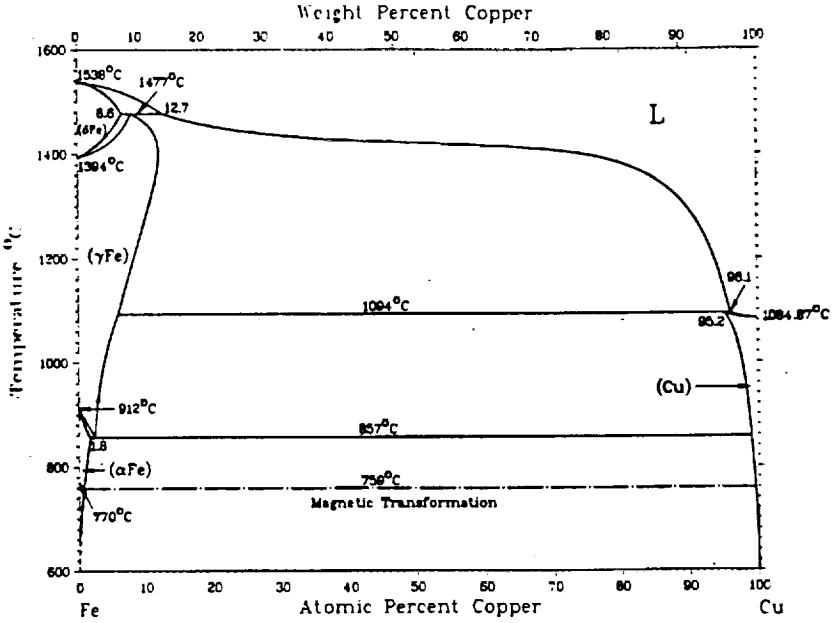

Figure AI-1. Fe-Cu phase diagram. [Binary Alloy Phase Diagrams, 1986, redrawn from Kubaschewski]

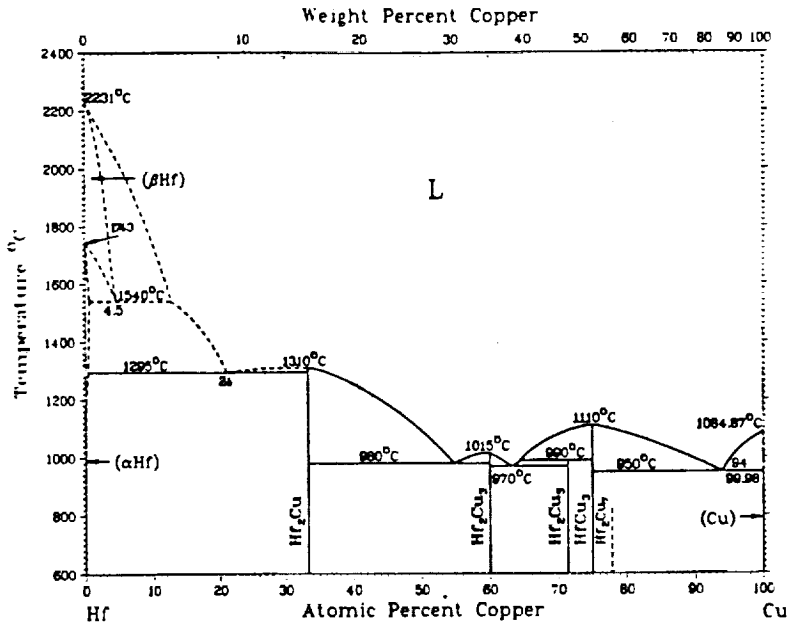

Figure AI-2. Hf-Cu phase diagram. [Binary Alloy Phase Diagrams, 1986, redrawn from Hafnium]

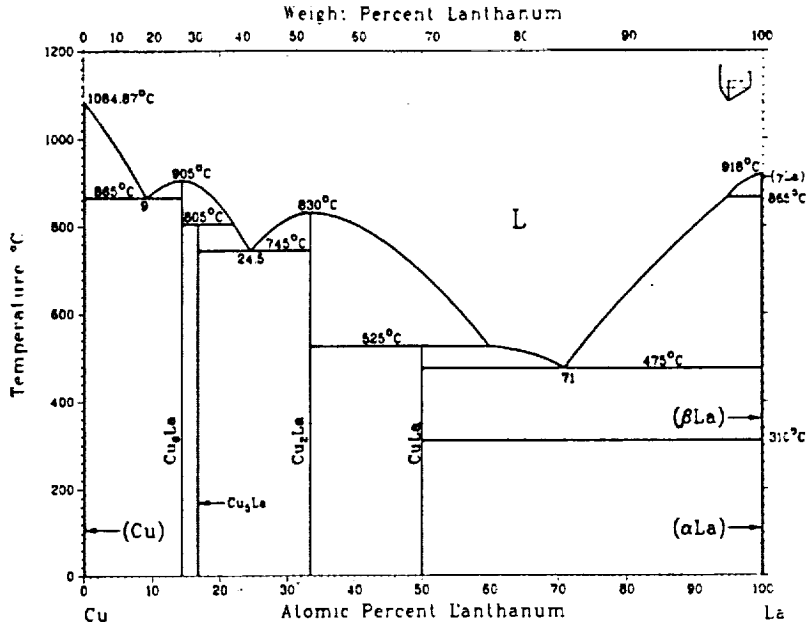

Figure AI-3. Cu-La phase diagram. [Chakrabarti and Laughlin, 1981]

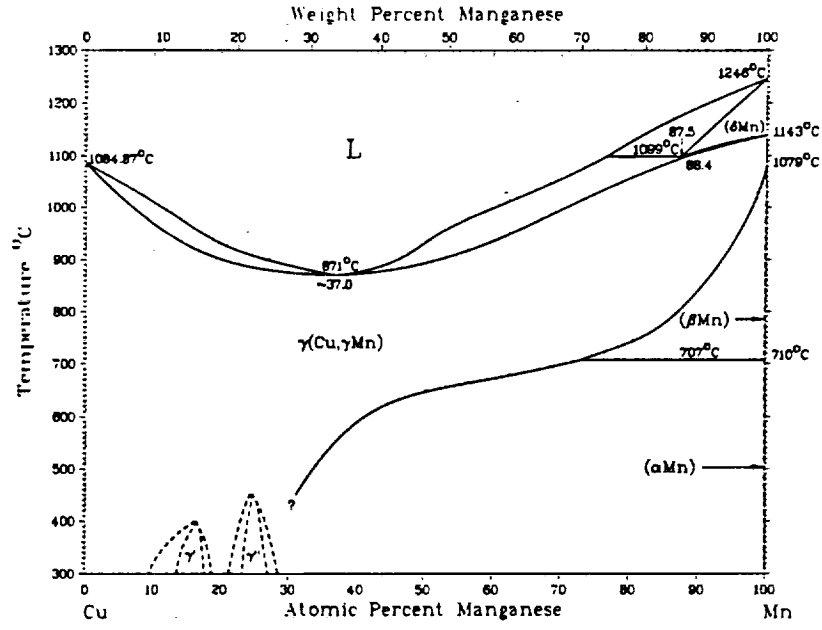

Figure AI-4. Cu-Mn phase diagram. [Binary Alloy Phase Diagrams, 1986, redrawn from Metals]

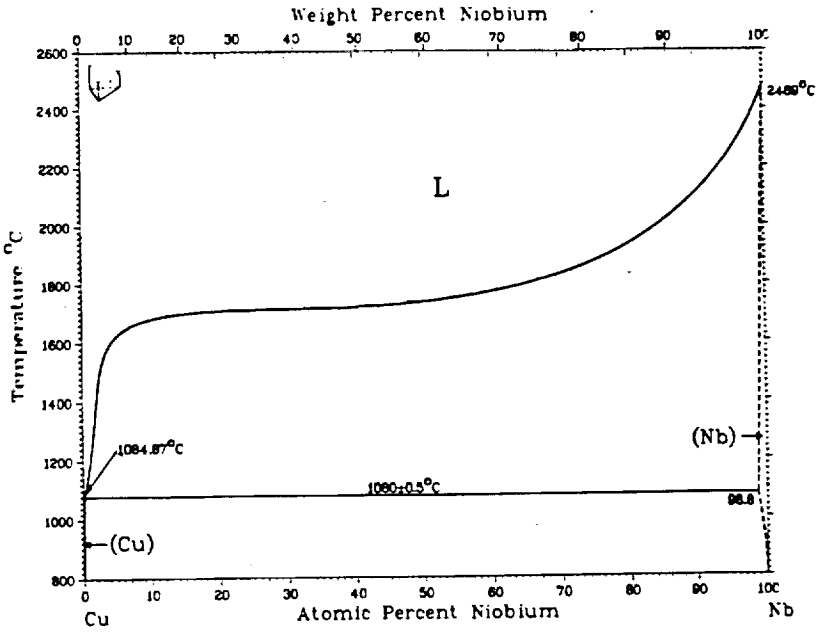

Figure AI-5. Cu-Nb phase diagram. [Chakrabarti and Laughlin, 1982]

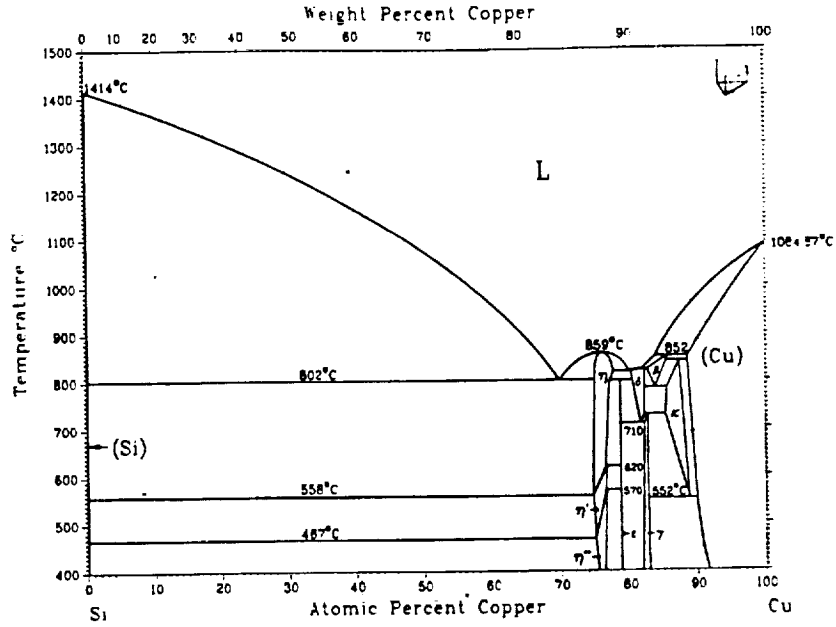

Figure AI-6. Si-Cu phase diagram. [Binary Alloy Phase Diagrams, 1986, from Olesinski and Abbaschian]

Figure AI-7. Ta-Cu phase diagram. [cannot find diagram]

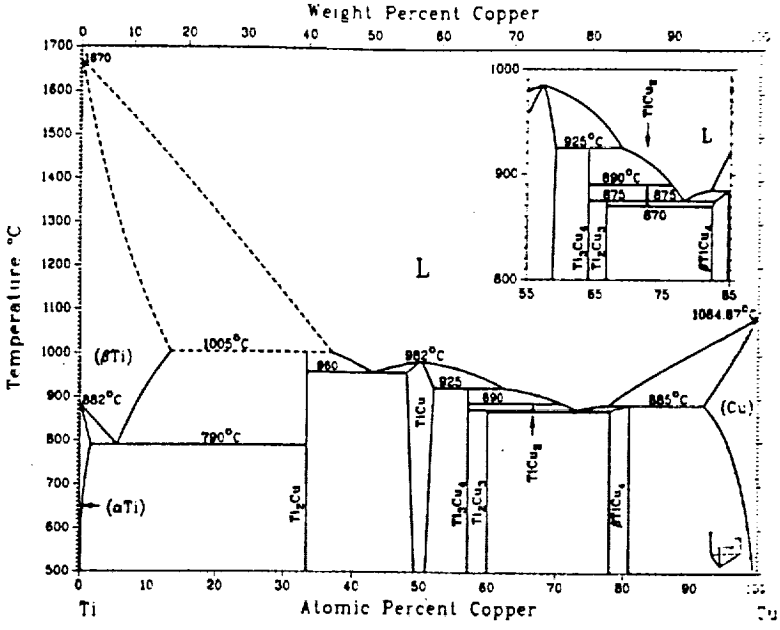

Figure AI-8. Ti-Cu phase diagram. [Binary Alloy Phase Diagrams, 1986, from Murray]

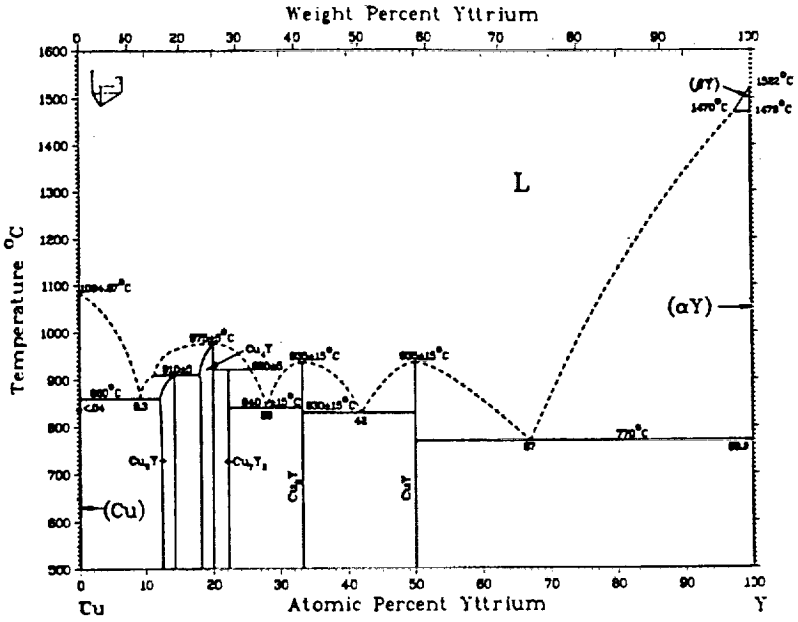

Figure AI-9. Cu-Y phase diagram. [Chakrabarti and Laughlin, 1981]

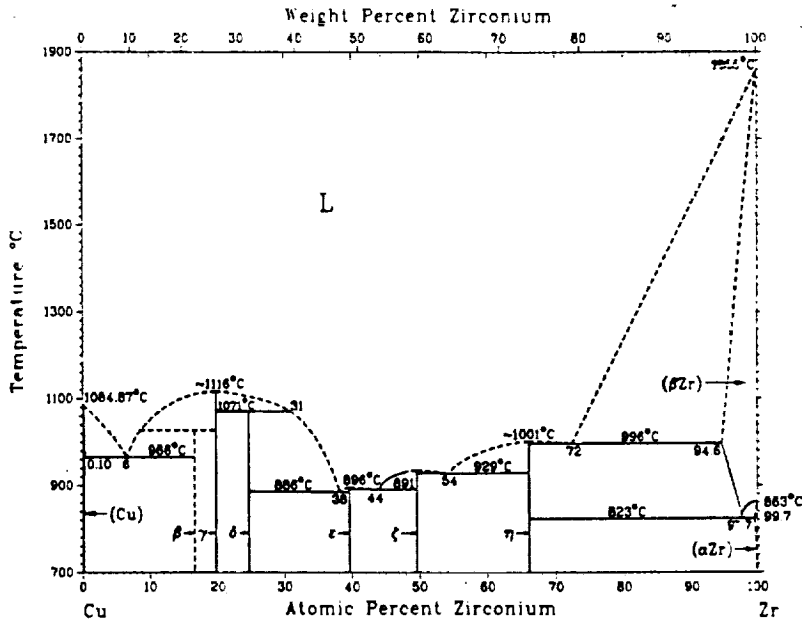

Figure AI-10. Cu-Zr phase diagram. [Binary Alloy Phase Diagrams, 1986, redrawn from Metals]

Appendix II

The diffraction data for C, Cr_3C_2, Cr_7C_3 and $Cr_{23}C_6$ are included in Figures AII-1 to AII-4. The cards shown contain data for d spacing (Å) of the peaks, peak intensity and planes of diffraction (hkl).

26-1080 C

C

Carbon

Rad. CuKα λ 1.54178 Filter d-sp Calculated
Cut off Int. Calculated $I/I_{cor.}$
Ref. Holcombe *Private Communication* (1974)

Sys. Hexagonal S.G. $P6_3mc$ (186)
a 2.480 b c 13.392 A C 5.4528
α β γ Z 8
Ref. Holcombe *U. S. AEC Oak Ridge Y-12 Plant Report Y1667* (1972)
D_x 2.281 D_m mp

Graphite structure. F_{30} = 51.6(.008,46). PSC: hPA

d Å	Int	hkl	d Å	Int	hkl
3.348	100	004			
2.1270	1	100			
2.1010	5	101			
2.0270	12	102			
1.9200	3	103			
1.7950	1	104			
1.6740	6	008			
1.6660	2	105			
1.5400	3	106			
1.4220	1	107			
1.2280	4	110			
1.1530	6	114			
1.1330	1	1010			
1.1160	1	0012			
1.0500	1	202			
0.9902	4	118			
0.9883	1	1012			
0.8370	1	0016			
0.8259	4	1112			
0.7962	1	212			

Figure AII-1. X-ray diffraction card for C.

35-804 ★

Cr_3C_2

Chromium Carbide

Rad. CuKα$_1$ λ 1.540598 Filter Mono d-sp Diff
Cut off 17.7 Int. Diffractometer I/I$_{cor.}$
Ref. *Nat. Bur. Stand. (U.S.) Monogr.* 21 (1984)

Sys. Orthorhombic S.G. Pnam (62)
a 5.5273(2) b 11.4883(5) c 2.8286(2) A 0.4811 C 0.2462
α β γ Z 4
Ref. Ibid.

D$_x$ 6.657 D$_m$ mp

Color Dark gray
The mean temperature of data collection was 24.0 C. The sample was obtained from Aesar Division of Johnson Matthey, Inc., Seabrook, New Hampshire, USA. CAS#: 12012-05-0. σ(I$_{obs}$) = ± 3. Cr_3C_2 type structure. Also called: Trichromium dicarbide. F$_{30}$=122.0(0.006,43). Silicon used as internal standard. PSC: oP20. To replace 14-406.

See following card

d Å	Int	hkl	d Å	Int	hkl
4.978	<1	110	1.5302	9	311
3.983	<1	120	1.4987	7	251
3.146	2	130	1.4375	3	350
2.7460	18	011	1.4193	3	071
2.5478	23	140	1.4143	19	002
2.4897	13	220	1.3902	1	180
2.4596	9	111	1.3720	5	410
2.3063	100	121	1.3273	4	360
2.2751	10	031	1.2997	1	430
2.2409	60	230	1.2812	2	351
2.1215	21	150	1.2626	5	271
2.1036	10	131	1.2474	13	181
1.9912	25	240	1.2367	5	142
1.9482	45	211	1.2342	6	411
1.9151	29	060	1.2296	3	222
1.8934	34	141	1.2254	8	370
1.8691	49	221	1.2135	6	421
1.8190	27	310	1.2017	11	361
1.7833	26	051	1.1961	12	232
1.7670	1	250	1.1810	10	431
1.7567	8	231	1.1768	6	152
1.6975	25	151	1.1619	6	281
1.6602	3	330	1.1590	6	290
1.6286	6	241	1.1531	8	242
1.5734	5	170	1.1397	4	441

35-804a ★

Cr_3C_2

Chromium Carbide

Rad. λ Filter d-sp
Cut off Int. I/I$_{cor.}$
Ref.

Sys. S.G.
a b c A C
α β γ Z
Ref.

D$_x$ D$_m$ mp

See preceding card

d Å	Int	hkl	d Å	Int	hkl
1.1378	11	062			
1.1247	8	1100			
1.1167	9	312			
1.1015	4	510			
1.0923	4	451			
1.0856	1	520			
1.0767	2	332			
1.0722	1	291			
1.0659	3	2100			
1.0571	3	470			
1.0519	3	262			
1.0493	3	390			
1.0317	3	540			
1.0262	2	1110			
1.0134	2	521			

Figure AII-2. X-ray diffraction cards for Cr_3C_2.

36-1482 ★

Cr_7C_3

Chromium Carbide

Rad. $CuK\alpha_1$ λ 1.540598 Filter Mono. d-sp Diff.
Cut off 17.7 Int. Diffractometer $I/I_{cor.}$
Ref. *Nat. Bur. Stand. (U.S.) Monogr.*, 22 (1985)

Sys. Orthorhombic S.G. Pmcn (51)
a 7.0149(12) b 12.153(2) c 4.5320(4) A 0.5772 C 0.3729
α β γ Z 4
Ref. Ibid.

D_x 6.877 D_m mp

Color Olive gray
Peak height intensities. The mean temperature of data collection was 24.6 C. The sample was obtained from CERAC, Incorporated, Milwaukee, Wisconsin, USA. CAS#: 12075-40-0. See card 11-550. The structure was determined by Rouault, M., Herpin, P., Fruchart, M., Ann. Chim. (Paris), 5, 461 (1970). $\sigma(I_{obs}) = \pm 1$. Also called: heptachromium tricarbide. $F_{30} = 22.9(.0078,167)$. Tungsten used as internal standard. PSC: oP40.

d Å	Int	hkl	d Å	Int	hkl
3.039	2	040	1.2107	12	333
2.2969	33	150	1.1929	1	502
2.2659	3	002	1.1874	13	282
2.1412	6	051	1.1737	10	551
2.1231	46	112	1.1706	12	522
2.0489	100	151	1.1694	12	390
2.0256	13	060	1.1445	<1	192
1.9662	1	321	1.1391	<1	413
1.9028	5	202	1.1330	1	004
1.8490	11	331	1.1323	1	391
1.8162	24	222	1.1248	2	353
1.7883	3	161			
1.7546	16	260			
1.7150	1	341			
1.6122	2	312			
1.5196	2	080			
1.5099	2	332			
1.4404	5	081			
1.4157	1	033			
1.3873	1	133			
1.3526	7	223			
1.3326	2	281			
1.3281	1	143			
1.2622	3	153			
1.2151	3	550			

 1610

Figure AII-3. X-ray diffraction card for Cr_7C_3.

35-783 ★

$Cr_{23}C_6$

Chromium Carbide

Rad. $CuK\alpha_1$ λ 1.540598 Filter Mono d-sp Diff
Cut off Int. Diffractometer $I/I_{cor.}$
Ref. *Nat. Bur. Stand. (U.S.) Monogr.*, 25 21 (1984)

Sys. Cubic S.G. Fm3m (225)
a 10.6599(5) b c A C
α β γ Z 4
Ref. Ibid

D_x 6.953 D_m mp

Color Gray
The mean temperature of data collection was 24.0 C. The sample was obtained from CERAC, Incorporated, Milwaukee, Wisconsin, USA. CAS# 12105-81-6. Spectrographic analysis (wt %, CERAC, Incorporated): 0.1 Al, Fe, Si, 0.08 Mo, 0.07 Mg, 0.01 V, 0.008 Ti, 0.003 Ni, 0.002 Ca, Cu. $\sigma(I_{obs}) = \pm 1$. $F_{23} = 69.6(0.011,38)$. Silicon used as internal standard. PSC: cF116. To replace 14-407.

d Å	Int	hkl	d Å	Int	hkl
6.148	1	111	1.0712	3	771
3.214	1	311	1.0453	<1	1020
3.077	1	222	1.0259	1	1022
2.666	4	400			
2.445	1	331			
2.383	23	420			
2.176	24	422			
2.0520	100	511			
1.8840	20	440			
1.8016	12	531			
1.7767	12	600			
1.6857	2	620			
1.6261	2	533			
1.6067	6	622			
1.4930	<1	551			
1.4788	<1	640			
1.3327	2	800			
1.2928	2	820			
1.2560	12	822			
1.2308	6	751			
1.2227	15	662			
1.1920	2	840			
1.1698	4	911			
1.1174	1	931			
1.0879	6	844			

 878

Figure AII-4. X-ray diffraction card for $Cr_{23}C_6$.

NASA
National Aeronautics and Space Administration

Report Documentation Page

1. Report No.	2. Government Accession No.	3. Recipient's Catalog No.
NASA CR-187143		

4. Title and Subtitle	5. Report Date
Development of Graphite/Copper Composites Utilizing Engineered Interfaces	June 1991
	6. Performing Organization Code

7. Author(s)	8. Performing Organization Report No.
Sandra M. DeVincent	None
	10. Work Unit No. 505-63-40

9. Performing Organization Name and Address	11. Contract or Grant No.
Case Western Reserve University 10900 Euclid Avenue Cleveland, Ohio 44106	NCC3-94
	13. Type of Report and Period Covered Contractor Report Final

12. Sponsoring Agency Name and Address	14. Sponsoring Agency Code
National Aeronautics and Space Administration Lewis Research Center Cleveland, Ohio 44135-3191	

15. Supplementary Notes

Project Manager, Donald Petrasek, Materials Division, NASA Lewis Research Center, (216) 433-5528. Report was submitted as a dissertation in partial fulfillment of the requirements for the degree of Master of Science, Case Western Reserve University, Cleveland, Ohio 44106.

16. Abstract

In situ measurements of graphite/copper alloy contact angles have been made using the sessile drop method. The interfacial energy values obtained from these measurements have then been applied to a model for the fiber/matrix interfacial debonding phenomenon found in graphite/copper composites. The information obtained from the sessile drop tests has led to the development of a copper alloy that suitably wets graphite. Characterization of graphite/copper alloy interfaces subjected to elevated temperatures has been conducted using Scanning Electron Microscopy, Energy Dispersive Spectroscopy, Auger Electron Spectroscopy and X-Ray Diffraction analyses. These analyses have indicated that during sessile drop tests conducted at 1130 °C for 1 hour, copper alloys containing greater than 0.98 at% chromium form continuous reaction layers of approximately 10 μm in thickness. The reaction layers are adherent to the graphite surface. The copper wets the reaction layer to form a contact angle of 60° or less. X-ray diffraction results indicate that the reaction layer is Cr_3C_2.

17. Key Words (Suggested by Author(s))	18. Distribution Statement
Graphite Copper Interface Reaction layer	Unclassified - Unlimited Subject Category 24

19. Security Classif. (of the report)	20. Security Classif. (of this page)	21. No. of pages	22. Price*
Unclassified	Unclassified	106	A06

*For sale by the National Technical Information Service, Springfield, Virginia 22161